Quantification of phase transformations using calorimetry and dilatometry

by

Ata Ollah Kamyabi Gol

A thesis submitted in partial fulfillment of the requirements for the degree of

Doctor of Philosophy

in

Materials Engineering

Department of Chemical and Materials Engineering

University of Alberta

Abstract

Dilatometry and calorimetry are well-established techniques, and have been used successfully for decades; however, they are seldom used to quantify the progress of a transformation. Most often, these techniques are used to detect start and finish of transformations. When used quantitatively, current analysis of dilation data does not account for the different changes in density for the multiple transformed phases. Similarly, quantitative calorimetric analysis does not account for different rates of enthalpy release for different transformed phases.

The technique proposed for both dilatometry and calorimetry consists on posing a differential equation based on dilation or temperature data generated under controlled experimental conditions. When integrated, this equation extracts phase fraction evolution from the experimental data. Like all differential equations, the equation posed involves coefficients and integration constants. The work presented differs from other similar work in that the coefficients are obtained from calibration before, after, and at transition points for each transformation, with a minimum of need of previously tabulated data.

These methods can go beyond any previous approach by quantifying partial transformations and making in-situ measurements of phase fractions in complex simultaneous phase transformations possible. This is possible because of a rigorous framework that reduces the number of unknown parameters to its minimum. The mathematical treatments will be introduced, and applications will be discussed involving precipitation during solidification in aluminum A356 alloy, martensitic transformation in creep-resistant steel, and simultaneous bainitic and martensitic transformations in AISI 4140 steel.

Preface

The Materials presented in the current thesis are parts of the research project under supervision of Dr. Patricio Mendez, which has been funded by Natural Sciences and Engineering Research Council (NSERC) of Canada, Codes And Standards Training Institute (CASTI), and MITACS.

Chapter 2 of this work is published as Kamyabi-Gol, A., Mendez, P., 2014 "The Evolution of the Fraction of Individual Phases During a Simultaneous Multiphase Transformation from TimeTemperature Data", *Metallurgical and Materials Transactions A.*

Chapter 3 of this work is published as Gibbs, J., Schlacher, C., Kamyabi-Gol, A., Mayr, P., Mendez, P., 2014 "Cooling Curve Analysis as an Alternative to Dilatometry in Continuous Cooling Transformations", *Chemical Engineering Metallurgical and Materials Transactions A*. The experiments were supervised by Dr. Peter Mayr and performed at University of Chemnitz, Germany.

Chapter 4 of this work has been submitted as Kamyabi-Gol, A., Clark, S., Gibbs, J., Seetharaman, S., Mendez, P., 2015 "Quantification of multiple simultaneous phase transformations using dilation curve analysis (DCA)", to the journal of *Acta Materialia.* Hot-stage microscopy was performed by Samuel Clark, supervised by Dr. Sridhar Seetharaman at University of Warwick.

Chapter 5 of this work has been submitted as Herath, D., Kamyabi-Gol, A., Mendez, P., 2015 "Effect of austenite grain size on transformation kinetics and the CCT diagram of 4140 steel", to the journal of *Metallurgical and Materials Transactions A*.

It should be mentioned that the format of this thesis is paper-based and there might be some repetition, specially in the "Experimental" section of each chapter.

To my sister and my parents, for their love, encouragement and continuous support.

Acknowledgements

Words can not describe my gratitude towards my supervisor, Dr. Patricio Mendez, for his appreciable inspiration, support and patience throughout my PhD studies. His invaluable kindness, guidance and comments allowed me to develop my personality and knowledge. It was a great pleasure to have the opportunity to work under his supervision.

I would like to express my special appreciation and thanks to Dr. Leijun Li for his great inspiration, kindness and guidance.

I would like to acknowledge and thank Dr. Peter Mayr, Dr. John Gibbs and Dr. Sridhar Seetharaman for their guidance and helpful suggestions. I would like to express my gratitude to a number of students, technicians and research assistants for their valuable support, suggestions, and assistance which aided the success of my experiments: Dr. Goetz Dapp, Dr. Abolfazl Noorjahan, Mr. Samual Clark, Mr. Christian Schlacher, Mr. Chris Rice, Mr. Shinya Myojin and Mr. Dhanusha Herath.

I would especially like to thank Gentry Wood, Nairn Barnes and all of my friends and colleagues at the Canadian Centre for Welding and Joining (CCWJ) for all of their support, help and encouragement throughout my program. A special gratitude to my friends Pouyan Motamedi, Mohammad Khalkhali, Lena Abbasi, Hossein Izadi, Behnam Berahman, Sahar Salimi, Andrea Jeffery, Solmaz Adam-Aref, Pooya Delshad-Khatibi, Nasseh Khodai, Maryam Aboui, Nicole (Nicki) Robertson, Scott Pavelich, Melodie Schaefer-Simard, Mareli Kemp, Meisam Nouri for being there for me when I needed good advice.

I would like to gratefully acknowledge the Natural Sciences and Engineering Research Council (NSERC) of Canada, Codes And Standards Training Institute (CASTI), and MITACS for financial support.

Last but not least, I would like to express my gratitude to my parents for their continued, endless and unconditional support, patience, love and understanding throughout my life. They have always and continue to support my choices and dreams and encourage me to pursue them.

Contents

List of Tables

List of Figures

Chapter 1

Introduction

1.1 Introduction

Cooling curve analysis (CCA) has been discussed in the literature for a long time and has reached a high degree of progress (Kamyabi-Gol and Mendez, 2014; Gibbs and Mendez, 2008; Gibbs, 2009; Gibbs et al., 2010; Xu et al., 2011; Fornaro and Palacio, 2009). CCA for a single phase transformation is well-established and discussed in (Gibbs and Mendez, 2008; Gibbs, 2009; Gibbs et al., 2010). The CCA methodology for multiple phase transformations is presented here. Similar to previous CCA techniques, this method relies on measuring the temperature of a sample as it undergoes phase transformations during Newtonian cooling. The proposed CCA method can work under a variety of cooling conditions (Kamyabi-Gol and Mendez, 2014; Gibbs, 2009), requires little to no specialized machinery, facilities, computing power and is timesaving. These benefits are more evident when considering that these types of measurements are currently made using techniques that are either slow, expensive or difficult to access, and in some cases, unable to accommodate realistic sample sizes or cooling rates; among those one can mention microscopy (Barrena et al., 2013), differential scanning calorimetry (DSC) (Barrena et al., 2013; Kuntz et al., 2013; Xu et al., 2012; Birol, 2009), differential thermal analysis (DTA) (MacKenzie, 1970; Alexandrov and Lippold, 2007), synchrotron diffraction

(Béchade et al., 2013), dilatometry (Tszeng and Shi, 2004; Bojack et al., 2012; Frankel et al., 2005) or indirect measurements such as magnetic field (Bakhtiyarov et al., 2004) and electrical resistivity (Kiuchi and Sugiyama, 1994). The limitations of these techniques are discussed in (Gibbs et al., 2010).

Dilatometry is a well-established technique primarily used to study the response of a material to temperature change (Speyer, 1993). The data obtained from a dilatometer is used to calculate the start and finish temperatures of the transformation(s). American Society for Testing and Materials (ASTM) has developed a well-known method (informally called the *lever-rule* method) for quantifying the fraction of a forming phase from dilatation data (ASTM A1033-10, 2013). However, this method assumes the progression of the phase transformation is proportional to the dilatation progression between two baselines (Zhao et al., 2001). In addition, this standard method bundles all simultaneous transformations as if a *single phase transformation* took place and the parent phase transformed into a homogeneous phase. This is rarely the case in most materials specifically steels continuously cooled after austenitizing (Kop et al., 2001).

Much work has been done towards a better analysis of dilatometry data to better predict the phase fractions in materials which undergo multiple phase transformations. Onink et. al. pioneered models for quantifying the phase fractions in multiple phase transformations in Fe-C steels (Onink and Tichelaar, 1996). Their models are based on the lattice parameters of the constituting phases and their dependence on temperature and composition. Many researchers have built on the analysis presented in (Onink and Tichelaar, 1996) and tried to expand them to take into account alloying elements (Choi, 2003; Gómez et al., 2003; Lee and Tyne, 2011), and diffusionless phase transformations (e.g. formation of martensite and bainite from austenite) (Lee et al., 2007; Kop et al., 2001; Suh et al., 2007; Warke et al., 2009). De Andres et. al. have developed a model on the basis of lattice parameters for the decomposition of pearlite to austenite in an eutectoid steel upon heating (de Andrés et al., 1998). Other researchers have taken a different approach and used the density of the constituting phases as the basis of their models (Zhao et al., 2001, 2002). Dykhuizen et. al. have developed a self-calibrating method with expressions for the phase densities as a function of temperature and composition to predict the austenite fraction in austenitization of a low carbon steel (Dykhuizen et al., 1999). Avrami-type mathematical expressions are also used in some literature to quantify the transformation kinetics in low carbon steels (Leeuwen et al., 2001; Tszeng and Shi, 2004).

All of the work discussed in the previous paragraph is finely tuned for specific alloy systems (mainly low alloy and low carbon steels) and are rarely applicable to the broader group of materials. In addition, most of the models suffer from limiting assumptions (e.g. geometrical assumptions, equilibrium estimations for non-equilibrium transformations, limited number of alloying elements, etc.) that hinder their application to all phase transformations.

The goal of both dilation curve analysis (DCA) and CCA is to obtain phase fraction evolution information of a material as it undergoes heating or cooling. Because of the similarities in the results and sample conditions during the experiment, DCA and CCA can be seen as complementary techniques. The primary difference between DCA and CCA is that the dilatometry model is based on the length of the sample, which is measured directly, whereas calorimetry is based on the temperature of the sample, which must be processed by using a heat transfer model (Gibbs et al., 2014).

1.2 Objectives

The main objective of this research project is to illustrate that the information regarding the phase fractions obtained from a dilatometer can be replicated using calorimetry which has a much simpler and less-expensive setup. In order to achieve this goal, the following objectives have been established:

- Establish rigorous mathematical methodologies to separate individual phase fractions from multiple simultaneous phase transformations using temperature-time and/or dilation-temperature data.
- Apply the methodologies to appropriate materials to illustrate their applicability.
- Compare results from the DCA and CCA methodologies for a single phase transformation to show reproducibility.

1.3 Thesis Outline

This thesis consists of 6 chapters focusing on achieving the above objectives. After the Introduction, in chapter 2, a rigorous mathematical methodology for separating multiple simultaneous phase transformations from temperature-time data is established. This method is applied to ten variations of aluminum A356 alloy to separate the final fraction of the $\alpha-$aluminum matrix and precipitates.

chapter 3 focuses on the development of DCA for a single phase transformation. In this chapter, DCA is compared to CCA for the single phase transformation of austenite to martensite in creep resistant 9Cr3W3CoVNb steel. The results presented in this chapter will show that CCA can replicate the results from DCA with high precision.

DCA for multiple simultaneous phase transformations is developed step by step in chapter 4. This new DCA methodology is applied to the simultaneous phase transformation of austenite to bainite and martensite in seven cylindrical AISI 4140 steel samples cooled at rates between 1 and 4 K/s in a dilatometer. The results show that the new DCA methodology can successfully separate the bainite and martensite fractions.

chapter 5 is mainly focused on comparing all the methodologies currently used to evaluate dilation/temperature data obtained from a dilatometer. Six different methods are used to measure the martensite start and finish temperatures and plot the martensite fraction evolution curve (where possible) in twelve AISI 4140 steels with varying austenite grain sizes.

Finally, chapter 6 summarizes and concludes the thesis.

1.4 References

Alexandrov, B.T., Lippold, J.C., 2007. Single Sensor Differential Thermal Analysis of Phase Transformations and Structural Changes During Welding and Postweld Heat Treatment. Welding in the World 51, 48–59.

de Andrés, C.G., Caballero, F., Capdevila, C., Bhadeshia, H.K.D.H., 1998. Modelling of kinetics and dilatometric behavior of non-isothermal pearlite-to-austenite transformation in an eutectoid steel. Scripta Materialia 39, 791–796.

ASTM A1033-10, 2013. Standard Practice for Quantitative Measurement and Reporting of Hypoeutectoid Carbon and Low-Alloy Steel Phase Transformations 1, pp. 1–14.

Bakhtiyarov, S.I., Dupac, M., Overfelt, R.a., Teodorescu, S.G., 2004. On Electrical Conductivity Measurements of Molten Metals by Inductive Technique. Journal of Fluids Engineering 126, 468–470.

Barrena, M.I., Gómez de Salazar, J.M., Pascual, L., Soria, A., 2013. Determination of the kinetic parameters in magnesium alloy using TEM and DSC techniques. Journal of Thermal Analysis and Calorimetry 113, 713–720.

Béchade, J.L., Menut, D., Doriot, S., Schlutig, S., Sitaud, B., 2013. X-ray diffraction analysis of secondary phases in zirconium alloys before and after neutron irradiation at the MARS synchrotron radiation beamline. Journal of Nuclear Materials 437, 365–372.

Birol, Y., 2009. Solid fraction analysis with DSC in semi-solid metal processing. Journal of Alloys and Compounds 486, 173–177.

Bojack, A., Zhao, L., Morris, P., Sietsma, J., 2012. In-situ determination of austenite and martensite formation in 13Cr6Ni2Mo supermartensitic stainless steel. Materials Characterization 71, 77–86.

Choi, S., 2003. Model for estimation of transformation kinetics from the dilatation data during a cooling of hypoeutectoid steels. Materials Science and Engineering: A 363, 72–80.

Dykhuizen, R., Robino, C., Knorovsky, G., 1999. A Method for Extracting Phase Change Kinetics from Dilatation for Multistep Transformations : Austenitization of a Low Carbon Steel. Metallurgical and Materials Transactions B 30, 107–117.

Fornaro, O., Palacio, H.a., 2009. Study of dilute AlCu solidification by cooling curve analysis. Journal of Materials Science 44, 4342–4347.

Frankel, J.I., Porter, W.D., Sabau, A., 2005. Analysis of Volumetric Changes Through Melting Using a Dilatometer. Journal of Thermal Analysis and Calorimetry 82, 171–177.

Gibbs, J.W., 2009. Thermal Analysis Techniques for Phase Fraction Measurements of First-order Phase Transformations. Msc. Colorodo School of Mines.

Gibbs, J.W., Kaufman, M.J., Hackenberg, R.E., Mendez, P.F., 2010. Cooling Curve Analysis to Determine Phase Fractions in Solid-State Precipitation Reactions. Metallurgical and Materials Transactions A 41, 2216–2223.

Gibbs, J.W., Mendez, P.F., 2008. Solid fraction measurement using equation-based cooling curve analysis. Scripta Materialia 58, 699–702.

Gibbs, J.W., Schlacher, C., Kamyabi-Gol, A., Mayr, P., Mendez, P.F., 2014. Cooling Curve Analysis as an Alternative to Dilatometry in Continuous Cooling Transformations. Metallurgical and Materials Transactions A 46, 148–155.

Gómez, M., Medina, S.F., Caruana, G., 2003. Modelling of Phase Transformation Kinetics by Correction of Dilatometry Results for a Ferritic Nb-microalloyed Steel. ISIJ International 43, 1228–1237.

Kamyabi-Gol, A., Mendez, P.F., 2014. The Evolution of the Fraction of Individual Phases During a Simultaneous Multiphase Transformation from TimeTemperature Data. Metallurgical and Materials Transactions A 46, 622–638.

Kiuchi, M., Sugiyama, S., 1994. A New Method to Detect Solid Fractions of Mushy/Semi-Solid Metals and Alloys. Annals of the CIRP 43, 271–274.

Kop, T., Sietsma, J., Zwaag, S.V.D., 2001. Dilatometric analysis of phase transformations in hypo-eutectoid steels. Journal of materials science 36, 519–526.

Kuntz, M.L., Panton, B., Wasiur-Rahman, S., Zhou, Y., Corbin, S.F., 2013. An Experimental Study of Transient Liquid Phase Bonding of the Ternary Ag-Au-Cu System Using Differential Scanning Calorimetry. Metallurgical and Materials Transactions A 44, 3708–3720.

Lee, S.J., Lusk, M., Lee, Y.K., 2007. Conversional model of transformation strain to phase fraction in low alloy steels. Acta Materialia 55, 875–882.

Lee, S.J., Tyne, C.J.V., 2011. Prediction of Martensite Volume Fraction in FeCrNi Alloys. ISIJ International 51, 169–171.

Leeuwen, Y.V., Onink, M., Sietsma, J., Zwaag, S.V.D., 2001. The .GAMMA.-.ALPHA.Transformation Kinetics of Low Carbon Steels under Ultra-fast Cooling Conditions. ISIJ International 41, 1037–1046.

MacKenzie, R.C., 1970. Differential Thermal Analysis. Academic Press.

Onink, M., Tichelaar, F., 1996. Quantitative analysis of the dilatation by decomposition of Fe-C austenites; Calculation of volume change upon transformation. Zeitschrift fur … 87, 24–32.

Speyer, R., 1993. Thermal analysis of materials.

Suh, D.W., Oh, C.S., Han, H.N., Kim, S.J., 2007. Dilatometric analysis of austenite decomposition considering the effect of non-isotropic volume change. Acta Materialia 55, 2659–2669.

Tszeng, T., Shi, G., 2004. A global optimization technique to identify overall transformation kinetics using dilatometry dataapplications to austenitization of steels. Materials Science and Engineering: A 380, 123–136.

Warke, V.S., Sisson, R.D., Makhlouf, M.M., 2009. A Model for Converting Dilatometric Strain Measurements to the Fraction of Phase Formed during the Transformation of Austenite to Martensite in Powder Metallurgy Steels. Metallurgical and Materials Transactions A 40, 569–572.

Xu, J., Liu, F., Xu, X., Chen, Y., 2011. Determination of Solid Fraction from Cooling Curve. Metallurgical and Materials Transactions A 43, 1268–1276.

Xu, J.F., Liu, F., Zhang, D., Zhang, K., 2012. Comparison of baseline method and DSC measurement for determining phase fractions. Materials Science and Technology 28, 1420–1425.

Zhao, J., Mesplont, C., Cooman, C., 2002. Calculation of the phase transformation kinetics from a dilatation curve. Journal of Materials Processing Technology 129, 345–348.

Zhao, J.Z., Mesplont, C., Cooman, B.C.D., 2001. Kinetics of Phase Transformations in Steels: A New Method for Analysing Dilatometric Results. ISIJ International 41, 492–497.

Chapter 2

The Evolution of the Fraction of Individual Phases During a Simultaneous Multiphase Transformation from Time–Temperature Data

2.1 Introduction

Cooling curve analysis has been preached for long and has reached a high degree of progress (Gibbs and Mendez, 2008; Gibbs, 2009; Gibbs et al., 2010; Xu et al., 2011; Fornaro and Palacio, 2009). None of the existing literature, however, has addressed the proper treatment of multiple simultaneous phase transformations. This paper generalizes the well-established formalism of (Gibbs, 2009) to address multiple phase transformations rigorously. Similar to previous CCA techniques, the proposed method in this paper relies on measuring the temperature of a sample as it undergoes phase transformations during Newtonian cooling. In this method the heat balance between the cooling sample and the surrounding environment is used in addition to tabulated latent and specific heat of present phases to determine the fraction of all existing phases in the sample. The main benefit of this method is that it can be used for multiple simultaneous phase transformations with the number limited by the quality of input data used, not by the mathematical formulation as in past implementations of CCA (Gibbs, 2009; Gibbs et al., 2010; Gibbs and Mendez, 2008; Xu et al., 2013). This approach can work under a variety of cooling conditions (Gibbs, 2009), it requires little to none specialized machinery, facilities, computing power and it is timesaving. These benefits are more evident when considering that these types of measurements are currently made using techniques that are either slow, expensive or difficult to access, and in some cases, unable to accommodate realistic sample sizes or cooling rates; among those one can mention microscopy (Barrena et al., 2013), differential scanning calorimetry (DSC) (Barrena et al., 2013; Kuntz et al., 2013; Xu et al., 2012; Birol, 2009), differential thermal analysis (DTA) (MacKenzie, 1970; Alexandrov and Lippold, 2007), synchrotron diffraction (Béchade et al., 2013), dilatometry (Tszeng and Shi, 2004; Bojack et al., 2012) or indirect measurements such as density (Frankel et al., 2005), magnetic field (Bakhtiyarov et al., 2004) and electrical resistivity (Kiuchi and Sugiyama, 1994). The limitations of these techniques are discussed in (Gibbs et al., 2010).

Current CCA techniques are limited to tracking formation temperatures and phase fractions for *separate* phase transformations (e.g. solidification OR precipitation). The method presented here does not suffer from such a limitation and can be used for complex phase transformations such as precipitation during solidification in aluminum alloys or potentially for the austenite to pearlite/martensite/ferrite transformation in steels. A more complex example of the application of the proposed methodology is in the welding of pipeline microalloyed steels (e.g. X70, X80 and X100). These steels tend to form more than 5 phases upon cooling from austenite (Gladman, 1997). These phases can be any combination of ferrite, bainite, pearlite, martensite, TiN, Nb(C,N), V(C,N) and complex precipitates.

The general mathematical approach presented in the next section is compared against the simultaneous solidification and precipitation of ten variants of aluminum alloy A356.

2.2 Thermodynamic balance during multiple transformations

An important aspect of the proposed methodology is to assign a single temperature to the whole sample (Newtonian cooling). To achieve this goal, any experiment conducted must have a small Biot number ($Bi = \bar{h}_{\text{eff}} L_c / k << 1$ where $\bar{h}_{\text{eff}}$ is the average effective heat transfer coefficient (accounting for convection, radiation and insulation), L_c a characteristic length defined as $L_c = V/A_s$ where V and A_s are respectively the volume and surface area of the sample, and k the thermal conductivity of the sample)(Bergman et al., 2011). In this methodology, special care is taken to ensure that the heat transfer coefficient ($\bar{h}_{\text{eff}}$) is constant during cooling.

Without loss of generality, consider a sequence of phase transformations $1 \longrightarrow 2$, $1 \longrightarrow 3$, $\ldots$, $1 \longrightarrow n$ taking place at different time scales during cooling with Phase 1 being the only parent phase. An example of this transformation sequence is the precipitation of intermetallics in the interdendritic region of aluminum alloys during solidification. The precipitation in the solid during solidification requires a different sequence of transformations ($1 \longrightarrow 2$, $1 \longrightarrow 2$ & $2 \longrightarrow 3$) that can be analyzed with slight modifications to the derivations presented here.

The heat of transformation (ΔH_{ij}) is approximately constant in the temperature range between start and end of transformation. For example, in the precipitation of Mg_2Si in aluminum alloys, the latent heat of precipitation of Mg_2Si from the liquid phase is $\Delta H = -476.5$ J/g at 829.7 K (556.5 °C) (beginning of precipitation for Alloy 6 discussed later in Table 2.2. Alloy 6 displays the largest amount of precipitation of all alloys considered) and $\Delta H = -467.9$ J/g at 772.4 K (499.2 °C) (end of precipitation for Alloy 6) (Andersson et al., 2002). In this example, there is only a 1.8% change in the latent heat of precipitation from the beginning to the end of precipitation. In the analysis that follows, the heat of transformation will be considered constant.

For an experimental setup based on convective cooling, an energy balance indicates that all enthalpy released during cooling and phase transformations is balanced by the heat losses by convection at the surface of the sample. For a small amount of cooling, $-dT$, the enthalpic balance of the system is represented by:

$$\begin{aligned} & -mf_1c_{p_1}dT - mf_2c_{p_2}dT - mf_3c_{p_3}dT - \cdots - mf_nc_{p_n}dT + m\Delta H_{12}df_2 + \\ & + m\Delta H_{13}df_3 + \cdots + m\Delta H_{1n}df_n = \bar{h}_{eff}A_s(T - T_\infty)dt \end{aligned} \tag{2.1}$$

This equation accounts for multiple phases present at any given temperature, with those that are not present having a mass fraction (f_i) of zero. To adapt this formulation to a three-phase system, the value of n should be replaced by 3 and no new terms should be added. The symbols used are described in Table 2.1. The terms containing dT in Equation 2.1 represent the amount of heat released by the corresponding phase during cooling. The terms containing df_i represent the latent heat released do to the corresponding phase transformation. The term on the right hand side of Equation 2.1 describes the heat transferred to the surrounding environment.

Equation 2.1 can be rearranged as Equation 2.2 where $K' = \bar{h}_{\text{eff}}A_s/m$ and $f_i = f_i^c f_i^*$ (f_i is split up into a temperature dependant variable (f_i^*) that ranges from 0, before the transformation, to 1, after the transformation is complete and a constant (f_i^c), corresponding to the characteristic mass fraction of Phase i). The summation of the mass

Table 2.1: List of terms and symbols used.

Symbol	**Name**	**Units**
A	Mold area	m^2
$c_{p\,i}$	Specific heat capacity of Phase i	J/gK
f_i	Actual mass fraction of Phase i	g/g
f_i^c	Characteristic mass fraction of Phase i	g/g
f_i^*	Normalized mass fraction of Phase i	g/g
$F_{S\,E}$	Fraction of solid at eutectic start temperature	g/g
$F_{S\,P}$	Fraction of solid at precipitation start temperature	g/g
K'	Quantity defined in Equation 2.2	W/gK
m	Total mass of the sample	g
n	Index number	-
t	Time	s
$t_{S\,i}$	i^{th} phase formation start time	s
$t_{F\,i}$	i^{th} phase formation finish time	s
T	Measured temperature of the sample	K
T_E	Eutectic formation start temperature	K
T_L	Liquidus temperature	K
T_P	Precipitation start temperature	K
T_∞	Ambient temperature	K
α_i	Quantity related to sensible heat defined in Equation 2.2	s
β_i	Quantity related to latent heat defined in Equation 2.2	Ks
γ_i	Quantity related to heat of all phases except Phase i	s
ΔH_{ij}	Latent heat of transformation $i \longrightarrow j$	J/g

fraction of all phases equals one: i.e. $\sum_{i=1}^{n} f_i = 1$ and $\sum_{i=2}^{n} f_i^c = 1$.

$$\begin{aligned} &\overbrace{\frac{c_{p1}}{K'}}^{\alpha_1} dT + \overbrace{\frac{c_{p2} - c_{p1}}{K'} f_2^c}^{\alpha_2} f_2^* dT + \overbrace{\frac{c_{p3} - c_{p1}}{K'} f_3^c}^{\alpha_3} f_3^* dT + \cdots + \overbrace{\frac{c_{pn} - c_{p1}}{K'} f_n^c}^{\alpha_n} f_n^* dT - \\ &- \underbrace{\frac{\Delta H_{12}}{K'} f_2^c}_{\beta_2} df_2^* - \underbrace{\frac{\Delta H_{13}}{K'} f_3^c}_{\beta_3} df_3^* - \cdots - \underbrace{\frac{\Delta H_{1n}}{K'} f_n^c}_{\beta_n} df_n^* = -(T - T_\infty) dt \end{aligned} \tag{2.2}$$

Equation 2.2 can be further rearranged to group similar terms together and only leave out terms related to Phase 2 as shown below:

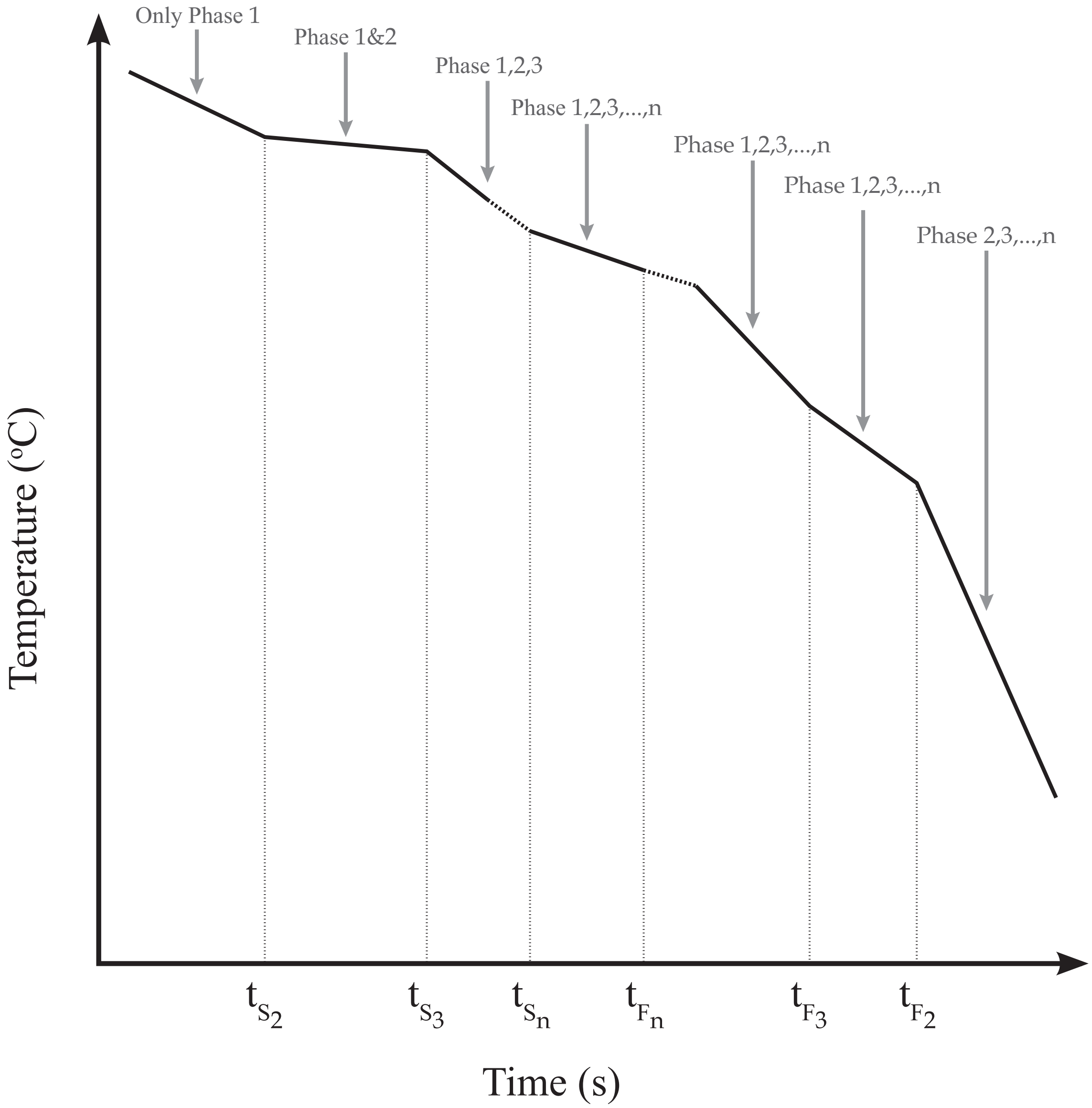

Figure 2.1: Schematic representation of a typical cooling curve with n phases and $n-1$ phase transformations.

$$\begin{cases} \overbrace{\left(\alpha_1 + \alpha_3 f_3^* + \cdots + \alpha_n f_n^* - \beta_3 \frac{df_3^*}{dT} - \cdots - \beta_n \frac{df_n^*}{dT}\right)}^{\gamma_2} dT + \alpha_2 f_2^* dT - \beta_2 df_2^* = -(T - T_\infty)dt \\ \gamma_2 dT + \alpha_2 f_2^* dT - \beta_2 df_2^* = -(T - T_\infty)dt \end{cases} \tag{2.3}$$

A similar procedure can be done to obtain equations similar to Equation 2.3 for all other phases. In relevance to the development of the current model, the equations for Phase 3 and Phase n are shown below:

$$\begin{cases} \overbrace{\left(\alpha_1 + \alpha_2 f_2^* + \cdots + \alpha_n f_n^* - \beta_2 \frac{df_2^*}{dT} - \cdots - \beta_n \frac{df_n^*}{dT}\right)}^{\gamma_3} dT + \alpha_3 f_3^* dT - \beta_3 df_3^* = -(T - T_\infty)dt \\ \gamma_3 dT + \alpha_3 f_3^* dT - \beta_3 df_3^* = -(T - T_\infty)dt \end{cases} \tag{2.4}$$

$$\begin{cases} \overbrace{\left(\alpha_1 + \alpha_2 f_2^* + \alpha_3 f_3^* + \cdots + \alpha_{n-1} f_{n-1}^* - \beta_2 \frac{df_2^*}{dT} - \beta_3 \frac{df_3^*}{dT} - \cdots - \beta_{n-1} \frac{df_{n-1}^*}{dT}\right)}^{\gamma_n} dT + \\ + \alpha_n f_n^* dT - \beta_n df_n^* = -(T - T_\infty)dt \\ \gamma_n dT + \alpha_n f_n^* dT - \beta_n df_n^* = -(T - T_\infty)dt \end{cases} \tag{2.5}$$

α_1 represents the material before any transformation has started (i.e. the portion of the cooling curve before t_{S_2} in Figure 2.1 where f_2^*, f_3^*,…, f_n^* and df_2^*, df_3^*, …, df_n^* are all zero). Therefore, we can evaluate α_1 by examining the portion of the cooling curve that only consists of Phase 1 (section of cooling curve before t_{S2} in Figure 2.1). When the only phase present in the material is Phase 1, all the other phase fractions will be zero (f_2^*=f_3^*=…=f_n^*=df_2^*=df_3^*=…=df_n^*=0 in Equation 2.2) hence we will have $\alpha_1 dT = -(T - T_\infty)dt$. This equation can be integrated to result in:

$$-\frac{1}{\alpha_1} = \frac{d[\ln(T - T_\infty)]}{dt} \tag{2.6}$$

Because heat transfer coefficient and specific heat of all phases are nearly constant in the experimental conditions of this methodology, the value of α_1 is nearly constant and its weak dependence on temperature will be captured as a gentle slope in a graph of $d[ln(T - T_\infty)]dt$ versus temperature.

The next step is to fit the inverse of α_1 to the experimental data (temperature vs. time) as a function of temperature (or time). This approach to evaluating α_1 does not require explicit evaluation of the individual parameters that make up α_1 (i.e. c_{p_1}, m, A, K).

By using a similar approach as used in evaluating α_1, one can evaluate each α_i and γ_i from a specific portion of the cooling curve. Equation 2.7 demonstrates how each portion of the schematic cooling curve in Figure 2.1 is used to evaluate α_i and γ_i.

$$\begin{cases} \alpha_1 \xrightarrow{\text{eval. from}} \text{portion of cooling curve before } t_{S2} \\ \alpha_2 + \gamma_2 \xrightarrow{\text{eval. from}} \text{portion of cooling curve after } t_{F2} \\ \gamma_2 \xrightarrow{\text{eval. from}} \text{portion of cooling curve before } t_{S2} \\ \alpha_3 + \gamma_3 \xrightarrow{\text{eval. from}} \text{portion of cooling curve after } t_{F3} \\ \gamma_3 \xrightarrow{\text{eval. from}} \text{portion of cooling curve before } t_{S3} \\ \qquad \vdots \qquad \textit{repeat for every phase} \\ \alpha_n + \gamma_n \xrightarrow{\text{eval. from}} \text{portion of cooling curve after } t_{Fn} \\ \gamma_n \xrightarrow{\text{eval. from}} \text{portion of cooling curve before } t_{Sn} \\ \alpha_1 + \alpha_2 + \alpha_3 + \cdots + \alpha_n \xrightarrow{\text{eval. from}} \text{portion of cooling curve after } t_{F2} \end{cases} \tag{2.7}$$

An example of how the values in Equation 2.7 are fitted to sample experimental data in the solidification of aluminum A356 alloy is shown in Figure 2.2. For example, it can be seen how a straight line is an appropriate approximation to the dependence of $-1/\alpha_1$ with temperature. Points A and B in Figure 2.2 where chosen in a way that the line passing through these two points is the best approximation for the entire region where only Phase 1 exists. Similarely, the line passing through points C and D in Figure 2.2 is the best fit line to approximate the dependence of $-1/\gamma_3$ with temperature. A single line passing through points E and F in Figure 2.2 can be used to simultaneously show the dependance of $-1/(\alpha_3 + \gamma_3)$, $-1/(\alpha_2 + \gamma_2)$, and $-1/(\alpha_1 + \alpha_2 + \alpha_3)$ on the temperature. Because the latent heat and the heat transfer properties in this methodology are nearly constant, the values of β_i in Equation 2.2 will be considered to be constant and can be calculated by forcing the corresponding f_i^* to be equal to 1 for the portion of the cooling curve where the corresponding Phase i has finished forming (i.e. after t_{Fi}). Hence we

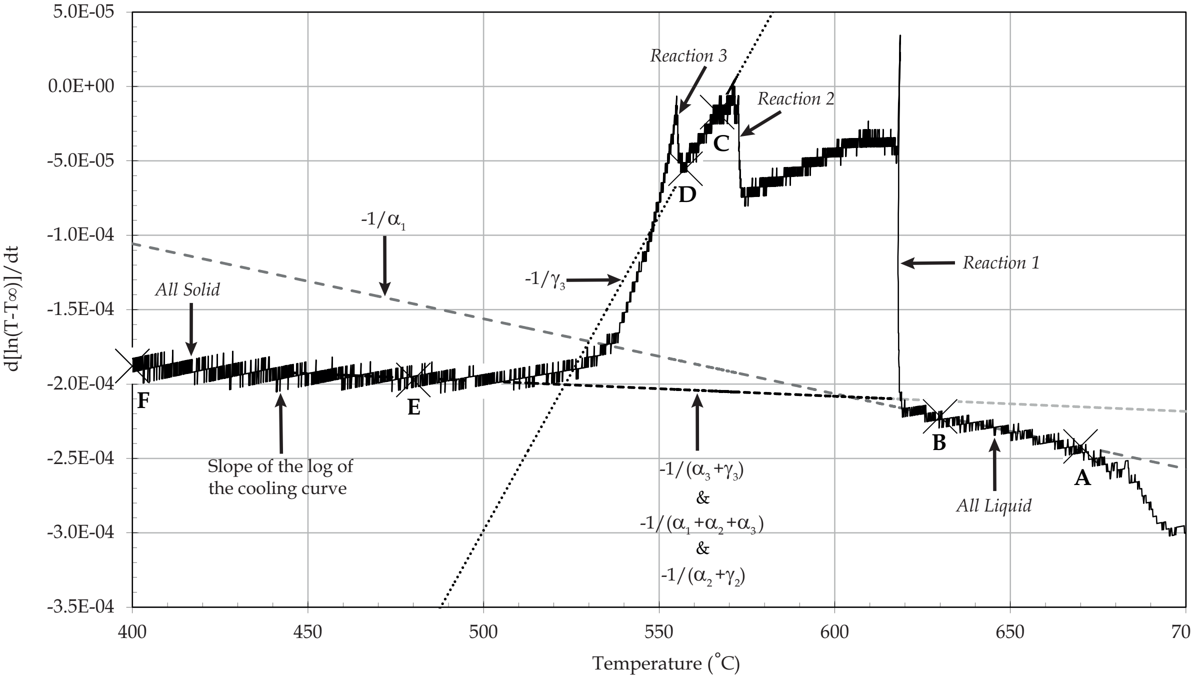

Figure 2.2: Fitting parameters in Equation 2.7 to experimental data (aluminum A356) as linear functions of temperature. The numbered reactions correspond to those described in Equation 2.11

have:

$$\begin{cases} \beta_2 \xrightarrow{\text{eval. by}} \text{forcing } f_2^* = 1 \text{ after } t_{F2} \\ \beta_3 \xrightarrow{\text{eval. by}} \text{forcing } f_3^* = 1 \text{ after } t_{F3} \\ \qquad \vdots \qquad \textit{repeat for every phase} \\ \beta_n \xrightarrow{\text{eval. by}} \text{forcing } f_n^* = 1 \text{ after } t_{Fn} \end{cases} \tag{2.8}$$

After evaluating α_1, α_2, α_3, …, α_n and β_2, β_3, …, β_n, an Euler explicit integration scheme is applied to Equation 2.3, Equation 2.4 and Equation 2.5 (and similar equations for all other phases) to obtain the fraction of each phase as shown below:

$$\begin{cases} f_2^{*i+1} = f_2^{*i} + \dfrac{1}{\beta_2}\Big[\gamma_2(T^{i+1} - T^i) + \alpha_2 f_2^{*i}(T^{i+1} - T^i) + (T^{i+1} - T_\infty)(t^{i+1} - t^i)\Big] \\ f_3^{*i+1} = f_3^{*i} + \dfrac{1}{\beta_3}\Big[\gamma_3(T^{i+1} - T^i) + \alpha_3 f_3^{*i}(T^{i+1} - T^i) + (T^{i+1} - T_\infty)(t^{i+1} - t^i)\Big] \\ \qquad \vdots \qquad \textit{repeat for every phase} \\ f_n^{*i+1} = f_n^{*i} + \dfrac{1}{\beta_n}\Big[\gamma_n(T^{i+1} - T^i) + \alpha_n f_n^{*i}(T^{i+1} - T^i) + (T^{i+1} - T_\infty)(t^{i+1} - t^i)\Big] \end{cases} \tag{2.9}$$

Finally, f_2^c, f_3^c, …, f_n^c can each be separately calculated as follows:

$$\begin{cases} f_3^c = \dfrac{c_{p1}\beta_3}{\alpha_1 \Delta H_{13}} \\ \qquad \vdots \qquad \textit{repeat for every phase} \\ f_n^c = \dfrac{c_{p1}\beta_n}{\alpha_1 \Delta H_{1n}} \\ f_2^c = 1 - \displaystyle\sum_{i=3}^{n} f_i^c \end{cases} \tag{2.10}$$

The specific heat capacity of Phase 1, enthalpy of formation of Phase 3 to n from Phase 1 (i.e. c_{p_1}, ΔH_{13}, …, ΔH_{1n} in Equation 2.2) need to be looked up from standard thermochemical tables or calculated through Thermo-Calc software.

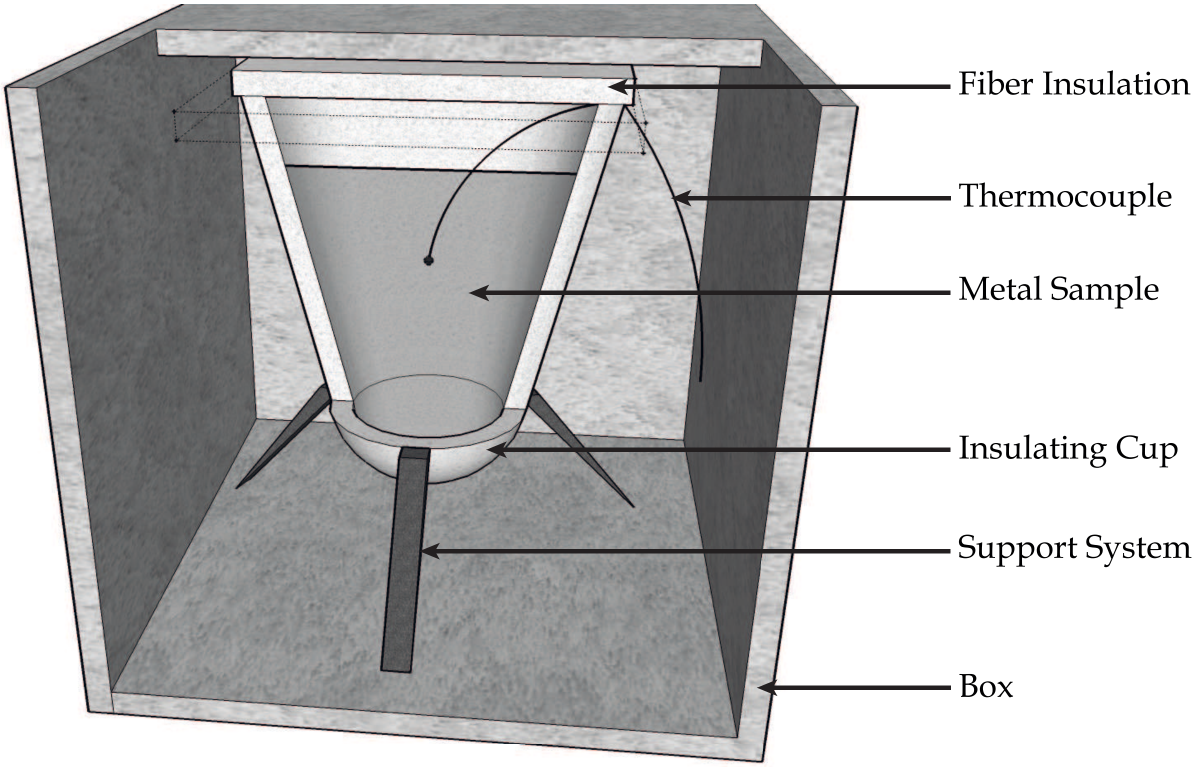

Figure 2.3: Schematic representation of experimental setup.

2.3 Experimental

To achieve Newtonian cooling conditions, relatively small samples (∼200-300 cm^3) of aluminum A356 alloys with compositions given in Table 2.2 were melted in SiC crucibles. The amounts of silicon and magnesium (marked with •) were varied intentionally and measured while for all other elements, the average or maximum of their nominal content was chosen based on (Bäckerud et al., 1990). The molten alloys were poured into containers with thin insulating walls as schematically shown in Figure 2.3. The insulating walls along with small sample sizes minimized thermal gradients in the sample. The metal samples were heated to slightly more than 373.2 K (100 °C) above their respective liquidus temperature, poured into new containers and allowed to cool to at least 323.2 K (50 °C) below their solidus temperature.

Table 2.2: Chemical composition of different aluminum A356 alloys used. (Al balance)

	Element (wt%)						
	$^{\bullet}$Si	†Fe	†Cu	†Mn	$^{\bullet}$Mg	†Zn	*Ti
Alloy 1	6.40	0.12	0.10	0.05	0.24	0.05	0.20
Alloy 2	7.77	0.12	0.10	0.05	0.23	0.05	0.20
Alloy 3	6.89	0.12	0.10	0.05	0.24	0.05	0.20
Alloy 4	7.09	0.12	0.10	0.05	0.45	0.05	0.20
Alloy 5	7.12	0.12	0.10	0.05	0.37	0.05	0.20
Alloy 6	6.82	0.12	0.10	0.05	0.69	0.05	0.20
Alloy 7	7.38	0.12	0.10	0.05	0.34	0.05	0.20
Alloy 8	6.09	0.12	0.10	0.05	0.23	0.05	0.20
Alloy 9	6.79	0.12	0.10	0.05	0.26	0.05	0.20
Alloy 10	8.09	0.12	0.10	0.05	0.13	0.05	0.20

$\bullet$: measured $\dagger$: average of nominal range $\star$: maximum allowed

A single type K thermocouple recording at 10 Hz frequency was used in all of the experiments (located in the center of the fiber cup as shown in Figure 2.3). After the molten metal was poured into the cups, a fiber insulation sheet was immediately placed on top to prevent heat losses due to radiation. In addition, the entire setup was placed in a box to prevent stray air currents from affecting the heat transfer rate of the metal sample in the cups. The recorded cooling rates were of the order of 0.15 to 0.3 K/s.

Aluminum A356 was specifically chosen as an example because of it's wide industrial application, readibly available thermophysical data and the fact that it shows simultaneous solidification-precipitation reactions as shown below (Lu and Dahle, 2005; Suwanpinij et al., 2003; Bäckerud et al., 1990):

$$\begin{cases} \text{Reaction 1: } L \to Al & \text{(primary aluminum dendrites)} \sim 885.2K(612^{\circ}C) \\ \text{Reaction 2: } L \to Al + Si & \text{(Al/Si eutectic)} \sim 853.2K(580^{\circ}C) \\ \text{Reaction 3: } L \to Al + Si + Mg_2Si + Al_8FeMg_3Si_6 & \text{(eutectic+precipitates)} \sim 823.2K(550^{\circ}C) \end{cases} \tag{2.11}$$

Reaction 1 corresponds to the solidification of primary aluminum and the beginning of formation of dendrites. Reaction 2 corresponds to the formation of Al/Si eutectic. Reaction 3 corresponds to two precipitation reactions that occur nearly simultaneously. One of the reactions is the precipitation of Mg_2Si from the liquid. The other reaction is the precipitation of $Al_8FeMg_3Si_6$ (typically called "sludge" in industrial settings). Neither of these reactions is typically desirable at this stage, as sludge severely affects the mechanical properties of the final alloy (lower strength and much lower toughness), and the precipitation of Mg_2Si is desired to be in the solid state, as part of the precipitation hardening process. During these reactions, the specific heat capacity of molten aluminum, is 0.963 J/gK (Holt et al., 1999; Davis, 1990).

The role of ΔH_{13} deserves special attention and so, it is discussed in detail here. The difference in start temperature for both precipitation reactions is relatively small and undistinguishable in the experimental data collected. Thermo-Calc analysis indicates that precipitation of the sludge happens first, followed by Mg_2Si after the sample cooling progressed further 4 to10 K. Because of their near-simultaneous behavior, both precipitation reactions are treated as a single one with a heat of formation given by the following mass fraction average:

$$\Delta H_{13} = f_{\mathrm{Mg_2Si}} \Delta H_{\mathrm{Mg_2Si}} + (1 - f_{\mathrm{Mg_2Si}}) \Delta H_{\mathrm{sludge}} \tag{2.12}$$

where $\Delta H_{\mathrm{Mg_2Si}}$ and $\Delta H_{\mathrm{sludge}}$ are respectively the heat of formation of Mg_2Si and sludge and $f_{\mathrm{Mg_2Si}}$ is the mass fraction of Mg_2Si in the total amount of precipitate.

This particular alloy system in which two phases precipitate simultaneously (Mg_2Si and sludge), adds the challenge of determining the relative amount of each phase in the total amount of precipitate. In the present case, this phase balance was determined using the Scheil solidification module of Thermo-Calc software and the results are listed in

Table 2.3. In the case of single-phase precipitates, this previous thermodynamic analysis is not necessary.

Using Thermo-Calc software TTAL7 Al-alloy database v7.1, the heat of formation of Mg_2Si is $\Delta H_{\mathrm{Mg_2Si}}$=-472.1 J/g (Andersson et al., 2002) which is calculated from the average of $H_{\mathrm{Mg_2Si}} - H_L$ during precipitation of Alloy 6. The heat of formation of sludge is -47.0 J/g (Andersson et al., 2002) calculated in a similar manner to Mg_2Si. These value are consistent with the values published in (Ravi and Wolverton, 2005). Considering the final mass fractions of Mg_2Si and sludge based on Scheil model for solidification, ΔH_{13} was calculated to be in the range of -130.2 to -207.0 J/g for all the alloys presented in Table 2.2.

2.4 Results

Ten different alloys of compositions listed in Table 2.2 were studied to compare the methodology presented with computational thermodynamic analysis. For all ten alloys the evolution of phase fraction for solid aluminum and precipitates was determined with both techniques. In this section, general details of results are discussed using Alloy 6 as an example.

Figure 2.5 uses Alloy 6 to compare the results from the current methodology to both equilibrium and Scheil model for solidification obtained using Thermo-Calc. The formation of primary aluminum dendrites, eutectic and precipitates are clearly marked on this graph. Similarly, the $\{Mg_2Si+Al_8FeMg_3Si_6\}$ precipitate fraction for Alloy 6 is displayed in Figure 2.6. The precipitation of the sludge and Mg_2Si are also shown in Figure 2.6. It is worth mentioning that the solid aluminum fraction in Figure 2.5 does not reach 1 due to the formation of precipitates. For this specific alloy (Alloy 6) the final phase fraction consists of 0.9836 solid aluminum and 0.0164 precipitates.

Alloy 6 was chosen as an example due to the high fraction of precipitates which form during solidification. The final fraction of precipitates in the aluminum samples calculated by the presented method is displayed in Table 2.3. This table also includes the final equilibrium precipitate fraction and that predicted by Scheil model of solidification. The final mass fraction of Mg_2Si and the heat of formation of the precipitates are also given in Table 2.3. To test the accuracy of the methodology presented here, the final precipitate mass fractions are compared to that obtained from computational analysis for all ten alloys in Figure 2.4. This figure demonstrates the power of the proposed methodology in producing accurate results.

Table 2.3: Final mass fraction of precipitate present in aluminum A356 alloys.

	Precipitate fraction (g/g)				
	Present methodology	Equilibrium	Scheil equation	$f_{\mathrm{Mg_2Si}}$	ΔH_{13} (J/g)
Alloy 1	0.0090	0.0096	0.0084	0.201	-132.545
Alloy 2	0.0080	0.0094	0.0083	0.201	-132.572
Alloy 3	0.0087	0.0096	0.0085	0.201	-132.454
Alloy 4	0.0123	0.0129	0.0121	0.241	-149.578
Alloy 5	0.0110	0.0116	0.0110	0.197	-130.851
Alloy 6	0.0155	0.0167	0.0149	0.376	-206.992
Alloy 7	0.0106	0.0112	0.0104	0.196	-130.199
Alloy 8	0.0084	0.0094	0.0082	0.202	-132.843
Alloy 9	0.0091	0.0099	0.0088	0.199	-131.655
Alloy 10	0.0066	0.0079	0.0065	0.218	-139.744

The phase fraction evolution curves contain valuable information regarding the tranformation start/finish temperatures and the amount of each phase at these specific temperatures. Figure 2.7 schematically displays the most important information obtained from a phase fraction curve which includes the liquidus temperature, eutectic temperature and solid fraction at this temperature, precipitation temperature and solid fraction at this temperature. Table 2.4 summarizes the information obtained from the phase fraction

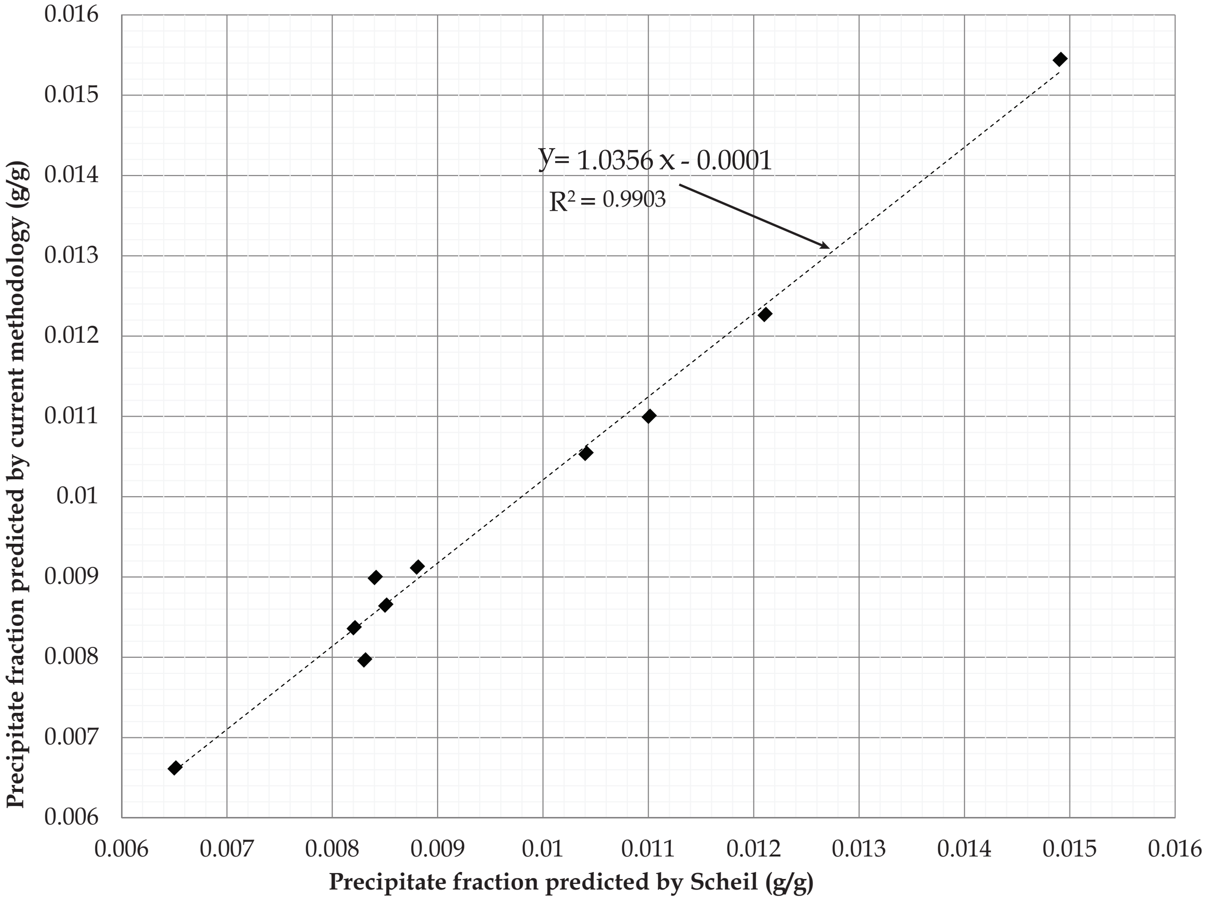

Figure 2.4: Comparison of the final precipitate mass fraction obtained from the current methodology and Scheil model for the ten alloys used in this research.

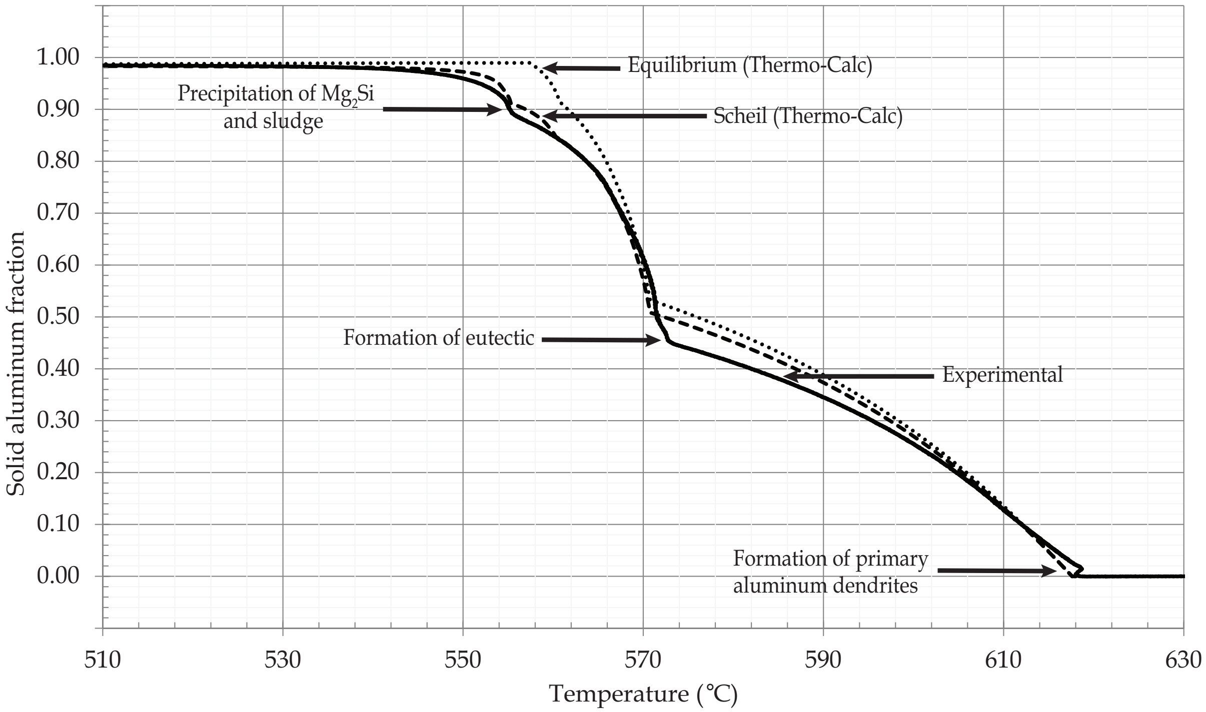

Figure 2.5: Solid aluminum fraction versus temperature for the aluminum matrix forming in Alloy 6.

curves (curves presented in Figure 2.5 and Figure 2.6) for all the alloys.

2.5 Discussion

The proposed methodology in this paper enables, for the first time, the accurate calculation of phase fractions using cooling curve analysis with multiple simultaneous phase transformations. This methodology overcomes the shortcomings of previous calorimetry approaches of assigning a single enthalpy to all transformations present.

The proposed approach involves a modest amount of effort (e.g. calculating/finding the latent heat of some phases) that is not neccessary in previous methodologies; however, this extra effort allows for the proper accounting of phase fractions that is not possible

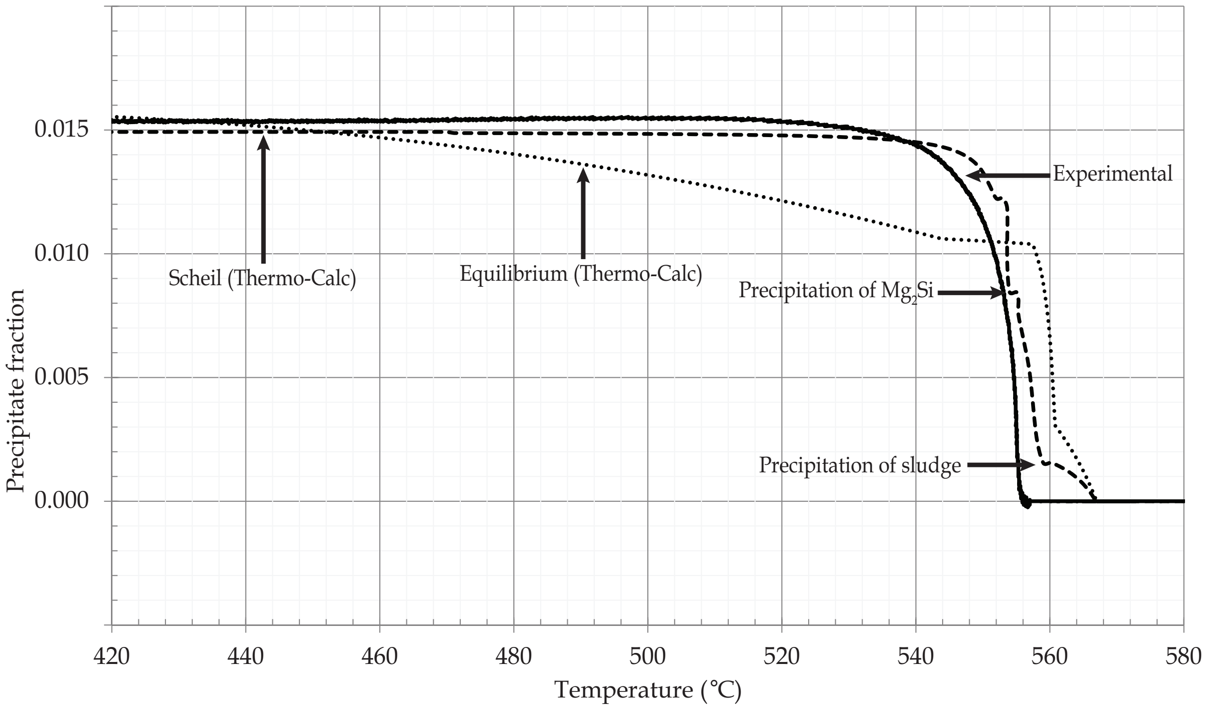

Figure 2.6: Precipitate fraction versus temperature forming in Alloy 6 during solidification.

Table 2.4: Critical information obtained from the phase fraction curves similar to Figure 2.5 and Figure 2.6 for all studied alloys.

	T_L (°C)		T_E (°C)		T_P (°C)		F_{SE} (g/g)		F_{SP} (g/g)	
	Expr.	Scheil	Expr.	Scheil	Expr.	Scheil	Expr.	Scheil	Expr.	Scheil
Alloy 1	623.8	623.0	576.3	574.0	557.6	552.8	0.511	0.538	0.975	0.971
Alloy 2	610.9	613.0	579.0	574.6	557.1	552.7	0.355	0.426	0.972	0.971
Alloy 3	620.3	619.0	576.9	574.2	556.2	552.9	0.453	0.498	0.971	0.970
Alloy 4	618.3	617.0	576.9	572.8	555.9	554.7	0.425	0.485	0.939	0.943
Alloy 5	618.3	617.0	577.3	573.4	554.5	554.2	0.432	0.481	0.932	0.954
Alloy 6	618.6	617.6	572.8	570.8	556.5	555.4	0.463	0.509	0.905	0.909
Alloy 7	617.1	615.0	578.4	573.7	557.7	554.0	0.414	0.460	0.955	0.957
Alloy 8	625.1	625.0	577.6	573.9	553.1	552.6	0.516	0.563	0.981	0.972
Alloy 9	617.5	620.0	574.9	574.0	552.7	553.1	0.454	0.507	0.978	0.968
Alloy 10	608.8	609.9	578.9	574.9	556.0	557.9	0.319	0.550	0.977	0.977

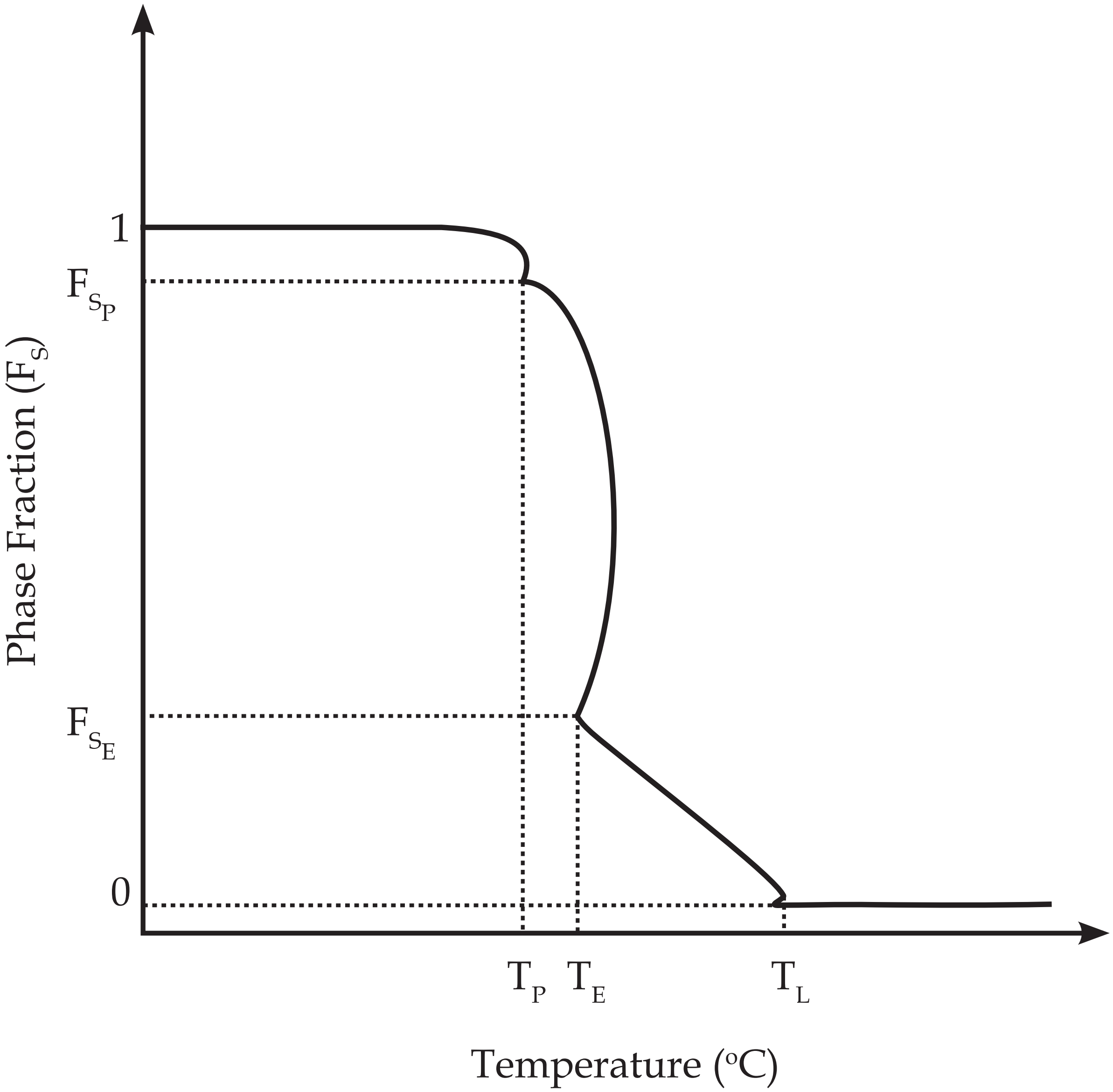

Figure 2.7: Schematic representation of the most important information obtained from a solid fraction curve.

otherwise. With the latest advancements in thermodynamic databases available through commercial software such as Thermo-Calc Software, the amount of resources spent on gathering the extra information required for this methodology is relatively small. In addition, the effort spent on analyzing a specific alloy group does not need to be repeated for similar systems; theautorefore, the analysis of experimental curves does not need independent Thermo-Calc runs for each analysis once the enthalpy of precipitates is known. By measuring the final precipitate fraction in unknown systems or systems which do not have reliable thermodynamic databases available, the enthalpies of all phase transformations involved can be accurately back-calculated. This is an advantage over relying solely on available thermodynamic databases and can be used to get a deeper understanding of new or custom alloy systems.

The phase evolution and final amount of phases correspond well to those calculated using Thermo-Calc software. The maximum deviation in the amount of precipitate is an overestimate of 7.1% (for Alloy 1). Higher accuracy might have been possible if direct measurements of all alloying elements was available.

It is worth mentioning that using aluminum A356 alloy as an example in this paper also plays a role in the accuracy of the calculated precipitate fraction. The magnitude of the latent heat of formation of the precipitates is large enough to be able to track their evolution during solidification ($\Delta H_{solidification}$ is comparable to $\Delta H_{precipitation}$).

The developed methodology can be used as a complimentary method to well-established methods currently being used to track multiple phase transformations (e.g. dilatometry) without having to change the experimental setup. In fact, by making some minor adjustments to the proposed methodology (Equation 2.1), one can take into account complex heat transfer situations where convection and radiation might coexist (such as high temperature phase transformations in a dilatometry sample). By combining CCA with other experimental techniques, new unexplored and interesting doors in the world of materials science can be opened.

2.6 Conclusions

A rigorous mathematical model for the quantification of simultaneous phase transformations in cooling curve analysis was introduced for the first time. The methodology proposed is based on the integration of cooling curves and knowledge of latent heat and specific heat of phases involved. The outcome of this methodology is an accurate accounting of multiple phase fractions as the transformations progress in continuous cooling and start/finish temperatures during cooling containing multiple simultaneous phase transformations.

The simultaneous solidification-precipitation of ten variations of aluminum A356 with magnesium and silicon content respectively ranging from 0.13 to 0.69 $wt.\%$ and 6.09 to 8.09 $wt.\%$ were analyzed using the methodology proposed. The results were in good agreement with values obtained based on the Scheil model of solidification implemented in Thermo-Calc Software TTAL7 Al-alloys database v7.1. The maximum deviation in the amount of precipitate is an overestimate of 7.1% (for Alloy 1).

The results of these examples support the presented simultaneous phase transformation methodology as a tool capable of tracking multiple simultaneous phase transformations and amount of each phase present in the material.

2.7 Acknowledgement

The authors would like to acknowledge Codes And Standards Training Institute (CASTI), MITACS and Natural Sciences and Engineering Research Council of Canada (NSERC) for their support of this work. Special gratitude to Chris Rice and Shinya Myojin who

performed the experiments.

2.8 Appendix: Evolution of solid aluminum fraction and precipitate fraction with temperature for all the alloys studied

The developed methodology was used to study the simultaneuous solidification-precipitation of all the alloys mentioned in Table 2.2. Thermo-Calc Software was used to predict the equilibrium phase fractions in each of the alloys. Scheil model for solidification was also used in Thermo-Calc Software to predict the phase fractions under non-equilibrium solidification for every alloy.

The resulting phase fraction curves consisting of a solid aluminum fraction curve and a precipitate fraction curve for each of the alloys are shown in the following figures. The data used to plot these curves is also used to extract all the important information shown in Table 2.4 during the simultaneous solidification-precipitation for each of the alloys.

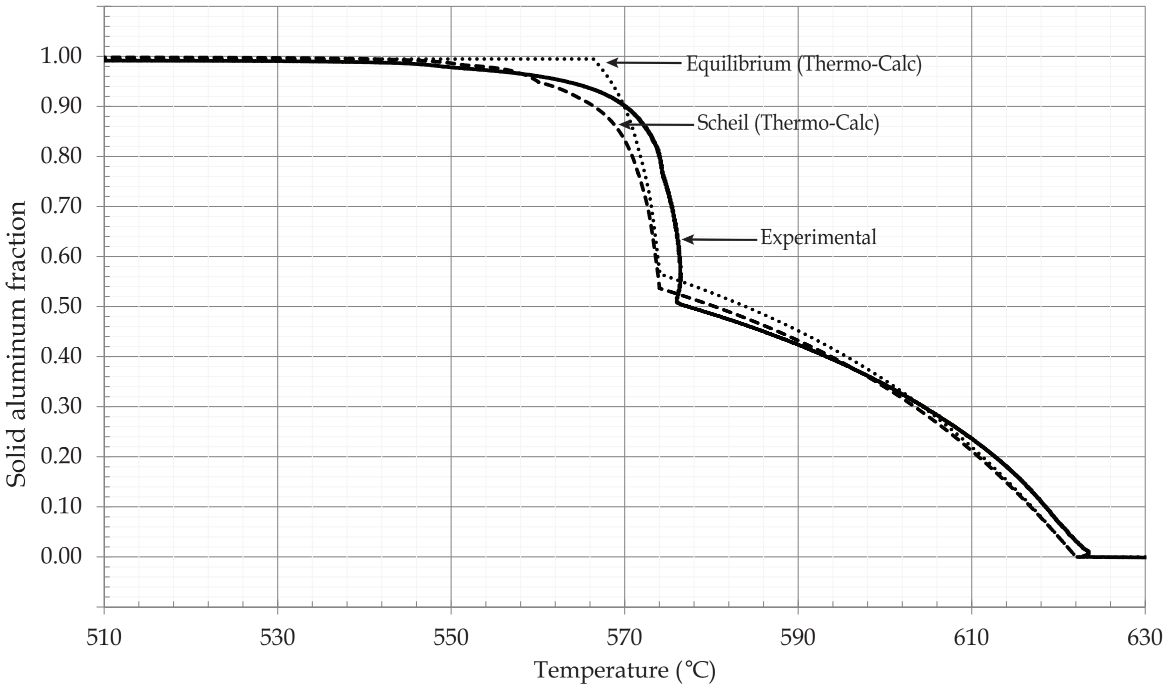

Figure 2.8: Solid aluminum fraction versus temperature for the aluminum matrix forming in Alloy 1.

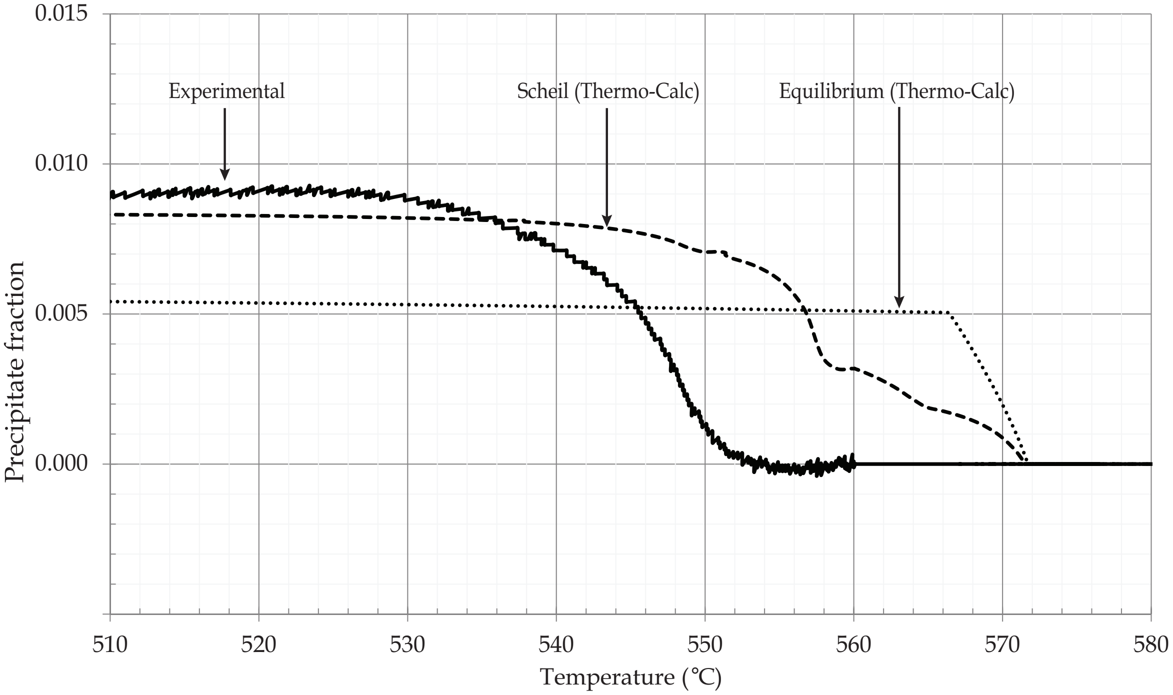

Figure 2.9: Precipitate fraction versus temperature forming in Alloy 1 during solidification.

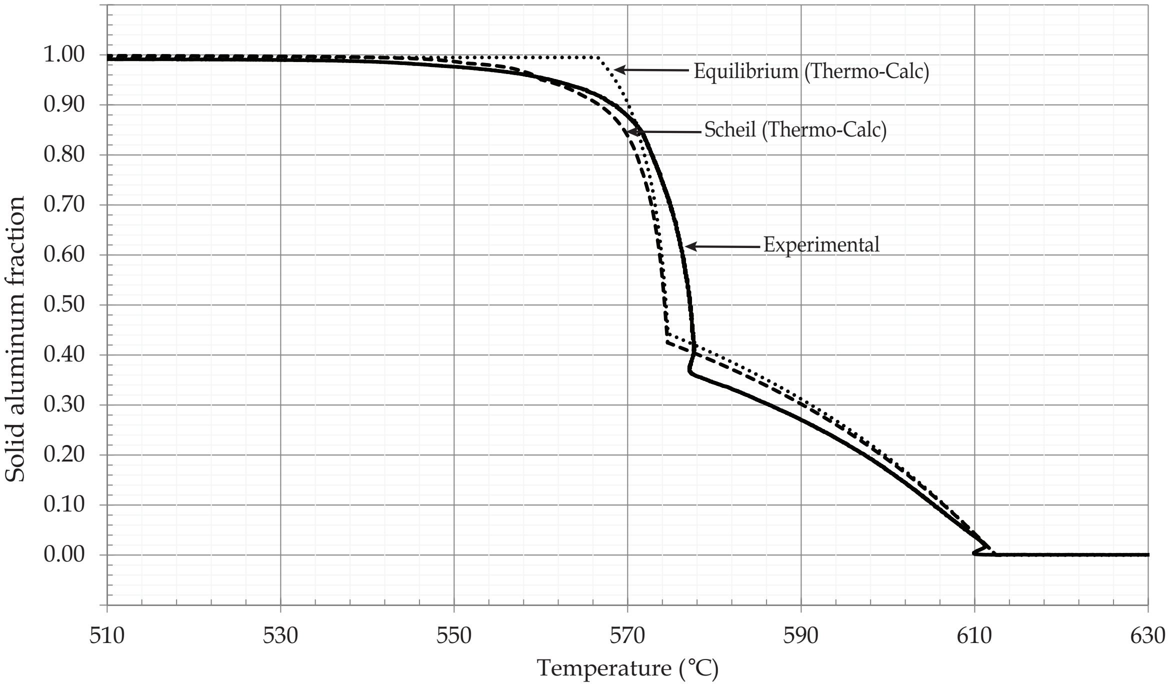

Figure 2.10: Solid aluminum fraction versus temperature for the aluminum matrix forming in Alloy 2.

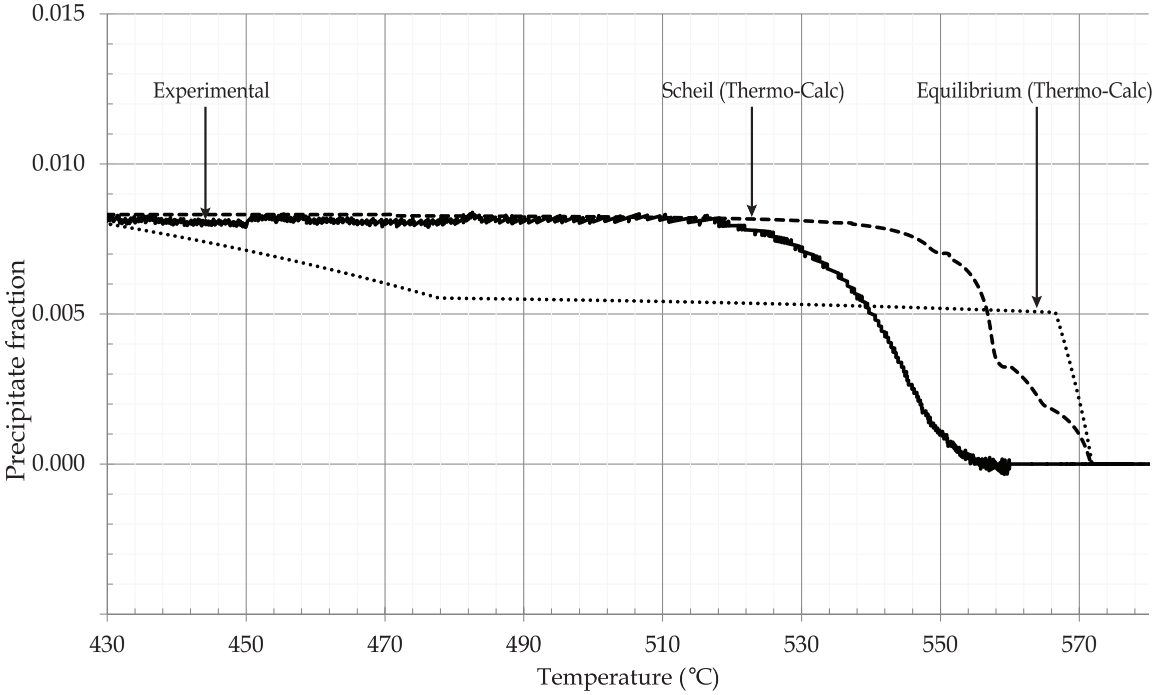

Figure 2.11: Precipitate fraction versus temperature forming in Alloy 2 during solidification.

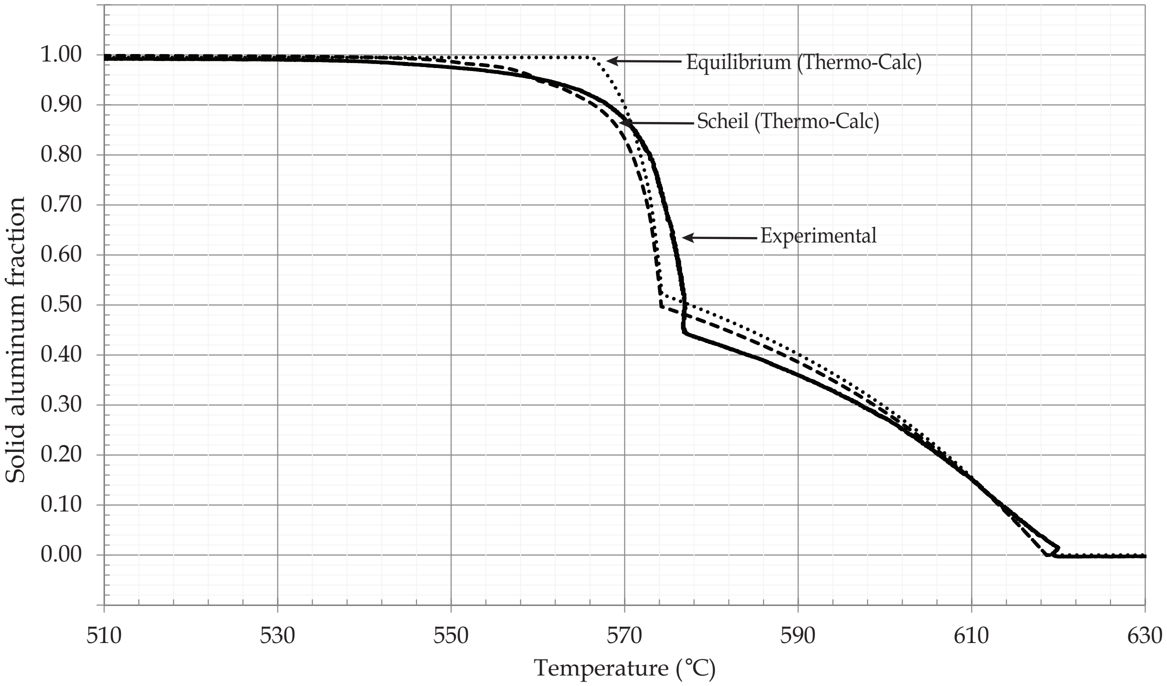

Figure 2.12: Solid aluminum fraction versus temperature for the aluminum matrix forming in Alloy 3.

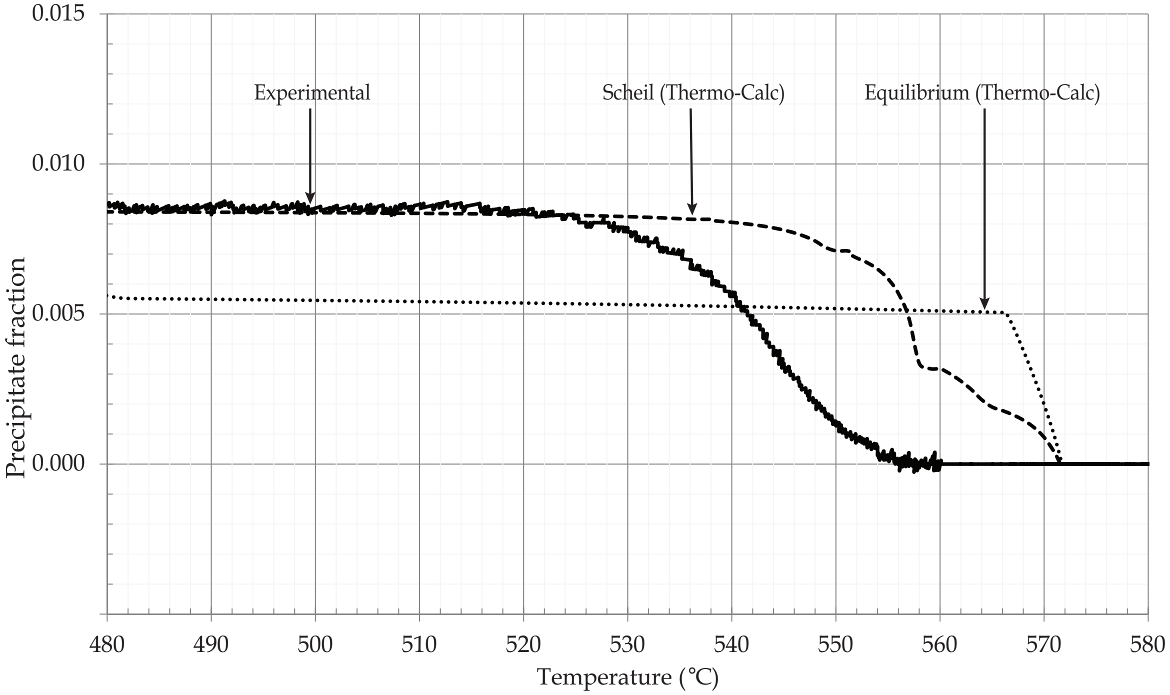

Figure 2.13: Precipitate fraction versus temperature forming in Alloy 3 during solidification.

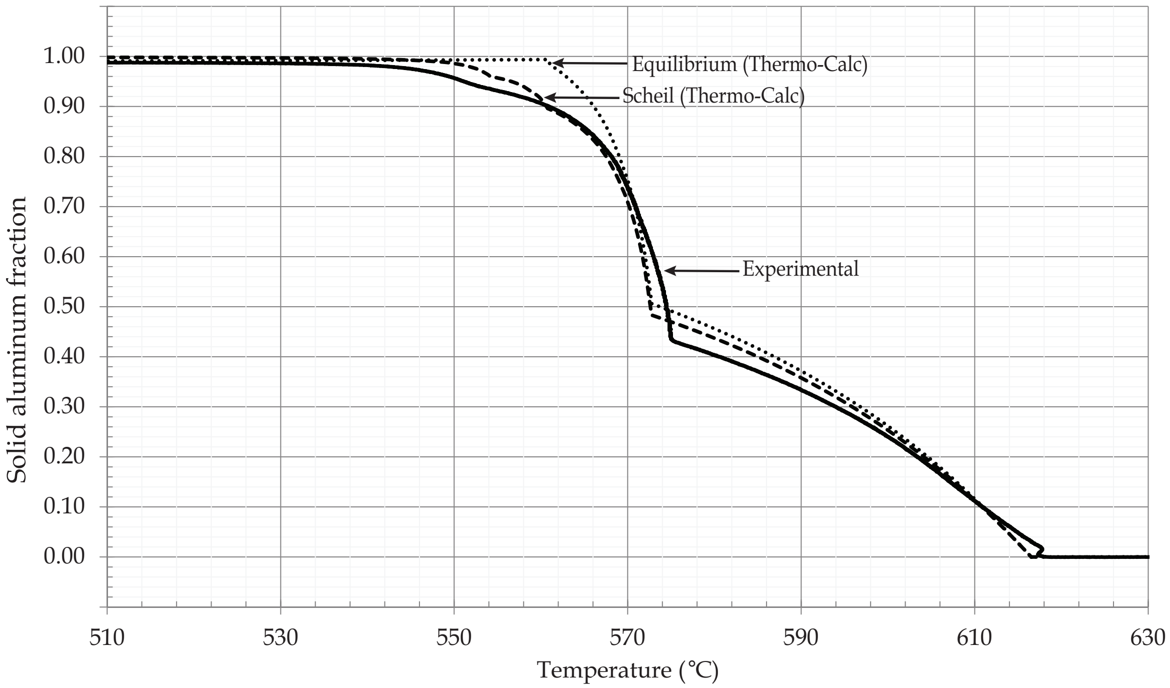

Figure 2.14: Solid aluminum fraction versus temperature for the aluminum matrix forming in Alloy 4.

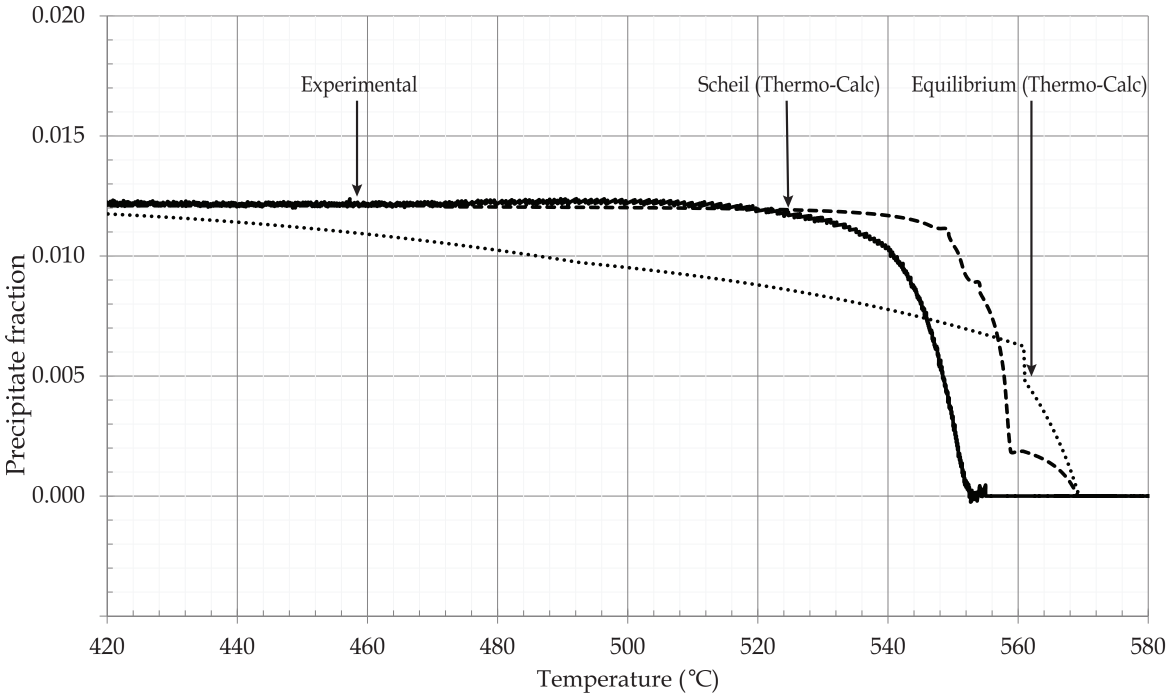

Figure 2.15: Precipitate fraction versus temperature forming in Alloy 4 during solidification.

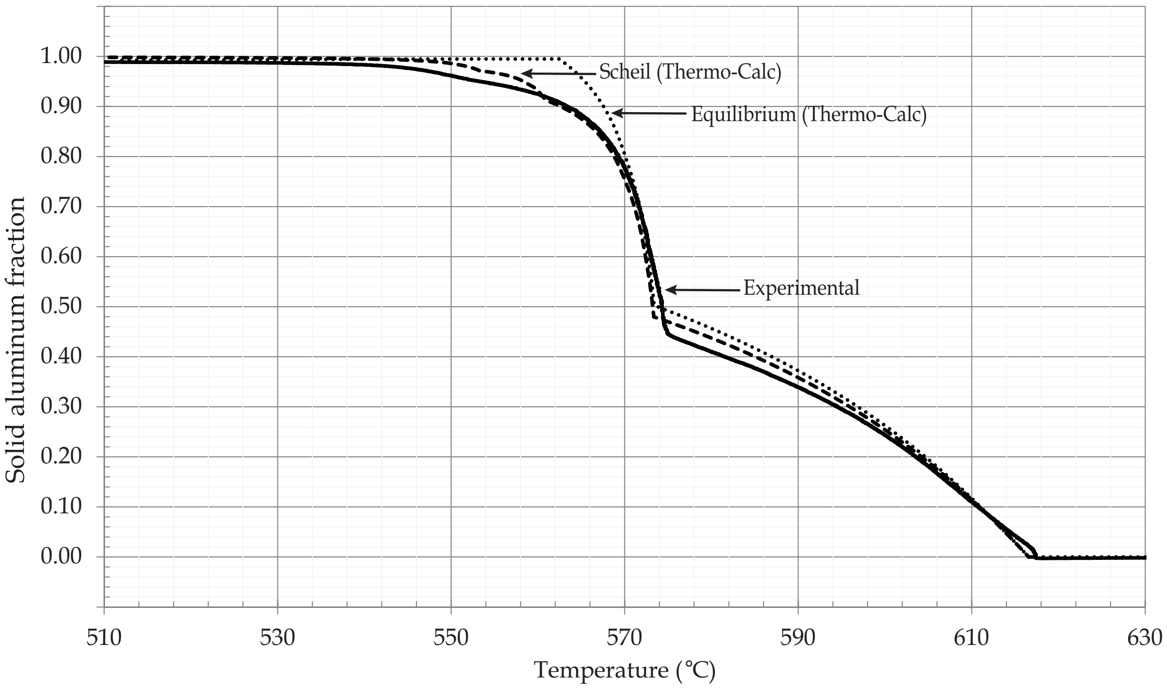

Figure 2.16: Solid aluminum fraction versus temperature for the aluminum matrix forming in Alloy 5.

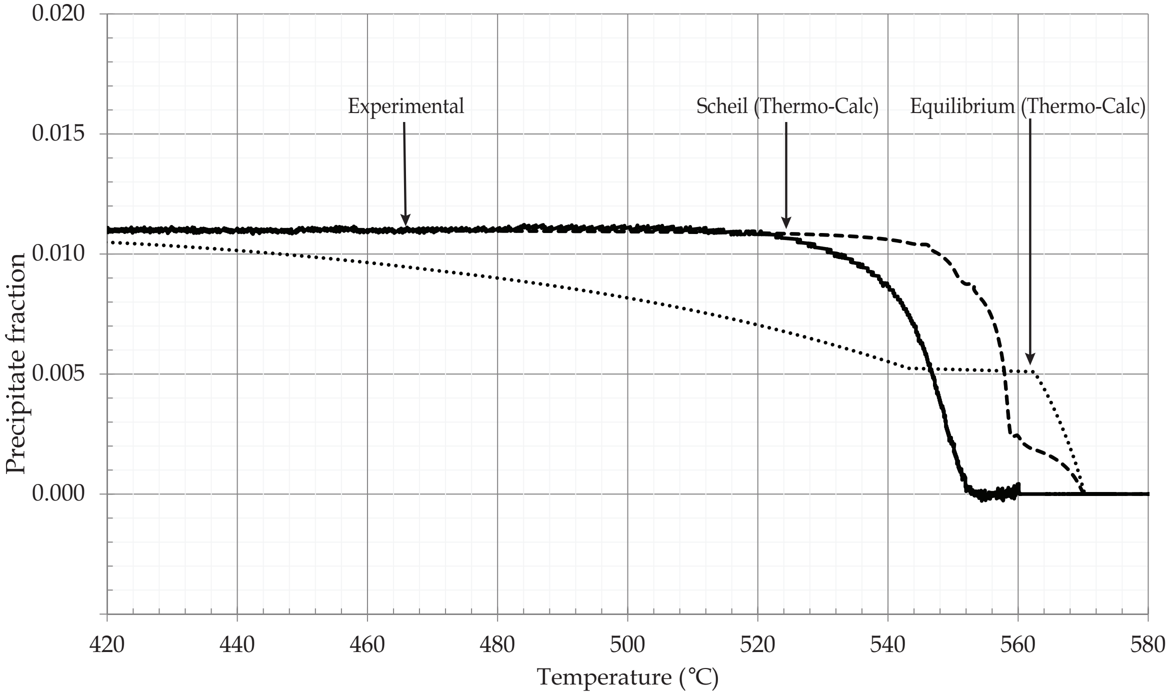

Figure 2.17: Precipitate fraction versus temperature forming in Alloy 5 during solidification.

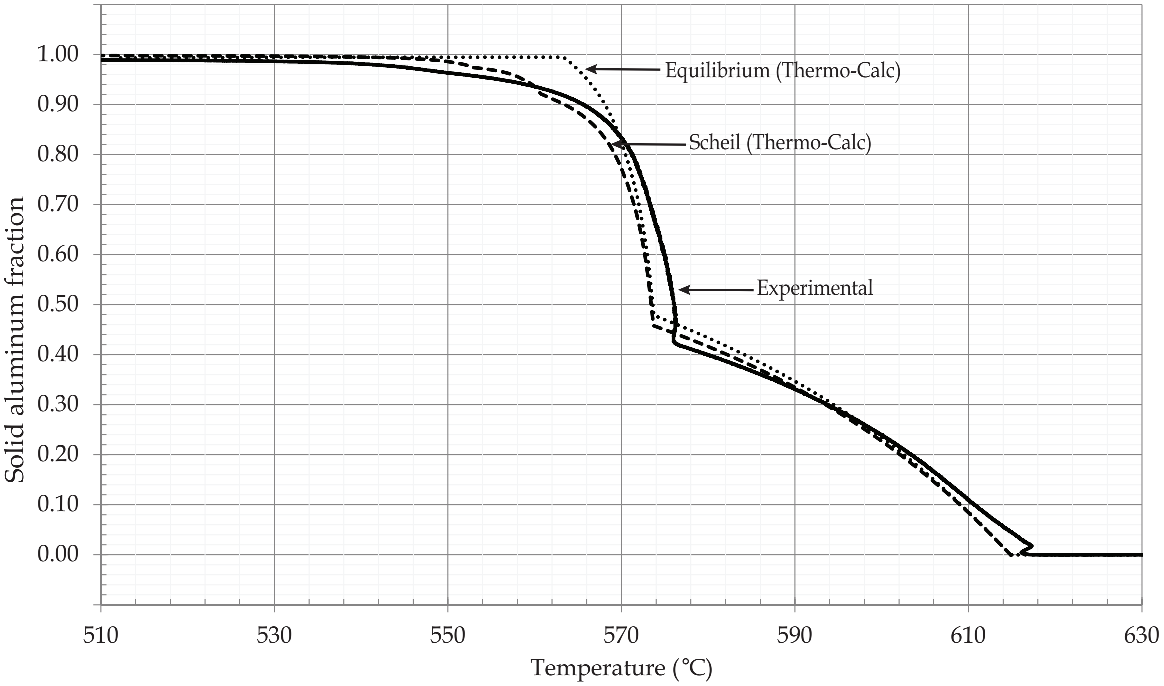

Figure 2.18: Solid aluminum fraction versus temperature for the aluminum matrix forming in Alloy 7.

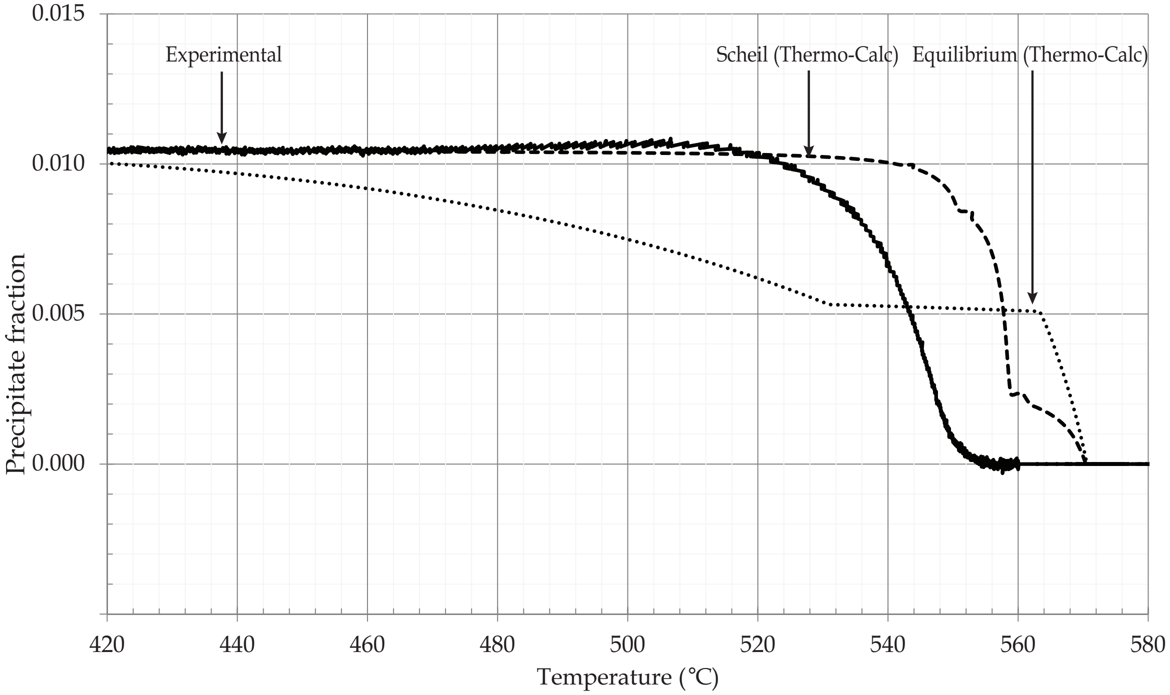

Figure 2.19: Precipitate fraction versus temperature forming in Alloy 7 during solidification.

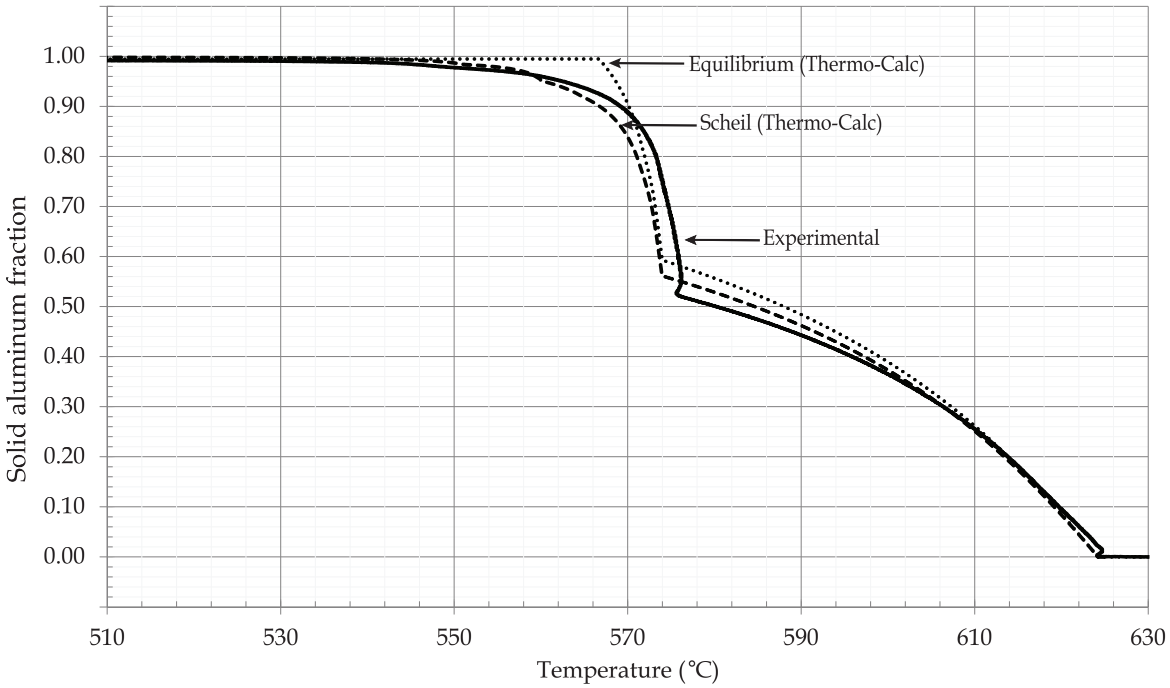

Figure 2.20: Solid aluminum fraction versus temperature for the aluminum matrix forming in Alloy 8.

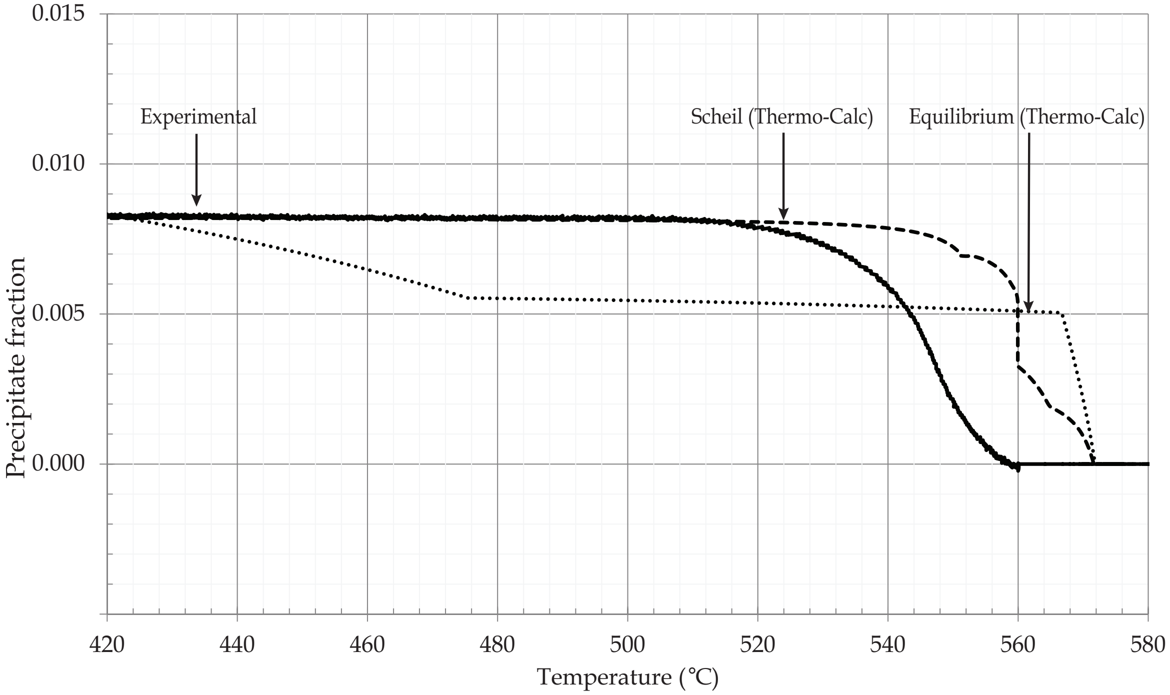

Figure 2.21: Precipitate fraction versus temperature forming in Alloy 8 during solidification.

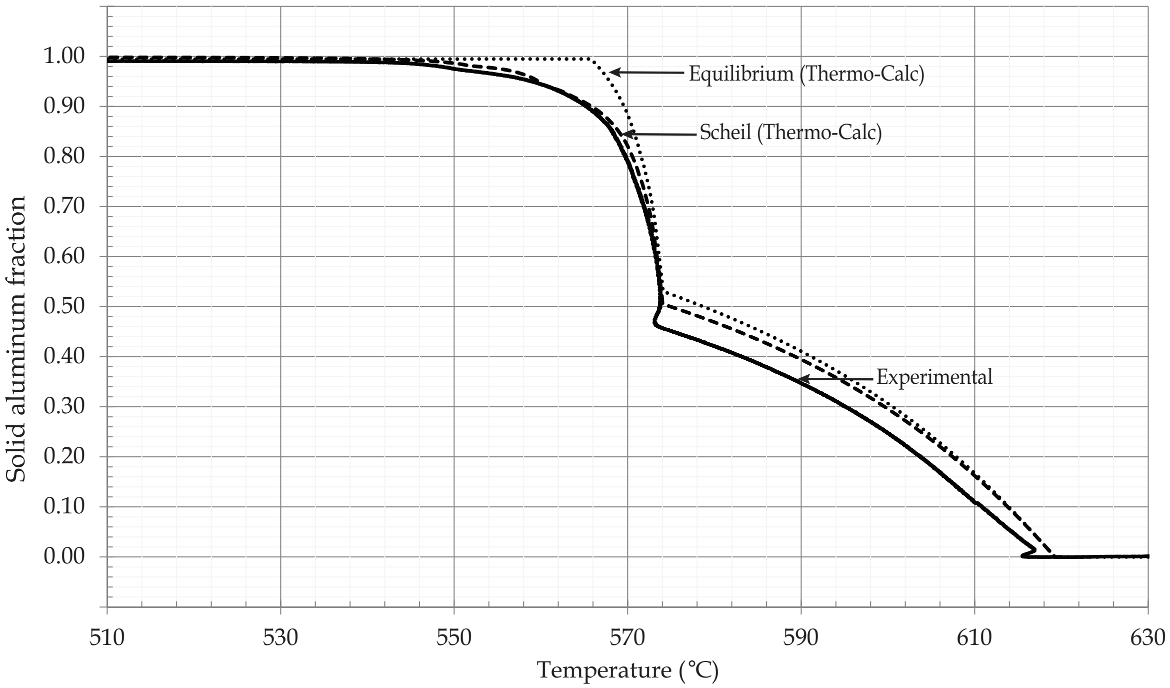

Figure 2.22: Solid aluminum fraction versus temperature for the aluminum matrix forming in Alloy 9.

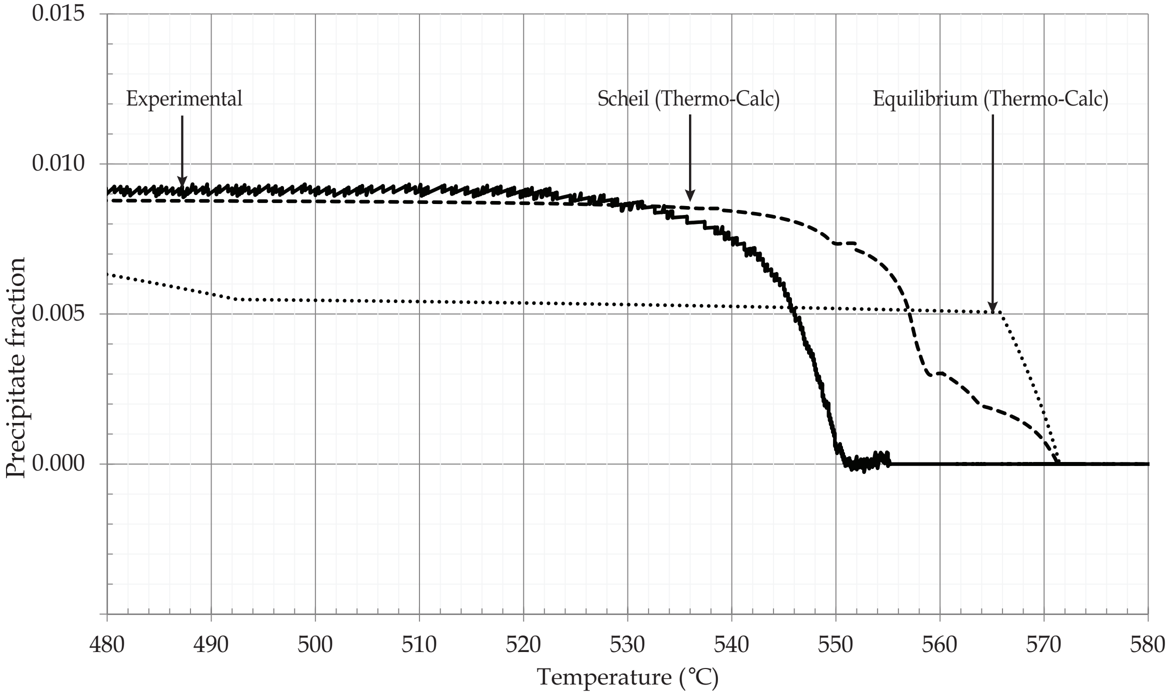

Figure 2.23: Precipitate fraction versus temperature forming in Alloy 9 during solidification.

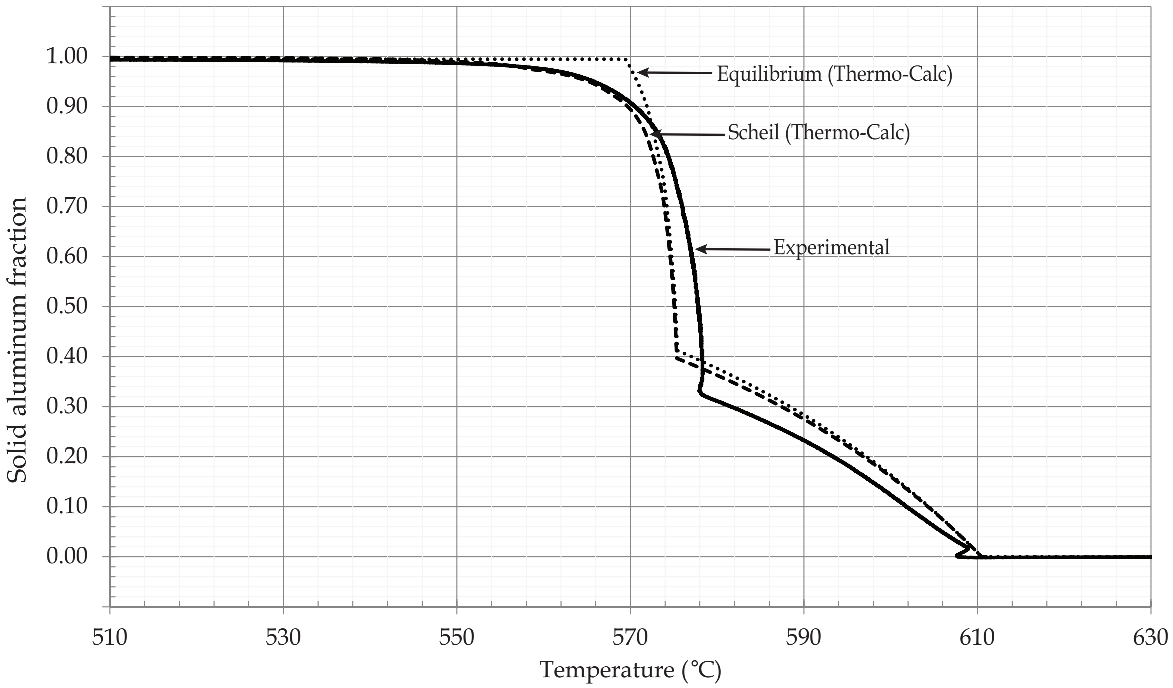

Figure 2.24: Solid aluminum fraction versus temperature for the aluminum matrix forming in Alloy 10.

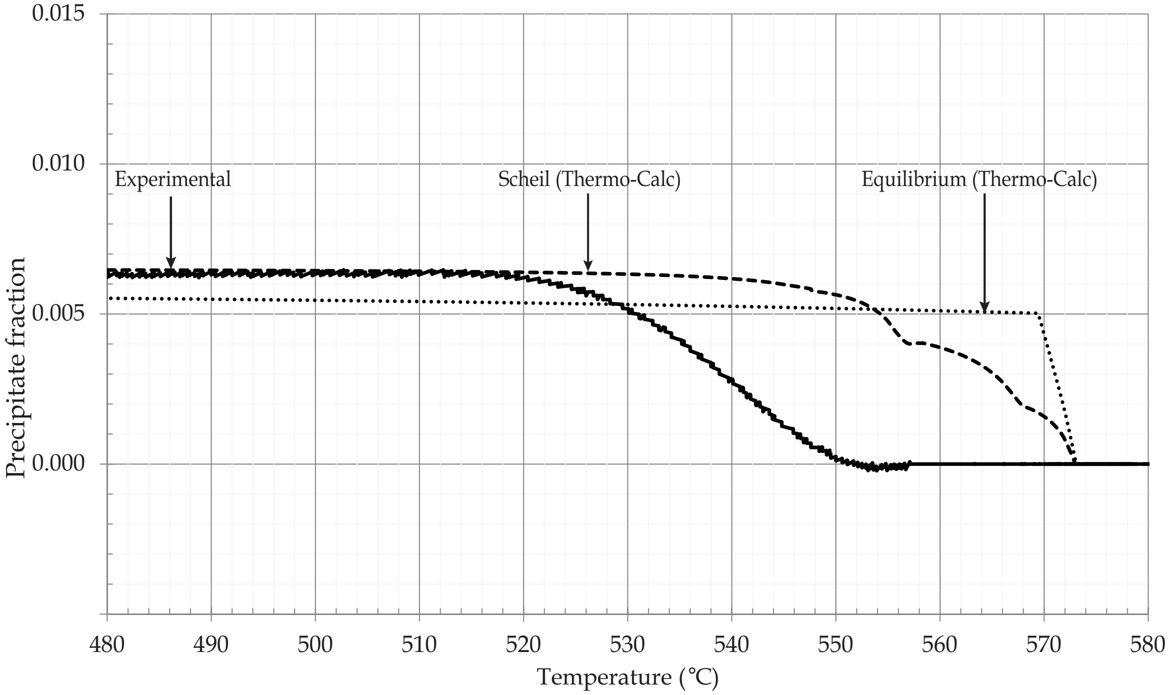

Figure 2.25: Precipitate fraction versus temperature forming in Alloy 10 during solidification.

2.9 References

Alexandrov, B.T., Lippold, J.C., 2007. Single Sensor Differential Thermal Analysis of Phase Transformations and Structural Changes During Welding and Postweld Heat Treatment. Welding in the World 51, 48–59.

Andersson, J.O., Helander, T., Hdghmd, L., Shi, P., Sundman, B., 2002. THERMO-CALC & DICTRA, Computational Tools For Materials Science. Calphad 26, 273–312.

Bäckerud, L., Chai, G., Tamminen, J., 1990. Solidification Characteristics of Aluminium Alloys: Foundry Alloys. Solidification Characteristics of Aluminum Alloys, AFS/Skanaluminium.

Bakhtiyarov, S.I., Dupac, M., Overfelt, R.a., Teodorescu, S.G., 2004. On Electrical Conductivity Measurements of Molten Metals by Inductive Technique. Journal of Fluids Engineering 126, 468–470.

Barrena, M.I., Gómez de Salazar, J.M., Pascual, L., Soria, A., 2013. Determination of the kinetic parameters in magnesium alloy using TEM and DSC techniques. Journal of Thermal Analysis and Calorimetry 113, 713–720.

Béchade, J.L., Menut, D., Doriot, S., Schlutig, S., Sitaud, B., 2013. X-ray diffraction analysis of secondary phases in zirconium alloys before and after neutron irradiation at the MARS synchrotron radiation beamline. Journal of Nuclear Materials 437, 365–372.

Bergman, T.L., Incropera, F.P., Lavine, A.S., DeWitt, D.P., 2011. Fundamentals of Heat and Mass Transfer. Wiley.

Birol, Y., 2009. Solid fraction analysis with DSC in semi-solid metal processing. Journal of Alloys and Compounds 486, 173–177.

Bojack, A., Zhao, L., Morris, P., Sietsma, J., 2012. In-situ determination of austenite and martensite formation in 13Cr6Ni2Mo supermartensitic stainless steel. Materials Characterization 71, 77–86.

Davis, J.R., 1990. Properties and selection: nonferrous alloys and special-purpose materials. ASM handbook / prepared under the direction of the ASM International Handbook Committee, ASM International.

Fornaro, O., Palacio, H.a., 2009. Study of dilute AlCu solidification by cooling curve analysis. Journal of Materials Science 44, 4342–4347.

Frankel, J.I., Porter, W.D., Sabau, A., 2005. Analysis of Volumetric Changes Through Melting Using a Dilatometer. Journal of Thermal Analysis and Calorimetry 82, 171–177.

Gibbs, J.W., 2009. Thermal Analysis Techniques for Phase Fraction Measurements of First-order Phase Transformations. Msc. Colorodo School of Mines.

Gibbs, J.W., Kaufman, M.J., Hackenberg, R.E., Mendez, P.F., 2010. Cooling Curve Analysis to Determine Phase Fractions in Solid-State Precipitation Reactions. Metallurgical and Materials Transactions A 41, 2216–2223.

Gibbs, J.W., Mendez, P.F., 2008. Solid fraction measurement using equation-based cooling curve analysis. Scripta Materialia 58, 699–702.

Gladman, T., 1997. The physical metallurgy of microalloyed steels.

Holt, J.M., Gibson, C., Ho, C.Y., for Information, P.U.C., Analysis, N.D., Synthesis, 1999. Structural Alloys Handbook. Number v. 2 in Structural Alloys Handbook, CINDAS/Purdue University.

Kiuchi, M., Sugiyama, S., 1994. A New Method to Detect Solid Fractions of Mushy/Semi-Solid Metals and Alloys. Annals of the CIRP 43, 271–274.

Kuntz, M.L., Panton, B., Wasiur-Rahman, S., Zhou, Y., Corbin, S.F., 2013. An Experimental Study of Transient Liquid Phase Bonding of the Ternary Ag-Au-Cu System Using Differential Scanning Calorimetry. Metallurgical and Materials Transactions A 44, 3708–3720.

Lu, L., Dahle, A.K., 2005. Iron-Rich Intermetallic Phases and Their Role in Casting Defect Formation in Hypoeutectic Al-Si Alloys. Metallurgical and Materials Transactions A 36, 819–835.

MacKenzie, R.C., 1970. Differential Thermal Analysis. Academic Press.

Ravi, C., Wolverton, C., 2005. Comparison of thermodynamic databases for 3xx and 6xxx aluminum alloys. Metallurgical and Materials Transactions A 36, 2013–2023.

Suwanpinij, P., Kitkamthorn, U., Diewwanit, I., Umeda, T., 2003. Influence of Copper and Iron on Solidification Characteristics of 356 and 380-Type Aluminum Alloys. Materials Transactions 44, 845–852.

Tszeng, T., Shi, G., 2004. A global optimization technique to identify overall transformation kinetics using dilatometry dataapplications to austenitization of steels. Materials Science and Engineering: A 380, 123–136.

Xu, J., Liu, F., Xu, X., Chen, Y., 2011. Determination of Solid Fraction from Cooling Curve. Metallurgical and Materials Transactions A 43, 1268–1276.

Xu, J., Liu, F., Zhang, D., 2013. In situ observation of solidification of undercooled hypoeutectic NiNi3B alloy melt. Journal of Materials Research 28, 1891–1902.

Xu, J.F., Liu, F., Zhang, D., Zhang, K., 2012. Comparison of baseline method and DSC measurement for determining phase fractions. Materials Science and Technology 28, 1420–1425.

Chapter 3

Cooling Curve Analysis as an Alternative to Dilatometry in Continuous Cooling Transformations

3.1 Introduction

Dilatometry is commonly used to quantify the progress of solid-state phase transformations during continuous heating or cooling because it gives accurate and simple to interpret results that indicate start and finish temperatures of the transformation, relative phase fraction as a function of temperature and, when combined with information about the relative densities of the two phases, it can be used to determine the absolute amount of second phase formed as a function of temperature (Tszeng and Shi, 2004; Farahat, 2008; Bojack et al., 2012; Kiani-Rashid and Edmonds, 2008).

One of the downsides of dilatometry is that it requires specialized equipment to make precise length/diameter measurements; this can be a limitation if one does not have access to a dilatometer or if a dilatometer is incompatible with a concurrent experiment (e.g. a tensile test or a synchrotron experiment). One proposed alternative method that has a significantly simpler experimental setup is cooling curve analysis (CCA); a technique that involves measuring the temperature of a sample as it cools and transforms, then using the transformation-induced deviations from single-phase cooling behavior to determine the phase fraction evolution (Gibbs and Mendez, 2008; Gibbs et al., 2010).

The goal of both dilatometry and CCA is to obtain phase fraction evolution information of a material as it undergoes monotonic heating or cooling. Because of the similarities in the results and sample conditions during the experiment, dilatometry and CCA can be seen as complimentary techniques; however, there has never been a published, quantitative comparison of the two. This work is intended to provide an initial comparison for one type of transformation.

For the comparison between the two methods, an austenite to martensite transformation is used because this is a common transformation to be analyzed using dilatometry. Dilatometry and CCA techniques are well suited to this type of transformation because both methods provide information on both the formation temperature and the amount formed as a function of temperature. The properties of the transformed martensite depend on the temperature at which it forms and the properties of the alloy depend upon the properties and amount of martensite present. The results of this comparison should also be applicable to other first-order phase transformations such as precipitation transformations.

Although the following methods are not the focus of this paper, it is important to consider alternate techniques that are available to measure phase fraction and also to note how these techniques compare to dilatometry and CCA. Differential thermal analysis (DTA) methods (MacKenzie, 1970), including single-sensor DTA (Alexandrov and Lippold, 2007), are useful for measuring the start and finish temperatures of a transformation but not the phase fractions. Differential scanning calorimetry (DSC) can be used for very precise measures of the enthalpy evolution of a transformation, which can be used to calculate phase fraction evolution similarly to CCA methods. A major drawback associated with DTA and DSC is that the small sample size is not statistically representative of real size components and the rates of heating and cooling are limited unlike CCA (Tamminen, 1988).

There are also indirect ways of measuring phase fraction evolution, such as measuring the electrical conductivity (Kiuchi and Sugiyama, 1994) or magnetic properties (Bakhtiyarov et al., 2004) and correlating their change to a change in phase fraction, similarly to how length change is used as a proxy for phase change information in dilatometry (Frankel et al., 2005). It is also important to note that the CCA method that is presented here is just one of several CCA techniques that are all based on similar principles (Tamminen, 1988; Stefanescu et al., 1990).

The innovative aspect presented in this paper resides on the rigorous mathematical formulation which allows for the extension of this methodology to other problems, including multiple simultaneous transformations. This paper has also extended the mathematical framework to provide a rigorous analysis of dilatometric data.

3.2 Dilatometry

The dilatometry analysis presented here involves developing a model that contains the collected data and terms that are either dependent on temperature or phase fraction (but not both); then using the collected data to determine values for the temperature dependent terms; and finally, solving for the phase fraction.

This new methodology for analyzing dilatometry data is proposed that is consistent with typical line-drawing techniques but is more mathematically rigorous. It also provides a unified framework that can also be used for the cooling curve analysis that is presented in the next section.

3.2.1 Material model

Considering a two constituent system, the total volume of the sample is $V = \sum_{i=1}^{n} V_i = V_\alpha + V_\beta$. The constituent volumes (V_i) can be calculated from their mass fraction and density ($V_i = m_T f_i/\rho_i$), where f_i is the mass fraction of constituent i, $f_i = m_i/m_T$, ρ_i is the density of constituent i and m_T is the total mass of the sample. Applying these considerations results in:

$$V_T = m_T(\frac{f_\alpha}{\rho_\alpha} + \frac{f_\beta}{\rho_\beta}) \tag{3.1}$$

The total mass of the sample in Equation 3.1 can be represented by the initial density and volume of the sample as $m_T = \rho_0 V_0$. To quantify the progression of constituents as a function of temperature, it is useful to create a differential equation by differentiating Equation 3.1 with respect to temperature to obtain:

$$\frac{1}{V_0}\frac{dV}{dT} = \left(f_\alpha \frac{\partial \lambda_\alpha}{\partial T} + \lambda_\alpha \frac{\partial f_\alpha}{\partial T} + f_\beta \frac{\partial \lambda_\beta}{\partial T} + \lambda_\beta \frac{\partial f_\beta}{\partial T} \right) \tag{3.2}$$

where $\lambda_i \equiv \rho_0/\rho_i$. The summation of all mass fractions adds to unity: $\sum_{i=1}^{n} f_i = 1$. Equation 3.2 can be rearranged considering the relationship between linear and volumetric thermal expansion coefficients (i.e. $\beta = 3\alpha$, where $\beta \equiv \frac{1}{V}\frac{dV}{dT}$) which will yield $\frac{1}{V_0}\frac{dV}{dT} = \frac{3V}{V_0 L}\frac{dL}{dT}$. For isotropic materials the ratio $V/V_0 = (L/L_0)^3$:

$$3\left(\frac{L}{L_0}\right)^2 \frac{1}{L_0}\frac{dL}{dT} = (1 - f_\beta)\frac{\partial \lambda_\alpha}{\partial T} + f_\beta \frac{\partial \lambda_\beta}{\partial T} - (\lambda_\alpha - \lambda_\beta)\frac{\partial f_\beta}{\partial T} \tag{3.3}$$

where L_0 is the initial length of the sample. For a typical material, the factor $(\mathrm{L}/\mathrm{L}_0)^2$ is very close to unity. Equation 3.3 can then be rearranged as:

$$\frac{dL}{dT} = \mathcal{L}_\alpha(1 - f_\beta) + \mathcal{L}_\beta f_\beta - C_{\Delta\lambda}\frac{\partial f_\beta}{\partial T} \tag{3.4}$$

where $\mathcal{L}_i \equiv \frac{L_0}{3}\frac{\partial \lambda_i}{\partial T}$ and $C_{\Delta\lambda} \equiv L_0(\lambda_\alpha - \lambda_\beta)/3$. The definition of $\mathcal{L}_i$ at this stage is to gather all the terms related to constituent i in a single parameter that can be tracked when fitting to experimental data discussed later on.

3.2.2 Determining f_β-independent terms

All the $\mathcal{L}_i$ terms in Equation 3.4 are functions of temperature. The variations of $C_{\Delta\lambda}$ with temperature are proportional to the difference $(\lambda_\alpha - \lambda_\beta)$. For typical materials, $\lambda_\alpha - \lambda_\beta$ is much smaller than either λ_α or λ_β and $C_{\Delta\lambda}$ is considered as independent of temperature. In determining the values of these terms, it is important to keep in mind what the phase fractions represent. For some transformations, such as solidification, the definition is very straight forward: f_α is the liquid fraction and f_β is the solid fraction and the system will start at $f_\beta = 0$ and finish at $f_\beta = 1$. For other transformations, such as martensite formation from austenite, it is mathematically more convenient to let f_α represent the fraction of pre-transformation constituent and f_β represent the fraction of post-transformation product. For example, in a martensite transformation that yields a maximum of 40% martensite that is half way through the transformation, there would be 20% martensite and $f_\beta = 0.5$. Using this definition of the phase fractions, the values for the $\mathcal{L}_i$ terms can be determined by considering Equation 3.4 either before or after the transformation takes place. Before the transformation, when the system is comprised entirely of α and no transformation is occurring ($f_\beta = 0$ and $\partial f_\beta/\partial T = 0$), Equation 3.4

becomes:

$$\frac{dL}{dT} = \mathcal{L}_\alpha \tag{3.5}$$

A similar argument can be used to relate the measured length (L) to $\mathcal{L}_\beta$ after the transformation has occurred and these terms can be easily computed from the measured data. Determining a value for $C_{\Delta\lambda}$ is done by first assuming a reasonable value, then proceeding with this analysis to obtain a phase fraction evolution curve that begins at $f_\beta = 0$ and ends at some value of f_β other than 1. Since the transformation proceeds to $f_\beta = 1$ by definition, the calculated values of f_β after the transformation can be used to make an improved evaluation of $C_{\Delta\lambda}$. This process is iterated until $f_\beta = 1$ after the transformation is complete.

3.2.3 Determining phase fractions

Equation 3.4 can be rearranged to pose it as a differential equation for phase fraction evolution as follows:

$$\frac{\partial f_\beta}{\partial T} = \frac{1}{C_{\Delta\lambda}} \left[\mathcal{L}_\alpha \left(1 - f_\beta\right) + \mathcal{L}_\beta f_\beta - \frac{dL}{dT} \right] \tag{3.6}$$

Equation 3.6 can be numerically integrated, starting from an initial condition of $f_\beta = 0$, using an explicit Euler integration scheme as shown below:

$$f_\beta^{n+1} = f_\beta^n + \frac{T^{n+1} - T^n}{C_{\Delta\lambda}} \left[\mathcal{L}_\alpha^n \left(1 - f_\beta^n\right) + \mathcal{L}_\beta^n f_\beta^n - \frac{L^{n+1} - L^n}{T^{n+1} - T^n} \right] \tag{3.7}$$

3.3 Cooling curve analysis

The thermal analysis technique presented here was originally presented in (Gibbs and Mendez, 2008; Gibbs et al., 2010). This technique is similar to that presented for dilatometry in which a model is proposed that describes the enthalpy of the sample using terms that are functions of either temperature or phase fraction, solving for the temperature dependent terms, then determining the phase fraction.

The primary difference between the dilatometry and cooling curve analysis is that the dilatometry model is based on the length of the sample, which is measured directly, whereas the thermal model is based on the enthalpy of the sample, which must be inferred by using a heat transfer model.

3.3.1 Thermal model

The thermal model assumes two phases are present and the total enthalpy of the sample can be described by a sum of the enthalpies of the individual phases ($H = H_\alpha + H_\beta$). Similarly to the dilatometry analysis, the enthalpy terms are split to separately account for changes in the enthalpy of the phase that are due to a change in the amount of the phase and changes that are due to variations in the specific enthalpy of the phase.

$$H = m_\alpha H^*_\alpha + m_\beta H^*_\beta \tag{3.8}$$

By further splitting the masses of the individual phases into total system mass and phase fraction, and differentiating Equation 3.8 with respect to temperature, the following equation is obtained:

$$\frac{dH}{dT} = m\left(\frac{\partial f_\alpha}{\partial T}H^*_\alpha + f_\alpha\frac{\partial H^*_\alpha}{\partial T}\right) + m\left(\frac{\partial f_\beta}{\partial T}H^*_\beta + f_\beta\frac{\partial H^*_\beta}{\partial T}\right) \tag{3.9}$$

This equation can be simplified by rearranging terms and using the properties of a two phase system similar to what was done in the dilatometry section. It is also convenient to replace the enthalpy differentials with thermodynamic quantities, namely specific heat capacity (c_p) and heat of transformation (ΔH^*).

$$\frac{dH}{dT} = mc_p^\alpha \left(1 - f_\beta\right) + mc_p^\beta f_\beta - m\Delta H^* \frac{\partial f_\beta}{\partial T} \tag{3.10}$$

To relate dH/dT to the observed temperatures in the experiment, a heat transfer relationship is used. Depending on the dominant cooling mechanism, a relationship describing conduction, convection or radiation is used; for this particular set of experiments, the following convection dominant equation is used:

$$\frac{dH}{dt} = \bar{h}A\left(T - T_\infty\right) \tag{3.11}$$

This is related to Equation 3.10 by multiplying the left hand side of Equation 3.11 by $\left(dT/dt\right)^{-1}$ to obtain a dH/dT term, then replacing dH/dT by the right hand side of Equation 3.10 to get

$$\frac{dT}{dt}\left[mc_p^\alpha \left(1 - f_\beta\right) + mc_p^\beta f_\beta - m\Delta H^* \frac{\partial f_\beta}{\partial T}\right] = \bar{h}A\left(T - T_\infty\right) \tag{3.12}$$

3.3.2 Determining f_β-independent terms

In its present form, Equation 3.12 contains six unknowns: m, ΔH^*, c_p^α, c_p^β, $\bar{h}$ and A. It is intractible to solve for each of them individually. Since all these variables are functions of temperature and not phase fraction, it is possible to combine them into just three variables using the following definitions:

$$\gamma_\alpha = \frac{mc_p^\alpha}{\bar{h}A} \qquad \gamma_\beta = \frac{mc_p^\beta}{\bar{h}A} \qquad C_{\Delta H} = \frac{m\Delta H^*}{\bar{h}A} \tag{3.13}$$

Using these variables, Equation 3.12 becomes:

$$\gamma_\alpha \frac{dT}{dt}\left(1 - f_\beta\right) + \gamma_\beta \frac{dT}{dt} f_\beta - C_{\Delta H}\frac{df_\beta}{dt} = \left(T - T_\infty\right) \tag{3.14}$$

Where γ_α and γ_β are functions of temperature due to the temperature dependence of the specific heat capacity and $C_{\Delta H}$ is a constant. These new parameters can be evaluated by considering Equation 3.14 when no transformation is occurring. For example, before the transformation begins $f_\beta = 0$ and $df_\beta/dt = 0$ and Equation 3.14 becomes

$$\gamma_\alpha = \left(\frac{dT}{dt}\right)^{-1}\left(T - T_\infty\right) \tag{3.15}$$

This equation provides a unique relationship that allows the variable γ_α to be related to and fitted to the collected temperature data. A similar procedure can be done after the transformation occurs to obtain a relationship for fitting γ_β. To determine a value for $C_{\Delta H}$, a similar procedure to the dilatometry analysis is used.

3.3.3 Determining phase fractions

To determine phase fractions, Equation 3.14 is rearranged to isolate df_β/dt as follows:

$$\frac{df_\beta}{dt} = \frac{1}{C_{\Delta H}}\left[\gamma_\alpha \frac{dT}{dt}\left(1 - f_\beta\right) + \gamma_\beta \frac{dT}{dt} f_\beta - \left(T - T_\infty\right)\right] \tag{3.16}$$

Table 3.1: Chemical composition of 9Cr3W3CoVNbBN test melt in wt.% (balance Fe)

Element	C	Si	Mn	Cr	W	V	Nb	Co	Al	B	N
Amount	0.09	0.3	0.51	9.26	2.92	0.2	0.05	2.88	0.004	0.0114	0.01

This equation is then discretized and numerically integrated using an explicit Euler integration scheme with an initial condition of $f_\beta = 0$:

$$f_\beta^{n+1} = f_\beta^n + \frac{t^{n+1} - t^n}{C_{\Delta H}} \left[\gamma_\alpha \frac{T^{n+1} - T^n}{t^{n+1} - t^n} \left(1 - f_\beta^n\right) + \gamma_\beta \frac{T^{n+1} - T^n}{t^{n+1} - t^n} f_\beta^n - \left(T^{n+1} - T_\infty\right) \right] \quad (3.17)$$

3.4 Experimental setup

A simultaneous dilatometry and cooling curve analysis experiment was performed on a 9Cr3W3CoVNb steel with controlled additions of 120ppm boron and 130ppm nitrogen produced by vacuum induction melting (VIM) in order to compare the results between the two methods. Table 3.1 shows the exact chemical composition of the steel in weight percent (wt%).

After the melting process the ingot (110 by 110 mm square) was rolled to 20 mm thick plates. The heat treatment consisted of normalizing at 1150°C for 1 hour followed by tempering at 770°C for 4 hours. To reveal the microstructure of the base material (before dilatometry) the surface of the samples was subsequently ground using silicon carbide paper down to grit 4000 and polished in two steps using a cloth coated with 3 and 1μm diamond suspensions. The polished samples were etched using a modified LBII etchant. Optical micrographs of the base materials are shown in Figure 3.1. The base material shows a tempered martensitic structure with a homogeneous polygon prior austenite grain structure with an average grain size of 300μm.

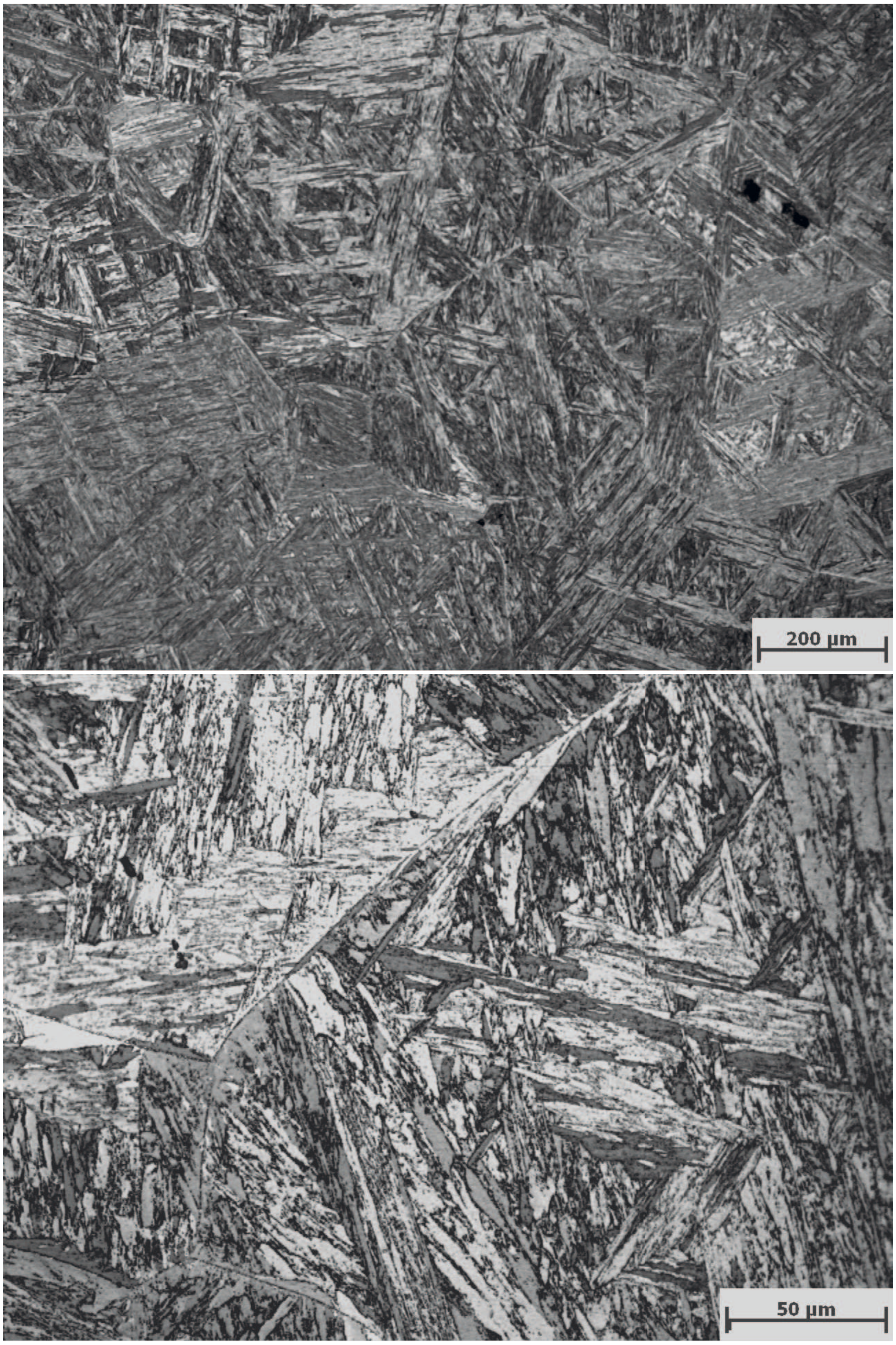

Figure 3.1: Optical micrographs of the 9Cr3W3CoVNb steel microstructure after heat treatment and before dilatometery.

3.4.1 Dilatometry setup

For the dilatometry investigations a Bahr DIL-805/D dilatometer was utilized. Cylindrical specimens of the 9Cr3W3CoVNb base material with a diameter of 4mm and a length of 10mm were used. Figure 3.2 shows the experimental setup of the dilatometer and the sample chamber.

The dilatometry temperature cycle is characterized by a heating rate of $10K/s$, a peak temperature of 1100°C, a holding time of 3 seconds, and free cooling. The dilatometer is used to precisely record the change in length of the sample as it is heated and cooled with time. In addition, variations of temperature with time are also recorded using the same setup. The recorded change in length and temperature with respect to time for the cooling section of the presented heat treatment are shown in Figure 3.3.

The recorded data for the change in length (with respect to the initial length of the sample) can be plotted against the temperature. This plot is useful in determining whether the parent phase has transformed into a new phase during cooling (change in slope of the plot) and if so, the start and end temperatures of the new phase(s) (point of deviation from the original slope). The corresponding dilation curve for the cooling section of the heat treatment is shown in Figure 3.4. The onset (AC_1) and completion (AC_3) of austenite formation take place at 895°C and 980°C, respectively. The measured martensite start (M_S) and finish (M_F) temperatures are 400°C and 240°C, respectively.

After the dilatometry experiments, the microstructure of the samples was analyzed again. Figure 3.5 represents the final microstructure of the steel samples after the thermal cycle. The material shows a martensitic microstructure with approximately 4% retained austenite (based on X-ray diffraction data discussed in detail in (Mayr et al., 2010; Mayr,

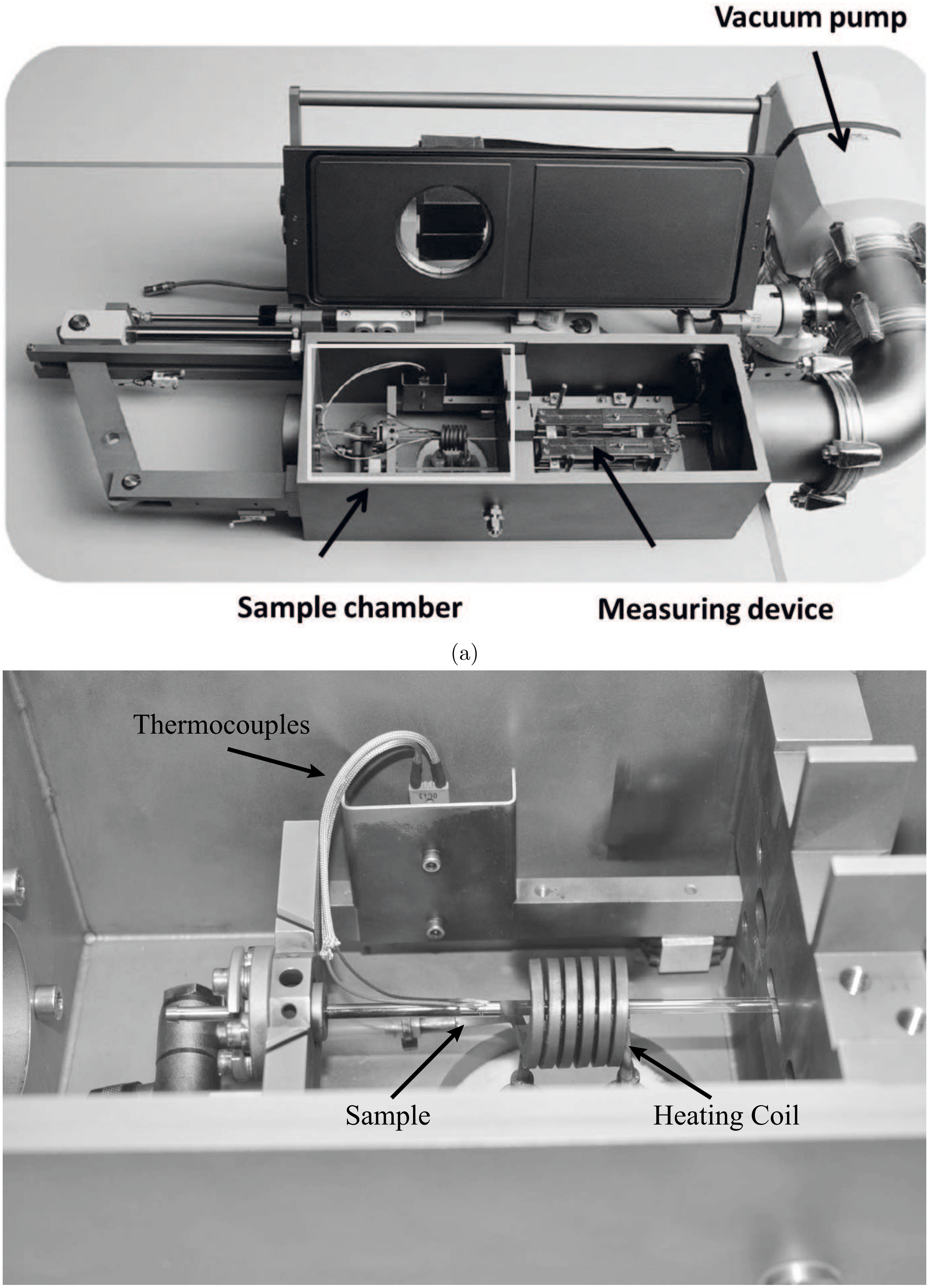

(a)

(b)

Figure 3.2: Experimental setup of the (a) dilatometer (b) sample chamber.

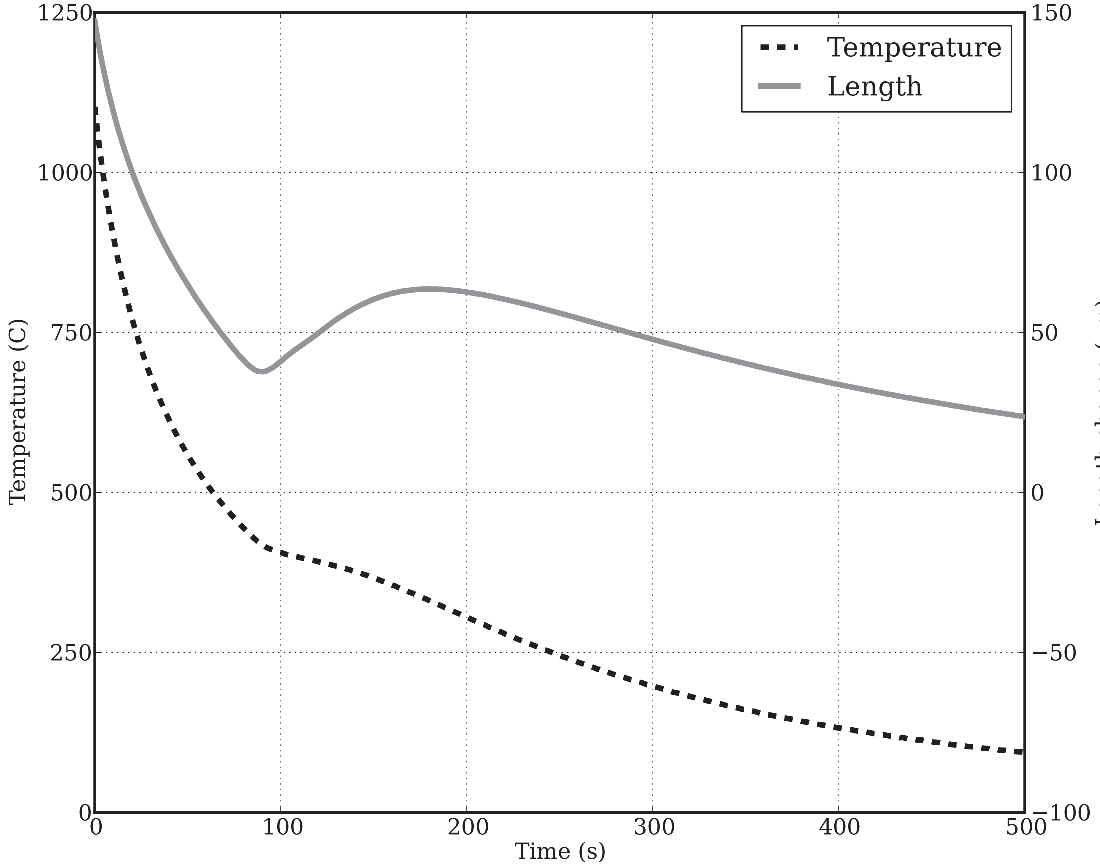

Figure 3.3: Temperature and length change relative to the room temperature length.

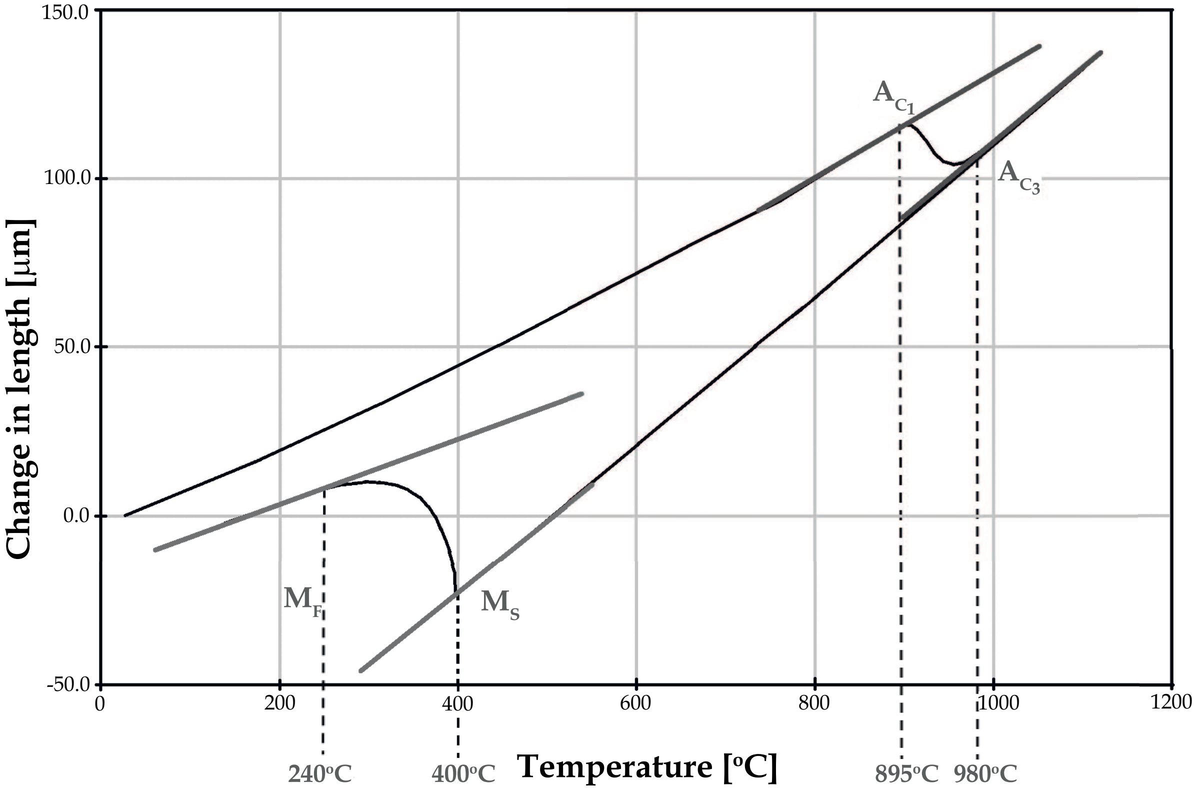

Figure 3.4: Dilation curve of the steel sample recorded by the dilatometer.

2013; Mayr et al., 2008)). The prior austenite grain boundaries are more difficult to observe compared to the base material shown in Figure 3.1 primarily due to the formation of virgin martensite (Mayr et al., 2008).

3.5 Analysis and Results

To determine values for the temperature dependent terms ($\mathcal{L}_i$ in Equation 3.4 and γ in Equation 3.13), temperature ranges that relate to before and after the transformation occurs must be defined so that the terms relating to the α phase (austenite in this case) are fit where only α is present and the same for terms relating to the β phase (martensite in this case). The temperature range considered for the region where only austenite is present was 450-900°C. For the region where martensite is the dominant phase present during cooling, the temperature range considered was 125-250°C.

Results from the single phase regions in the cooling curve can be seen in Figure 3.6. The higher temperature curve in the CCA plot representing γ_α is fitted to the data between 900°C and 450°C and was best captured by using a second-order polynomial while the lower temperature curve is fitted between 250°C and 125°C and was captured by using a straight line as suggested by (Gibbs and Mendez, 2008; Gibbs et al., 2010). The high temperature CCA fit was likely affected by radiation heat loss, which is proportional to T^4, instead of T as in the case of convection. This causes deviations from linearity in γ_α which was best captured with a second-order polynomial rather than a straight line. In the case of the dilatometry plot, both $\mathcal{L}_\alpha$ and $\mathcal{L}_\beta$ were best captured using linear functions of temperature. The values for the parameters used in the curve fittings are presented in Table 3.3.

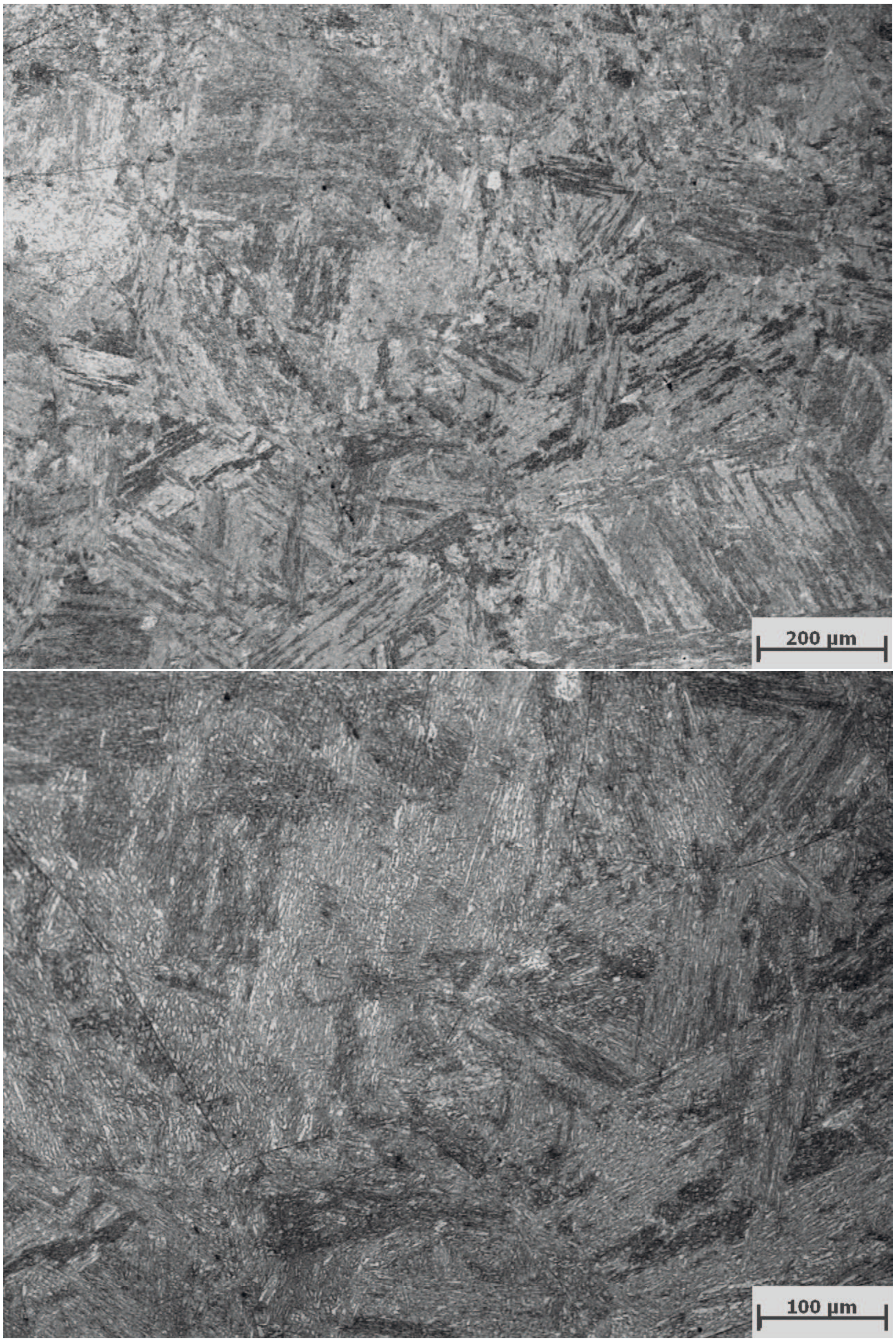

Figure 3.5: Optical micrographs of the 9Cr3W3CoVNb steel microstructure after dilatometery.

Table 3.2: List of terms and symbols used in the dilatometry and cooling curve analysis

Symbol	Name	Units
Common terms		
α	Name of the high temperature phase	
β	Name of the low temperature phase	
ρ_i	Specific density of phase i	$g/\mu m^3$
t	Time	s
T	Measured temperature of the sample	K
m	Total mass of the sample	g
m_i	Total mass of phase i	g
f_i	Mass fraction of phase i	g/g
n	Index number	
Dilatometry specific terms		
A	Cross-sectional area of the sample	μm^2
$\bar{h}$	Average heat-transfer coefficient over the sample	W/m^2K
K	Heat transfer coefficient of the sample	W/m^2K
L	Measured length of the sample	μm
L_i	Total length of phase i	μm
λ_i	Specific length of phase i	$\mu m/g$
$\mathcal{L}_\alpha$	Term defined in Equation 3.4	$\mu m/K$
$\mathcal{L}_\beta$	Term defined in Equation 3.4	$\mu m/K$
$C_{\Delta\lambda}$	Term defined in Equation 3.4	μm
CCA specific terms		
H	Extrinsic enthalpy of the system	J
H^*	Specific intrinsic enthalpy of the sample or phase	J/g
ΔH	Latent heat of transformation	J/g
c_p^i	Specific heat capacity of phase i	J/gK
λ_i	Specific length of phase i	$\mu m/g$
γ_α	Term defined in Equation 3.13	s
γ_β	Term defined in Equation 3.13	s
$C_{\Delta H}$	Term defined in Equation 3.13	Ks

Table 3.3: Values for the parameters used in curve fittings.

Parameter	Value	Units
γ_α	$-1.122 \times 10^{-8}T^2 + 2.256 \times 10^{-6}T - 1.706 \times 10^{-3}$	s
γ_β	$-1.581 \times 10^{-6}T - 1.395 \times 10^{-3}$	s
$C_{\Delta H}$	$4.641 \times 10^{+4}$	Ks
$\mathcal{L}_\alpha$	$1.08 \times 10^{-5}T + 2.136 \times 10^{-1}$	$\mu m/K$
$\mathcal{L}_\beta$	$-1.146 \times 10^{-4}T + 1.128 \times 10^{-1}$	$\mu m/K$
$C_{\Delta\lambda}$	$4.778 \times 10^{+1}$	μm

The evolution of the martensite fraction with time can be calculated using three separate methods: *a)* classic ”lever” method as per ASTM A1033-10; *b)* using the approach mentioned in Section 3.2.3 (dilation data); *c)* using the approach proposed in Section 3.3.3 (temperature data). Figure 3.7(a) compares the evolution of the martensite fraction with temperature obtained from both calorimetry and dilatometry methods. It can be seen that martensite formation starts around 430°C and ends close to 250°C. To see all the details of the martensite fraction evolution, the region between 200°C and 550°C in Figure 3.7(a) is enlarged and presented in Figure 3.7(b). This figure aslo includes the martensite fraction obtained from the experimental graph using ASTM A1033-10 standard method for graphical estimates of transformation progress (ASTM A1033-10, 2013). Figure 3.7(b) clearly shows that both calorimetry and dilatometry are powerful tools in predicting the evolution of martensite fraction with time. The temperature difference (ΔT_{max}) between the dialtometry and calorimetry curves observed in Figure 3.7(b) is explained in detail in the Appendix section.

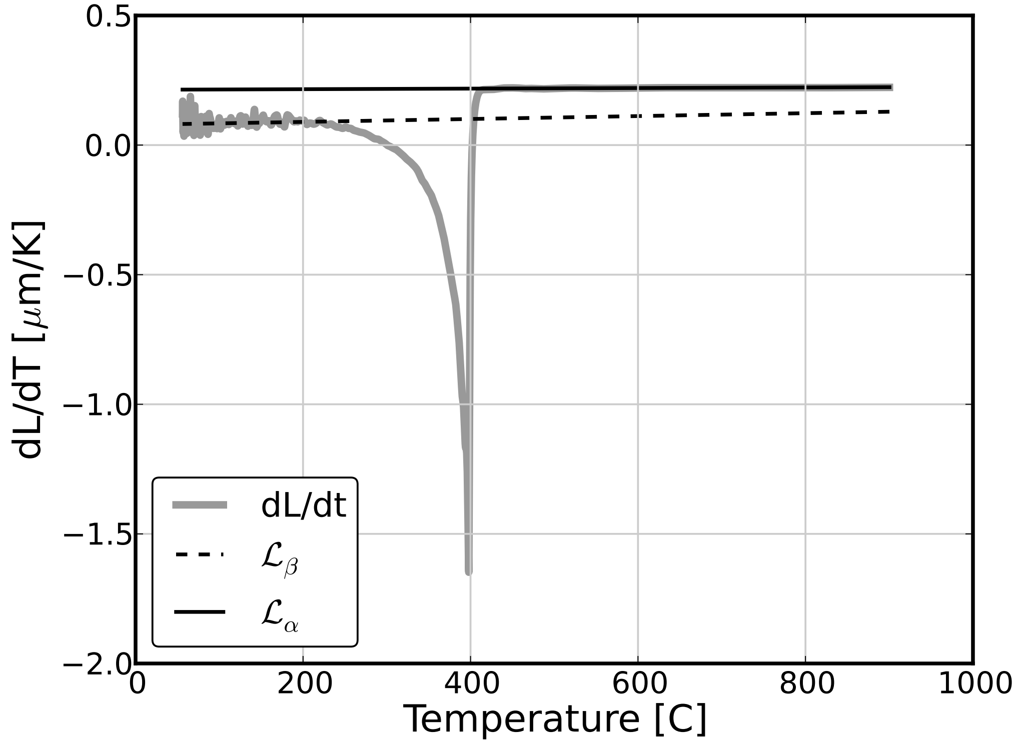

(a) Dilatometry

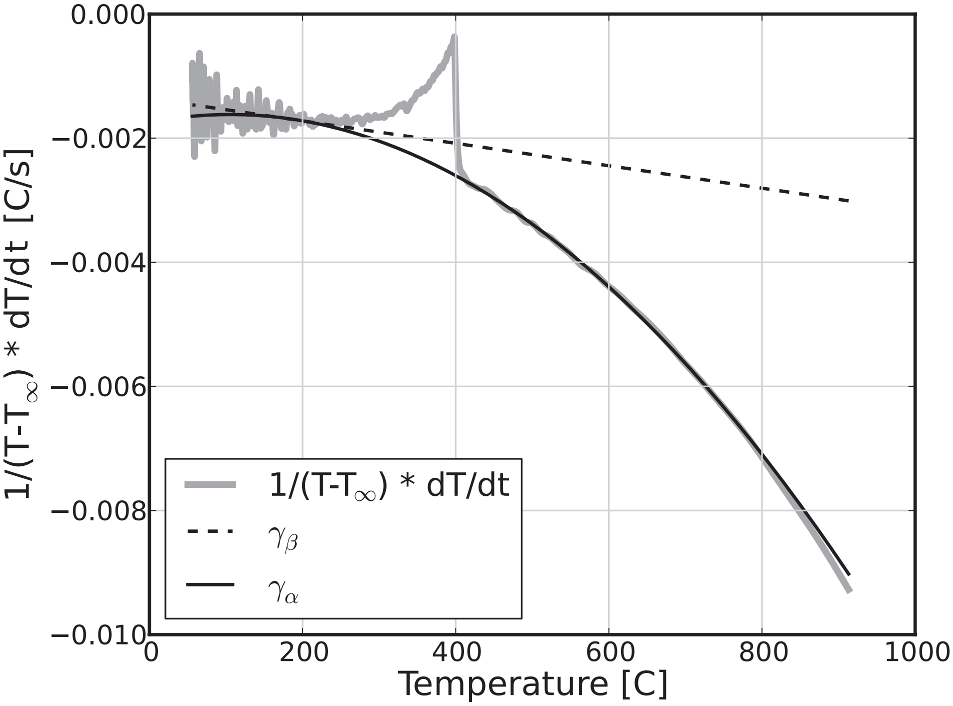

(b) CCA

Figure 3.6: Fitting of $\mathcal{L}$ and γ terms for dilatometry and CCA, respectively

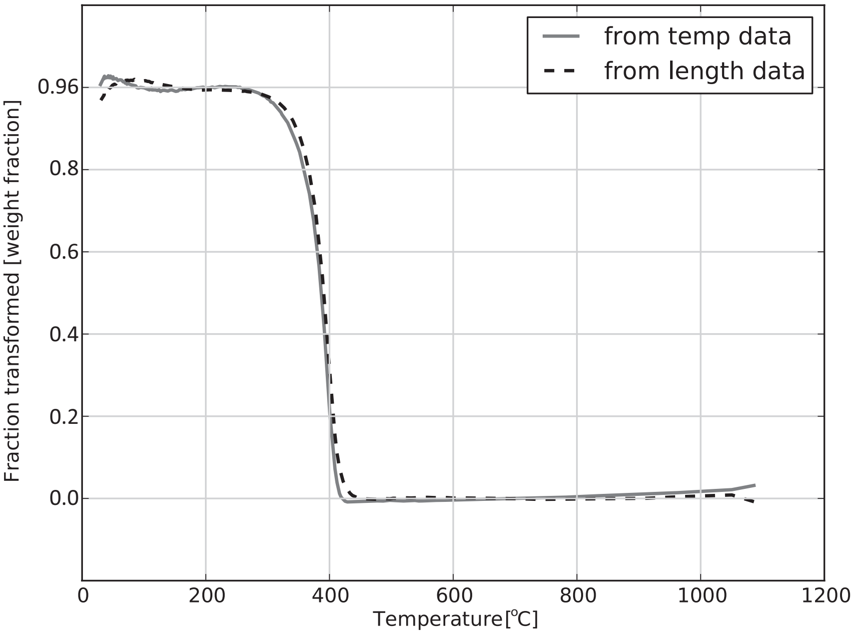

(a) Full temperature range

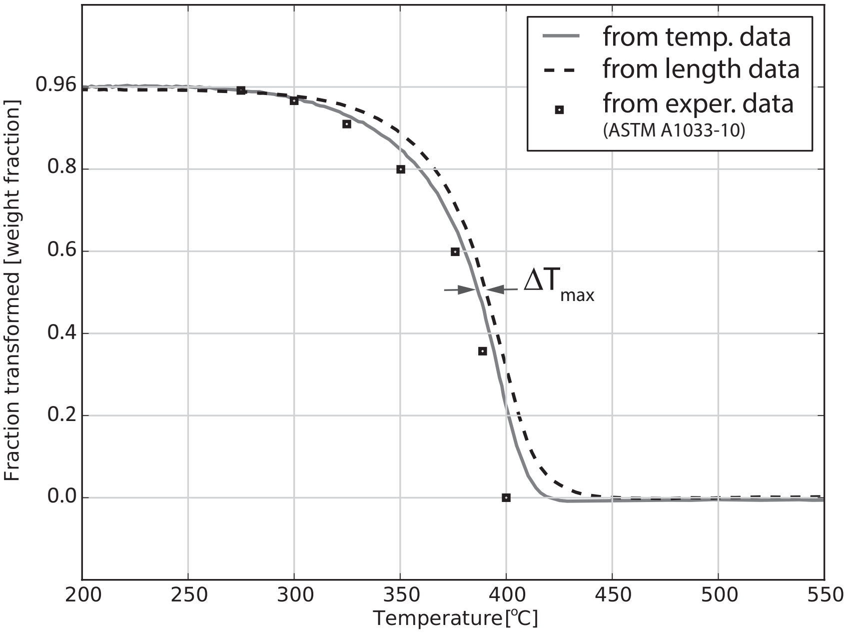

(b) Enlarged view of the transformation temperature range

Figure 3.7: A comparison of the two fraction transformed curves. ΔT_{max} is discussed in the appendix.

3.6 Discussion

In the analysis presented here, mass fractions are used because mass is a conserved quantity. With information about phase densities, a conversion to volume fraction is straightforward.

The high amplitude of noise observed at relatively low temperatures in Figure 3.6(b) is due to the nature of the equation used to represent the measured values ($\frac{1}{T-T_\infty} * \frac{dT}{dt}$). As the sample is cooled, the difference between the measured temperature of the sample and the ambient temperature approaches zero, hence, the fraction $\frac{1}{T-T_\infty}$ will approach infinity. Thus the measured cooling rate ($\frac{dT}{dt}$) will be greatly amplified as the temperature approaches the ambient temperature value, resulting in a noisier signal at lower temperatures.

There are many similarities between dilatometry and CCA but also some important difference that might make one method preferable over the other. Both techniques can be applied simultaneously to the same sample. All forms of dilatometry and CCA rely on some form of baseline. In the case of martensitic transformations, the baseline at low temperatures can contain a small error because the martensitic transformation is often not 100% finished at the lowest measured temperature. Both methods are also susceptible to inaccuracies due to temperature gradients within the sample which is discussed in detail in the Appendix (although these will be small due to the relatively small size of the sample).

The primary difference between the two methods is that the response variable is measured *directly* in the dilatometry analysis; compared to CCA, in which the response variable (heat flux away from the sample) is *inferred* based on temperature measurements and known heat transfer analysis methods. This has the potential to lead to inaccuracy if the heat transfer model does not accurately describe the experimental setup; however, the authors have found that it is relatively easy to create an experiment that can be well described by either a convective or radiative heat transfer law. This could make dilatometry more appealing if the transformation of interest occurs in a temperature range in which the dominant heat transfer mechanism changes; for example, from radiative at high temperatures to convective at lower temperatures.

The primary advantage of CCA is in the simplicity of its experimental setup and the freedom that this affords. One example of this flexibility is in the experiments presented here. These experiments were setup as standard dilatometry experiments without modifications for the CCA. With the analysis that was done here, relatively little new information was gained but by having two sources of information (length and heat) it would be possible to use the differences in these data to gain more information out of these experiments. For example, the length measurement is along one direction vs. heat that is omni-directional so some estimate of anisotropy could be made; or heat evolved is a combination of heat released by the transformation and heat absorbed by new interfaces being generated, so an estimate of the amount of interfacial energy in the sample could be made.

3.7 Conclusions

A sample of 9Cr3W3CoVNb steel was processed by normalizing at 1150°C for 1 hour, subsequently tempering at 770°C for 4 hours. This sample was exposed to a simulated weld thermal cycle by rapidly heating it to 1100°C and finally free cooling in a Bahr DIL-805/D dilatometer, resulting in a microstructure of nearly 100% martensite.

Cooling curve analysis has proven to be quite effective at producing similar results to dilatometry despite its drastically simpler experimental setup. Cooling curve analysis has also almost exactly reproduced the evolution of the martensitic transformation, as determined by dilatometry. The result of this experiment supports cooling curve analysis as a complement to dilatometry with the ability of tracking phase transformations even in the absence of dimensional changes. This, combined with the interesting possibilities that can come from combining CCA with other experimental techniques, makes CCA an analysis tool with vast potential for future utilization and development.

A rigorous methodology for the integration of dilatometry data is presented and compared with the traditional method obtaining similar results.

3.8 Acknowledgement

The authors would like to acknowledge the Natural Sciences and Engineering Research Council of Canada (NSERC), Codes And Standards Training Institute (CASTI) and MITACS for their support of this exploratory work.

3.9 Appendix: Estimation of temperature gradients in a dilatometry sample

Typically in dilatometry, the temperature is measured with a thermocouple welded to the surface of the metal sample. During free cooling of a metal dilatometry sample, a slight difference exists between the temperature of the core of the sample and its surface. A schematic of this temperature gradient is shown in Figure 3.8.

From an energy balance on the surface of the sample (heat transfer due to conduction = heat transfer due to convection) and assuming heat losses are only through the sides of the cylindrical sample, which is typically the case in push rod dilatometers, Equation 3.12

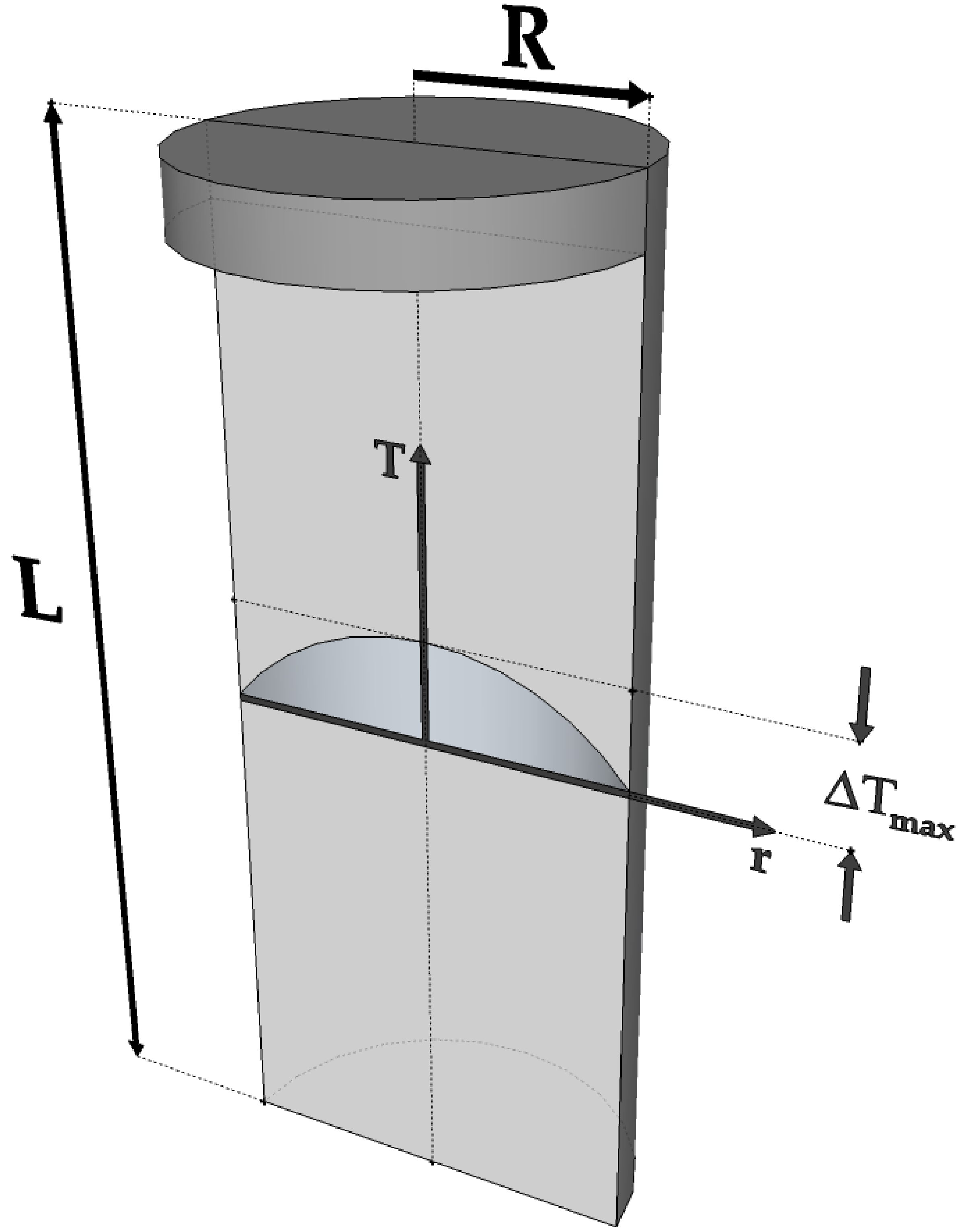

Figure 3.8: Variation of temperature in a typical cylindrical sample (L in length and R in radius) used in dilatometry.

can be rewritten as:

$$\frac{dT}{dt}\left[mc_p^{\alpha}\left(1-f_{\beta}\right)+mc_p^{\beta}f_{\beta}-m\Delta H^{*}\frac{\partial f_{\beta}}{\partial T}\right]=\bar{h}A\left(T-T_{\infty}\right)=-kA\left.\frac{\partial T}{\partial r}\right|_{R} \tag{3.18}$$

This equation can then be simplified to:

$$m\bar{c_p}\frac{dT}{dt}=-kA\left.\frac{\partial T}{\partial r}\right|_{R} \tag{3.19}$$

In this case $\bar{c_p}$ is the average heat content in the transformation range $\left(\bar{c_p}=\frac{H_2-H_1}{T_2-T_1}\right)$ and the corresponding thermal diffusivity is $\bar{\alpha}=\frac{k}{\rho\bar{c_p}}$. Temperature homogeneity is crucial to the analysis techniques presented here. The degree to which a sample is spatially isothermal is captured by the Biot number ($Bi=\frac{\bar{h}R}{k}$) (Bergman et al., 2011). For small Bi numbers $\left(\frac{\bar{h}R}{k}<<1\right)$, the temperature profile can be considered to be nearly homogeneous, decreasing uniformly at all points with time (Poirier and Geiger, 2013). A nearly uniform temperature distribution can be captured well with a second order polynomial. According to (Mendez, 2010), the gradient at the surface could then be estimated as:

$$-\left.\frac{\partial T}{\partial r}\right|_{R}\approx 2\frac{\Delta T_{max}}{R} \tag{3.20}$$

Considering a long cylinder:

$$m=\pi R^2L\rho, \qquad A=2\pi RL, \tag{3.21}$$

then,

$$\Delta T_{max}\approx\frac{1}{4}\frac{R^2}{\bar{\alpha}}\frac{dT}{dt} \tag{3.22}$$

For the setup used $k \approx 22.3\frac{W}{mK}$ (JAHM, 1999; Peet et al., 2011), $\rho \approx 7645\frac{kg}{m^3}$ (JAHM, 1999), $\bar{c_p} \approx 601\frac{J}{kgK}$ (Http://www.thermocalc.com, 2013; Gojić et al., 2004) (estimated as the addition of average c_p from start of transformation at 430°C to end of transformation at 250°C and the ratio of enthalpy of transformation and transformation temperature range, $\bar{c_p} = c_p + \frac{\Delta H}{\Delta T}$), $\bar{h} \approx 19.1\frac{W}{m^2K}$ (estimated from the high temperature single phase region with $c_p \approx 500\frac{J}{kgK}$(Http://www.thermocalc.com, 2013)), $R = 0.002m$, and $\bar{\alpha} = 5.83 \times 10^{-6}\frac{m^2}{s}$. Hence, $Bi = 0.0017$. With Bi significantly less than 1, the temperature profile is considered to be nearly homogeneous.

Using Equation 3.22, the estimate of the maximum temperature difference ranges from $\Delta T_{max} \approx 0.13$K at 300°C to $\Delta T_{max} \approx 0.84$K at 1000°C. The range obtained for ΔT_{max} is comparable to the difference in temperatures observed in Figure 3.7 (3.8°C).

3.10 References

Alexandrov, B.T., Lippold, J.C., 2007. Single Sensor Differential Thermal Analysis of Phase Transformations and Structural Changes During Welding and Postweld Heat Treatment. Welding in the World 51, 48–59.

ASTM A1033-10, 2013. Standard Practice for Quantitative Measurement and Reporting of Hypoeutectoid Carbon and Low-Alloy Steel Phase Transformations 1, pp. 1–14.

Bakhtiyarov, S.I., Dupac, M., Overfelt, R.a., Teodorescu, S.G., 2004. On Electrical Conductivity Measurements of Molten Metals by Inductive Technique. Journal of Fluids Engineering 126, 468–470.

Bergman, T.L., Incropera, F.P., Lavine, A.S., DeWitt, D.P., 2011. Fundamentals of Heat and Mass Transfer. Wiley.

Bojack, A., Zhao, L., Morris, P., Sietsma, J., 2012. In-situ determination of austenite and martensite formation in 13Cr6Ni2Mo supermartensitic stainless steel. Materials Characterization 71, 77–86.

Farahat, A.I.Z., 2008. Dilatometry determination of phase transformation temperatures during heating of Nb bearing low carbon steels. Journal of Materials Processing Technology 204, 365–369.

Frankel, J.I., Porter, W.D., Sabau, A., 2005. Analysis of Volumetric Changes Through Melting Using a Dilatometer. Journal of Thermal Analysis and Calorimetry 82, 171–177.

Gibbs, J.W., Kaufman, M.J., Hackenberg, R.E., Mendez, P.F., 2010. Cooling Curve Analysis to Determine Phase Fractions in Solid-State Precipitation Reactions. Metallurgical and Materials Transactions A 41, 2216–2223.

Gibbs, J.W., Mendez, P.F., 2008. Solid fraction measurement using equation-based cooling curve analysis. Scripta Materialia 58, 699–702.

Gojić, M., Sućeska, M., Rajić, M., 2004. Thermal analysis of low alloy Cr-Mo steel. Journal of Thermal Analysis and Calorimetry 75, 947–956.

Http://www.thermocalc.com, 2013. Thermo-Calc Software TCFE6 Steels/Fe-alloys database Version 6.2.

JAHM, 1999. Material Property Database (MPDB v6.61).

Kiani-Rashid, A., Edmonds, D., 2008. Phase transformation study of aluminium-containing ductile cast irons by dilatometry. Materials Science and Engineering: A 481-482, 752–756.

Kiuchi, M., Sugiyama, S., 1994. A New Method to Detect Solid Fractions of Mushy/Semi-Solid Metals and Alloys. Annals of the CIRP 43, 271–274.

MacKenzie, R.C., 1970. Differential Thermal Analysis. Academic Press.

Mayr, P., 2013. Henry Granjon Prize Competition 2008 Joint Winner Category B: Materials Behaviour and Weldability Evolution of Microstructure and Mechanical Properties of the Heat-Affected Zone in 9Cr Steels. Welding in the World 54, R1–R11.

Mayr, P., Palmer, T., Elmer, J., Specht, E., Allen, S., 2010. Formation of Delta Ferrite in 9 Wt Pct Cr Steel Investigated by In-Situ X-Ray Diffraction Using Synchrotron Radiation. Metallurgical and Materials Transactions A 41, 2462–2465.

Mayr, P., Palmer, T.A., Elmer, J.W., Specht, E.D., 2008. Direct observation of phase transformations in the simulated heat-affected zone of a 9Cr martensitic steel. International Journal of Materials Research 99, 381–386.

Mendez, P.F., 2010. Characteristic Values in the Scaling of Differential Equations in Engineering. Journal of Applied Mechanics 77, 610171–12.

Peet, M., Hasan, H., Bhadeshia, H., 2011. Prediction of thermal conductivity of steel. International Journal of Heat and Mass Transfer 54, 2602–2608.

Poirier, D.R., Geiger, G.H., 2013. Transport Phenomena in Materials Processing. Wiley.

Stefanescu, D.M., Upadhya, G., Bandyopadhyay, D., 1990. Heat Transfer-Solidification Kinetics Modeling of Solidification of Castings. Metallurgical Transactions A 21, 997–1005.

Tamminen, J., 1988. Thermal analysis for investigation of solidification mechanisms in metals and alloys. Phd. University of Stockholm.

Tszeng, T., Shi, G., 2004. A global optimization technique to identify overall transformation kinetics using dilatometry dataapplications to austenitization of steels. Materials Science and Engineering: A 380, 123–136.

Chapter 4

Quantification of evolution of multiple simultaneous phase transformations using dilation curve analysis (DCA)

4.1 Introduction

Dilatometry is a well-established technique primarily used to study the response of a material to temperature change (Speyer, 1993). A dilatometer records the length changes that occur during the heat treatment of a sample. The relative change in length as a function of temperature data obtained from a dilatometer can then be studied to determine if the sample experienced any phase transformation(s) during the heat treatment (Brown, 2001). The raw data can also be used to calculate the start and finish temperatures of the transformation(s). American Society for Testing and Materials (ASTM) has developed a well-known method (typically called the *lever-rule* method) for quantifying the fraction of a forming constituent from dilatation data (ASTM A1033-10, 2013). The ASTM method assumes the progression of the phase transformation is proportional to the dilatation progression between two baselines (Zhao et al., 2001). This method can only be applied to *single phase transformation*, or to multiple phase transformations if they can be considered to be in sequence with no overlaps. This is rarely the case in most materials, specifically steels continuously cooled after austenitizing (Kop et al., 2001). The shortcomings of the ASTM method are studied in (Knorovsky et al., 1998). This lack of quantification of the fractions of constituents is especially obvious in the continuous cooling transformation (CCT) and time-temperature-transformation (TTT) diagrams of (United States Steel Corporation, 1953) and (American Society for Metals, 1977).

Among previous work in the quantification of simultaneous phase transformations is the pioneering research of Onink et. al. on unalloyed steels (Onink et al., 1996). Their models are based on the lattice parameters of the constituting phases and their dependence on temperature and composition. Many researchers have built on the models presented in (Onink et al., 1996) and tried to expand them to take into account alloying elements (Choi, 2003; Gómez et al., 2003; Lee and Tyne, 2011), and diffusionless phase transformations (e.g. formation of martensite from austenite) (Lee et al., 2007; Kop et al., 2001; Suh et al., 2007; Warke et al., 2009). De Andres et. al. have developed a model on the basis of lattice parameters for the decomposition of pearlite to austenite in an eutectoid steel upon heating (de Andrés et al., 1998). Other researchers have taken a different approach and used the density of the constituting phases as the basis of their models (Zhao et al., 2001, 2002). Dykhuizen et. al. have developed a self-calibrating method with expressions for the phase densities as a function of temperature and composition to predict the austenite fraction in austenitization of a low carbon steel (Dykhuizen et al., 1999). Avrami-type transformation models are also used in some literature to quantify the transformation kinetics in low carbon steels (Leeuwen et al., 2001; Tszeng and Shi, 2004).

All of the models presented in the previous paragraph are finely tuned for specific alloy systems (mainly low alloy, low carbon steels) and are rarely applicable to the broader group of materials. In addition, most of the models suffer from limiting assumptions (e.g. geometrical assumptions, equilibrium estimations for non-equilibrium transformations, limited number of alloying elements, etc.) that hinder their application to all phase transformations.

Besides dilatometry, alternate techniques of measuring phase fractions also exist. Direct measurement techniques include microscopy (Barrena et al., 2013), differential scanning calorimetry (DSC) (Barrena et al., 2013; Kuntz et al., 2013; Xu et al., 2012; Birol, 2009), differential thermal analysis (DTA) (MacKenzie, 1970; Alexandrov and Lippold, 2007), synchrotron diffraction (Béchade et al., 2013). All of these techniques are either slow, expensive or difficult to access, and in some cases, unable to accommodate realistic sample sizes or cooling rates. Indirect measurement techniques include electrical resistivity (Mohanty and Bhagat, 2003; Bakhtiyarov et al., 2004; Kiuchi and Sugiyama, 1994). These techniques yield data in a format analogous to dilatometry, and it is likely the techniques presented here could also be extended to resistivity measurements. Research in the field of cooling curve analysis has led to the development of a promising methodology, independent of the type of material, to distinguish individual phase fractions in multiple simultaneous phase transformations (Kamyabi-Gol and Mendez, 2014; Gibbs et al., 2010; Gibbs and Mendez, 2008). Recently, a new approach to quantifying constituent fractions from dilation data for single phase transformations was developed by (Gibbs et al., 2014). This method is referred to as dilation curve analysis (DCA) and was compared to cooling curve analysis (CCA) results for an austenite to martensite single phase transformation in 9Cr3W3CoVNb steel. CCA has proven to be effective at producing similar results to dilatometry despite its drastically simpler experimental setup (Gibbs et al., 2014).

The aim of this paper is to present a novel mathematical formulation to be able to extract individual phase fractions of a multi-step phase transformation from the dilation curve. The multiple phase transformations can be simultaneous or consecutive. The highlight of this methodology is that it requires minimum input data from the user regarding the phase transformations. The presented methodology allows for its application to almost any material with very few assumptions and little user interaction.

4.2 Dilation curve analysis (DCA) during multiple transformations

The proposed DCA methodology consists of presenting all terms affecting the change in length with temperature in one single equation. The temperature dependent terms are then separated from the terms that depend on phase fraction. Raw dilatometry data and specific physical properties of some of the constituents (explained in more detail later on) are then used to determine values for the temperature dependent terms. Finally, the equations are solved independently to obtain all phase fractions as a function of temperature (i.e. phase fraction curves).

Without loss of generality, consider an isotropic n-constituent system with a sequence of phase transformations $1 \longrightarrow 2$, $1 \longrightarrow 3$, $\ldots$, $1 \longrightarrow n$ taking place at different time scales during cooling or heating with Constituent 1 being the only parent phase. The type and number of phase transformations do not affect the application of the proposed methodology i.e. the phase transformations can be sequential, simultaneous, or nested. The development of the methodology presented here will focus on nested phase transformations (one within the other) which are the most complicated to separate.

Consider a sample in which the microstructure is made of constituents 1, 2, ..., i, ..., n. For the case of nested transformations, $n = 1$ refers to the original parent constituent (typically austenite for the case of steels during cooling). Each constituent can be a phase (e.g. martensite) or a mixture of phases (e.g. bainite). The total volume of the sample is given by the volume of all constituents:

$$V_T = \sum_{i=1}^{n} V_i \tag{4.1}$$

where V_T is the total volume of the sample and V_i is the volume of constituent i. The constituent volumes (V_i) can be calculated from their mass fraction and density ($V_i = m_T f_i/\rho_i$), where f_i is the mass fraction of constituent i, $f_i = m_i/m_T$, ρ_i is the density of constituent i and m_T is the total mass of the sample. Applying these considerations to Equation 4.1 results in:

$$V_T = m_T \sum_{i=1}^{n} \frac{f_i}{\rho_i} \tag{4.2}$$

This equation accounts for multiple constituents present at any given temperature, with those that are not present having a mass fraction (f_i) of zero. For example, the experiments discussed later use the three constituent system of austenite, bainite, martensite ($n = 3$) where $i = 1$ is assigned to austenite, $i = 2$ is for bainite, and $i = 3$ is assigned to martensite.

The total mass of the sample in Equation 4.2 can be represented by the initial density and volume of the sample as $m_T = \rho_0 V_0$. The term f_i can be split up into a temperature dependent variable (f_i^*) and a constant (f_i^c). f_i^* ranges from 0, before the transformation, to 1, after the transformation is complete. f_i^c is defined only for the transformation product constituents and is the final mass fraction of constituent i after the transformation is complete. f_i^c can be confirmed through microscopy after the transformation is complete. Hence, $f_i \equiv f_i^c f_i^*$.

To quantify the progression of constituents as a function of temperature, it is useful to create a differential equation by differentiating Equation 4.2 with respect to temperature

Table 4.1: List of terms and symbols used.

Symbol	**Name**	**Units**
A	Sample cross-sectional area	μm^2
C_{λ_i}	Quantity defined in Equation 4.4	μm
f_i	Actual mass fraction of constituent i	g/g
f_i^c	Final mass fraction of constituent i	g/g
f_i^*	Normalized mass fraction of constituent i	g/g
j	Index number	-
L	Length of the sample	μm
L_0	Initial length of the sample	μm
m_i	Mass of constituent i	g
m_T	Total mass of the sample	g
n	Index number	-
$T_{S\,i}$	i^{th} constituent formation start temperature	s
$T_{F\,i}$	i^{th} constituent formation finish temperature	s
T	Measured temperature of the sample	K
V_0	Initial volume of the sample	μm^3
V_i	Volume of constituent i	μm^3
V_T	Total volume of the sample	μm^3
α_i	Linear thermal expansion coefficient of constituent i	1/K
β_i	Volumetric thermal expansion coefficient of constituent i	1/K
$\bar{\alpha_i}$	Average linear thermal expansion coefficient of constituent i	1/K
ϵ_T	Total strain due to change in temperature	μm/μm
γ_i	Quantity used in Equation 4.6	μm/K
λ_i	Quantity used in Equation 4.3	-
$\mathcal{L}_i$	Quantity related to specific length used in Equation 4.4	μm/K
ρ_0	Initial density of the sample	g/μm^3
ρ_i	Specific density of constituent i	g/μm^3

to obtain:

$$\frac{1}{V_0}\frac{dV}{dT} = \sum_{i=1}^{n}\left(f_i^c f_i^* \frac{\partial \lambda_i}{\partial T} + \lambda_i f_i^c \frac{\partial f_i^*}{\partial T}\right) \tag{4.3}$$

where $\lambda_i \equiv \rho_0/\rho_i$ and it can be shown that $\partial\lambda_i/\partial T = 3\lambda_i\alpha_i$ with α_i being the instantaneous linear thermal expansion coefficient of constituent i (i.e. $\alpha \equiv \frac{1}{L}\frac{dL}{dT}$, where L is a generic length for constituent i). The summation of all mass fractions adds to unity: $\sum\limits_{i=1}^{n} f_i = 1$. Constituent 1 is the only constituent in the parent microstructure so, $f_1^c = 1$. Also, for the type of nested transformations considered as an example here, $\sum\limits_{i=2}^{n} f_i^c = 1$.

In this case the summation starts at $i = 2$ since the parent constituent should not be included among the transformation products. Equation 4.3 can be rearranged considering the relationship between linear and volumetric thermal expansion coefficients (i.e. $\beta = 3\alpha$, where $\beta \equiv \frac{1}{V}\frac{dV}{dT}$) which will yield $\frac{1}{V_0}\frac{dV}{dT} = \frac{3V}{V_0 L}\frac{dL}{dT}$. For isotropic materials the ratio $V/V_0 = (L/L_0)^3$:

$$3\left(\frac{L}{L_0}\right)^2 \frac{1}{L_0}\frac{dL}{dT} = \sum_{i=1}^{n}\left(3f_i^c f_i^* \lambda_i \alpha_i + \lambda_i f_i^c \frac{\partial f_i^*}{\partial T}\right) \tag{4.4}$$

where L_0 is the initial length of the sample. For a typical material, the factor $(\mathrm{L}/\mathrm{L}_0)^2$ is very close to unity. The error caused by approximating $(\mathrm{L}/\mathrm{L}_0)^2$ as unity is discussed in the appendix. Equation 4.4 can then be rearranged as:

$$\frac{dL}{dT} = \mathcal{L}_1 + \sum_{i=2}^{n}(\mathcal{L}_i f_i^*) + C_{\lambda_i}\frac{\partial f_i^*}{\partial T} \tag{4.5}$$

where $\mathcal{L}_1 \equiv L_0\lambda_1\alpha_1$, $\mathcal{L}_i \equiv L_0 f_i^c(\lambda_i\alpha_i - \lambda_1\alpha_1) \quad \text{for } i \neq 1$, and $C_{\lambda_i} \equiv L_0 f_i^c(\lambda_i - \lambda_1)/3$. The definition of $\mathcal{L}_i$ at this stage is to gather all the terms related to constituent i in a single parameter that can be tracked when fitting to experimental data discussed later on.

For typical materials, $\lambda_i - \lambda_1$ is much smaller than either λ_1 or λ_i and C_{λ_i} is considered as independent of temperature. The conditions under which C_{λ_i} is constant are established in the appendix section. A similar relationship can be established between every $\mathcal{L}_i$ and α_i where $\mathcal{L}_i$ will be proportional to the difference between the linear thermal expansion coefficient of constituent i and Constituent 1.

The terms related to Constituent 2 (bainite in the experiments performed) can be isolated by rearranging Equation 4.5 as:

$$\frac{dL}{dT} = \gamma_2 + \mathcal{L}_2 f_2^* + C_{\lambda_2}\frac{\partial f_2^*}{\partial T} \tag{4.6}$$

where $\gamma_2 \equiv \mathcal{L}_1 + \sum\limits_{i=3}^{n}(\mathcal{L}_i f_i^* + C_{\lambda_i}\partial f_i^*/\partial T)$. The convenience of this rearrangement is that γ_2 does not depend on the evolution of Constituent 2. For isolating the terms related to constituent i, the equivalent of Equation 4.6 is $dL/dT = \gamma_i + \mathcal{L}_i f_i^* + C_{\lambda_i}\partial f_i^*/\partial T$ where $\gamma_i \equiv \mathcal{L}_1 + \sum\limits_{j=2, j\neq i}^{n}(\mathcal{L}_j f_j^* + C_{\lambda_j}\partial f_j^*/\partial T)$.

Every $\mathcal{L}_i$ and γ_i is calculated by fitting a baseline to a specific portion of the derivative of the dilation data obtained from a dilatometry experiment. $\mathcal{L}_1$ represents the sample material before any transformation has started (i.e. the portion of the dilatation curve above T_{S_2} in Figure 4.1(a)). Therefore, we can evaluate $\mathcal{L}_1$ by fitting a function (a linear fit is sufficient in most cases) to the portion of the derivative of the dilatation curve that only consists of Constituent 1 (austenite in the experiments performed). The condition under which $\mathcal{L}_i$ can be tracked using a linear fitting is discussed in the appendix section. This approach to evaluating $\mathcal{L}_1$ does not require explicit evaluation of the individual parameters that make up $\mathcal{L}_1$, i.e. L_0, ρ_0, ρ_1. When the only constituent present in the material is Constituent 1, all the other phase fractions will be zero ($f_2^*{=}\ldots{=}f_n^*{=}df_2^*{=}\ldots{=}df_n^*{=}0$ in Equation 4.6): $dL/dT = \mathcal{L}_1$.

A similar approach can be used to evaluate each $\mathcal{L}_i$ and γ_i from a specific portion of the derivative of the dilatation curve. Equation 4.7 demonstrates how each portion of the derivative of the dilatation curve in Figure 4.1 is used to evaluate $\mathcal{L}_i$ and γ_i.

$$\begin{cases} \mathcal{L}_1 \xrightarrow{\text{eval. from}} \text{when only Constituent 1 is present (above } T_{S2}) \\ \mathcal{L}_2 + \gamma_2 \xrightarrow{\text{eval. from}} \text{during the conditions after Constituent 2 finishes forming (below } T_{F2}) \\ \gamma_2 \xrightarrow{\text{eval. from}} \text{during the conditions before Constituent 2 has formed (above } T_{S2}) \\ \qquad \vdots \qquad \textit{repeat for every constituent} \\ \mathcal{L}_n + \gamma_n \xrightarrow{\text{eval. from}} \text{during the conditions after Constituent n finishes forming (below } T_{Fn}) \\ \gamma_n \xrightarrow{\text{eval. from}} \text{during the conditions before Constituent n has formed (above } T_{Sn}) \end{cases}$$

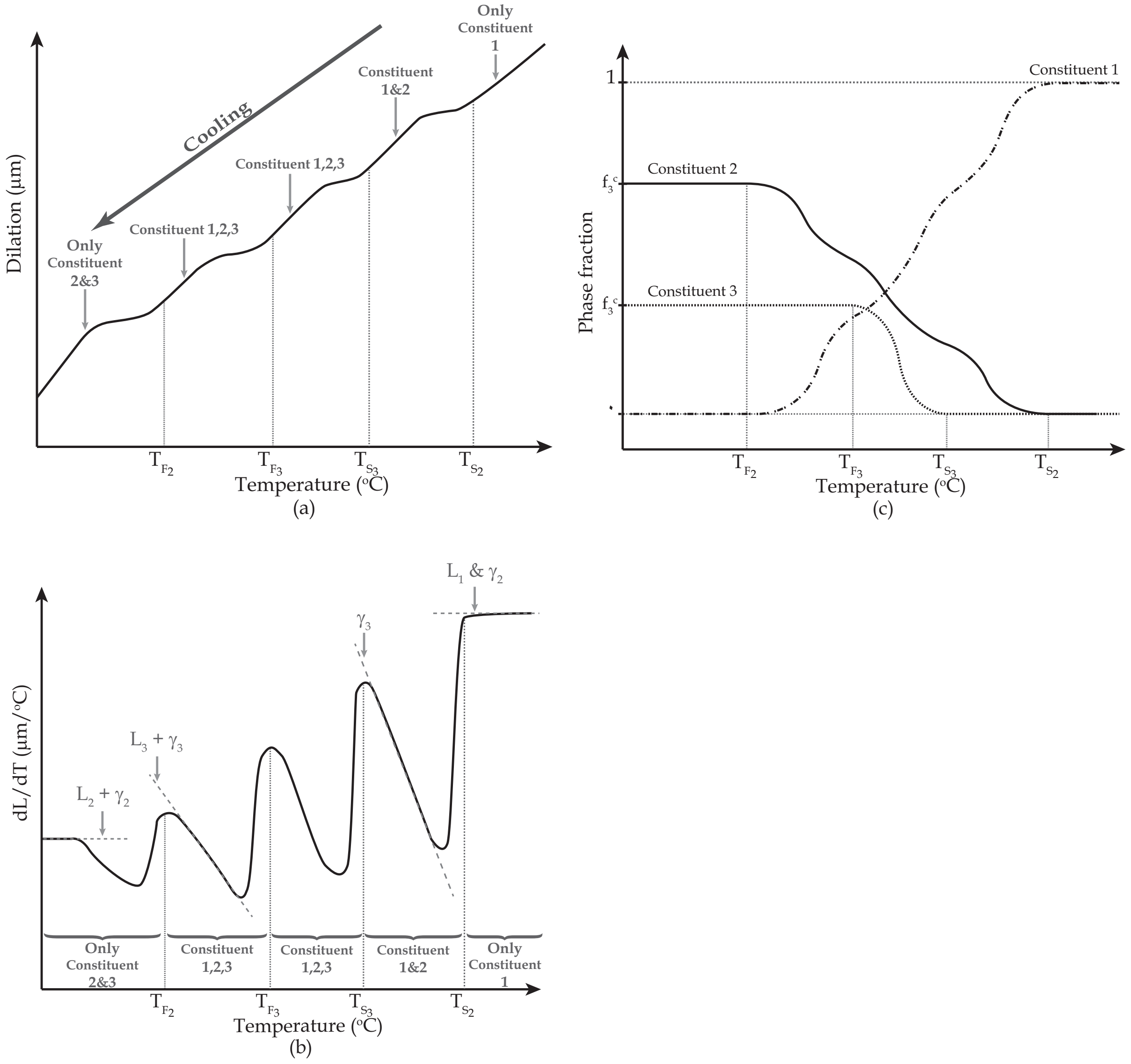

Figure 4.1: Schematic representation of a transformation containing 3 constituents and 2 nested phase transformations, (a) typical dilatation curve, (b) derivative of the dilation curve, (c) separated phase fractions obtained from the dilation curve. Note that these graphs are for a cooling experiment, i.e. temperature is decreasing with time.

(4.7)

The temperature dependence of $\mathcal{L}_i$ values depends on the linear thermal expansion of the associated constituents and is nearly constant in most materials. This temperature dependence can be captured as a gentle slope in a graph of dL/dT versus temperature. Figure 4.1(b) schematically shows how the values in Equation 4.7 are fitted to the derivative of the dilation curve.

C_{λ_i} is determined by iteration. The iterations are run until the value of $f_i^* = 1$ when constituent i has finished forming (i.e. below T_{Fi}). Typically 2 to 4 iterations are enough and for the case of austenite decomposition, a good starting value for the iterations is $C_{\lambda_i} = 10$ μm for a sample of 10 mm length.

$$\begin{cases} C_{\lambda_2} \xrightarrow{\text{eval. by}} \text{iterating after Constituent 2 finishes forming (below}T_{F2}\text{) to get } f_2^* = 1 \\ \qquad \vdots \qquad \textit{repeat for every constituent} \\ C_{\lambda_n} \xrightarrow{\text{eval. by}} \text{iterating after Constituent n finishes forming (below}T_{Fn}\text{) to get } f_n^* = 1 \end{cases} \tag{4.8}$$

After evaluating $\mathcal{L}_i$ and C_{λ_i}, an Euler explicit integration scheme is applied to Equation 4.6, and similar equations for all other constituents, to numerically calculate the fraction of each constituent starting from an initial condition of $f_i^* = 0$. The phase fraction for constituent i will be:

$$f_i^{*j+1} = f_i^{*j} + \frac{(T_{j+1} - T_j)}{C_{\lambda_i}} \Big[\frac{L_{j+1} - L_j}{T_{j+1} - T_j} - \gamma_i - \mathcal{L}_i f_i^{*j} \Big] \tag{4.9}$$

The characteristic mass fraction of constituent i can be calculated using the definition of C_{λ_i}:

$$f_i^c = \frac{3C_{\lambda_i}}{L_0(\lambda_i - \lambda_1)} \tag{4.10}$$

The initial length and initial density of the sample used for this analysis along with the density of Constituent 1 and $n-2$ other constituents are needed to calculate constituent fractions (e.g. in the case of the experiments performed here, only the density of austenite and martensite are required). The initial length of the sample is typically measured for every dilatometry experiment. The density of most constituents can be looked up from standard thermophysical tables, calculated through Thermo-Calc software (Andersson et al., 2002) or experimentally measured using the displacement method (Gupta, 2002). The final outcome of the proposed methodology is separated fraction curves for each of the constituents as shown in Figure 4.1(c).

4.3 Case study

The transformation of austenite to bainite and martensite upon cooling is used as an example to show the application of the proposed methodology. In this example the system consists of 3 constituents, austenite, bainite, martensite ($n = 3$) where $i = 1$ is assigned to austenite, $i = 2$ is for bainite, and $i = 3$ is assigned to martensite. Seven AISI 4140 steel samples with the composition shown in Table 4.2 were cooled at different rates to form various fractions of bainite and martensite. The cooling rates were chosen in a way that no pro-eutectoid ferrite would form upon cooling. The bainite and martensite fractions were calculated using the proposed methodology and compared to those obtained from metallography. Hot-stage microscopy was also performed on a high temperature confocal

Table 4.2: Chemical composition of the AISI 4140 steel used in weight percent. (Fe balance)

Element	C*	Mn	Cr	Mo	Ni	Cu	P	Al
Amount	0.41	0.73	0.82	0.17	0.06	0.13	0.011	0.022

* Nominal value of carbon in AISI 4140 steel

Table 4.3: Dimensions, weight and target cooling rate of dilatometry samples used.

Sample	Target cooling rate (K/s)	Length (mm)	Diameter±0.01 (mm)	Mass±0.01 (g)
1	1	8.26	4.95	1.27
2	1.5	8.07	4.95	1.24
3	2	7.73	4.95	1.19
4	2.5	7.77	4.95	1.19
5	3	8.08	4.95	1.24
6	3.5	7.58	4.95	1.16
7	4	9.54	4.95	1.46

scanning laser microscope (CSLM) to confirm the simultaneous formation of bainite and martensite from austenite. The composition of the AISI 4140 steel was measured with ICP-MS.

Cylindrical dilatometry samples were machined to size from a bar of AISI 4140 steel using a mini-lathe. The sample length, diameter, mass and target cooling rate are reported in Table 4.3. For the cooling rates chosen, the temperature control system in the dilatometer always kept a closed-feedback loop close to the target temperature.

K-type thermocouples (0.38 mm in diameter) were spot welded to the samples using a DCC Corp. Hotspot TC welder. For the dilatometry investigation, a vertical Linseis RITA L78 high speed quenching dilatometer was utilized. The dilatometry heating and cooling cycle is characterized by a heating rate of 10 K/s, a peak temperature of 1223 K (950°C), a holding time of 30 seconds, and different cooling rates as shown in Table 4.3 to room temperature. The change in the length of the samples with temperature is precisely recorded by the dilatometer. Upon cooling, austenite will first transform to bainite and

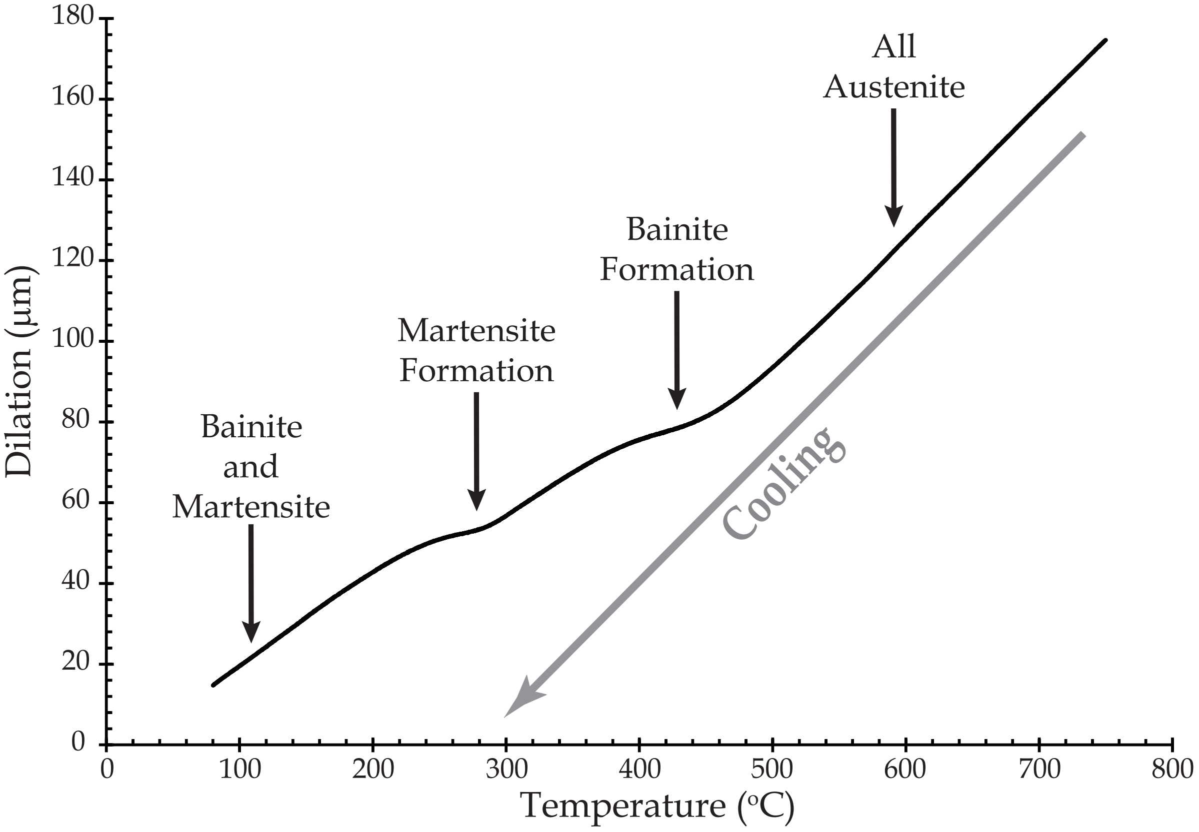

Figure 4.2: Experimentally determined change in length (relative to room temperature length) versus temperature for the AISI 4140 steel sample cooled at 2 K/s.

the remaining austenite will then transform to martensite while the bainite is evolving (Borgenstam et al., 2009; Kolmskog et al., 2012; Yakubtsov and Purdy, 2012); therefore, only the cooling portion of the experimental data is relevant to the current methodology. As an example, the resulting change in length with temperature upon cooling for sample 3 (cooled at 2 K/s) is shown in Figure 4.2.

Figure 4.3 displays a room temperature optical micrograph of the microstructure of the AISI 4140 steel sample cooled at 2 K/s at 1000 times magnification. The sample was polished and etched using 5% Nital solution to reveal the microconstituents. The microstructure consists of bainite and martensite with the white phase being martensite and the darker constituent showing bainite.

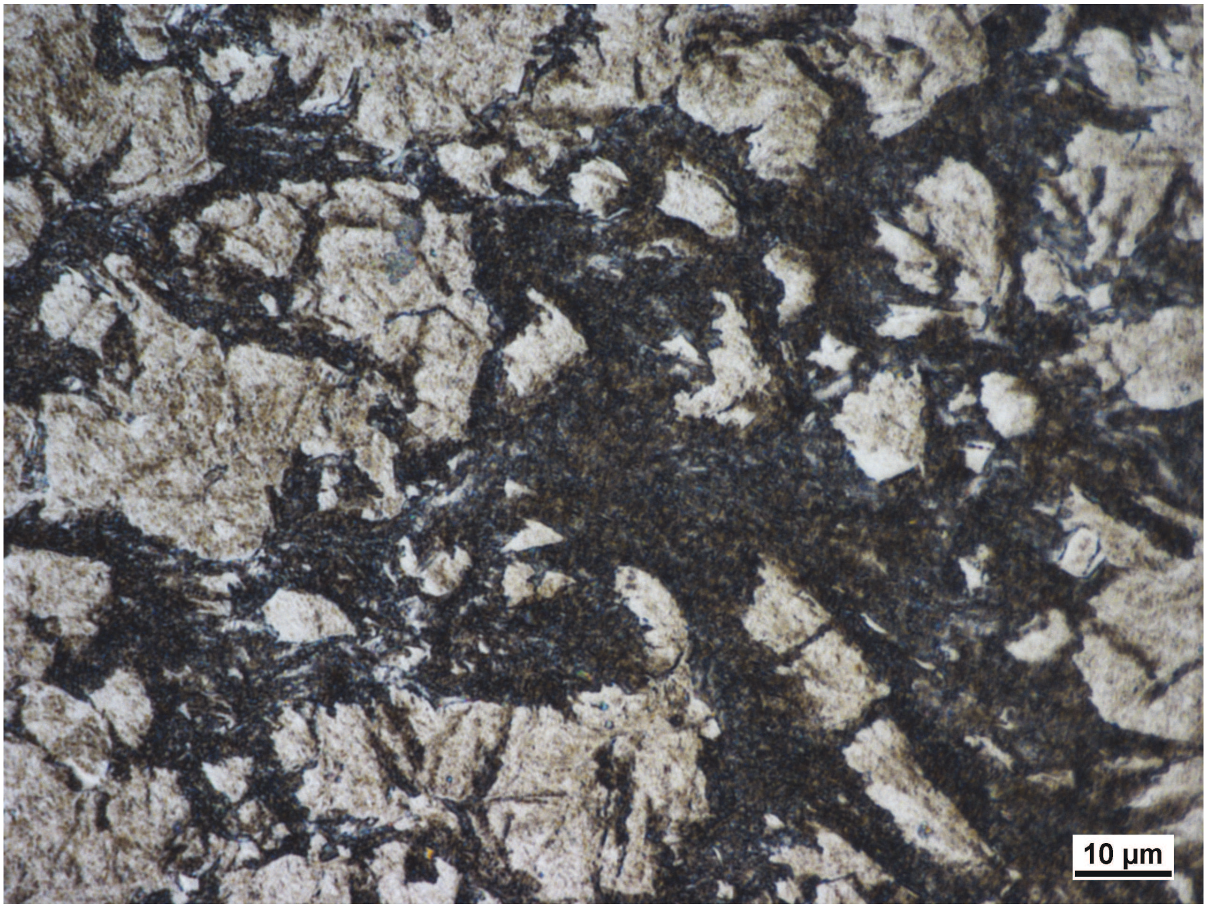

Figure 4.3: Optical micrograph of the room temperature AISI 4140 steel microstructure cooled at 2 K/s etched with 5% Nital (×1000 magnification).

Table 4.4: Values for the parameters used in curve fittings for sample 3 (cooled at 2 K/s).

Parameter	Value	Units
$\mathcal{L}_1 = \gamma_2$	$2.349 \times 10^{-4}T + 0.169$	μm/K
$\mathcal{L}_2 + \gamma_2 = \mathcal{L}_3 + \gamma_3$	$1.102 \times 10^{-4}T + 0.196$	μm/K
γ_3	$-1.153 \times 10^{-3}T + 0.598$	μm/K
C_{λ_2}	$2.554 \times 10^{+1}$	μm
C_{λ_3}	$1.137 \times 10^{+1}$	μm

4.3.1 Determination of bainite and martensite fractions

The $\mathcal{L}_i$ and γ_i for each of the samples are calculated by fitting a line to the appropriate section of the derivative of the dilation curve. As an example, the fitting of the values in Equation 4.7 to the experimental data in sample 3 (cooled at 2 K/s) is shown in Figure 4.4. Points A and B in Figure 4.4 were chosen in a way that the line passing through these two points is the best approximation for the entire region where only austenite exists. Similarly, the line passing through points C and D in Figure 4.4 is the best fit line to approximate the dependence of γ_3 with temperature. The dilation curve in the experimental case studied here (austenite to bainite and martensite transformation) shows fewer deflections as compared to the schematic in Figure 4.1. This is because bainite and martensite finish forming at the same time. Therefore, a single line passing through points E and F in Figure 4.4 can be used to simultaneously show the dependence of $\mathcal{L}_2 + \gamma_2$ and $\mathcal{L}_3 + \gamma_3$ on the temperature.

As an example, the values for the fitted parameters for sample 3 are shown in Table 4.4. The phase fraction evolution curves for bainite and martensite were then calculated for all seven samples using the presented methodology. For example, the fraction curves for sample 3 are shown in Figure 4.5 and Figure 4.6. The formation of bainite and martensite are clearly marked on Figure 4.5. The final phase fraction for this sample consists of 62% bainite and 38% martensite.

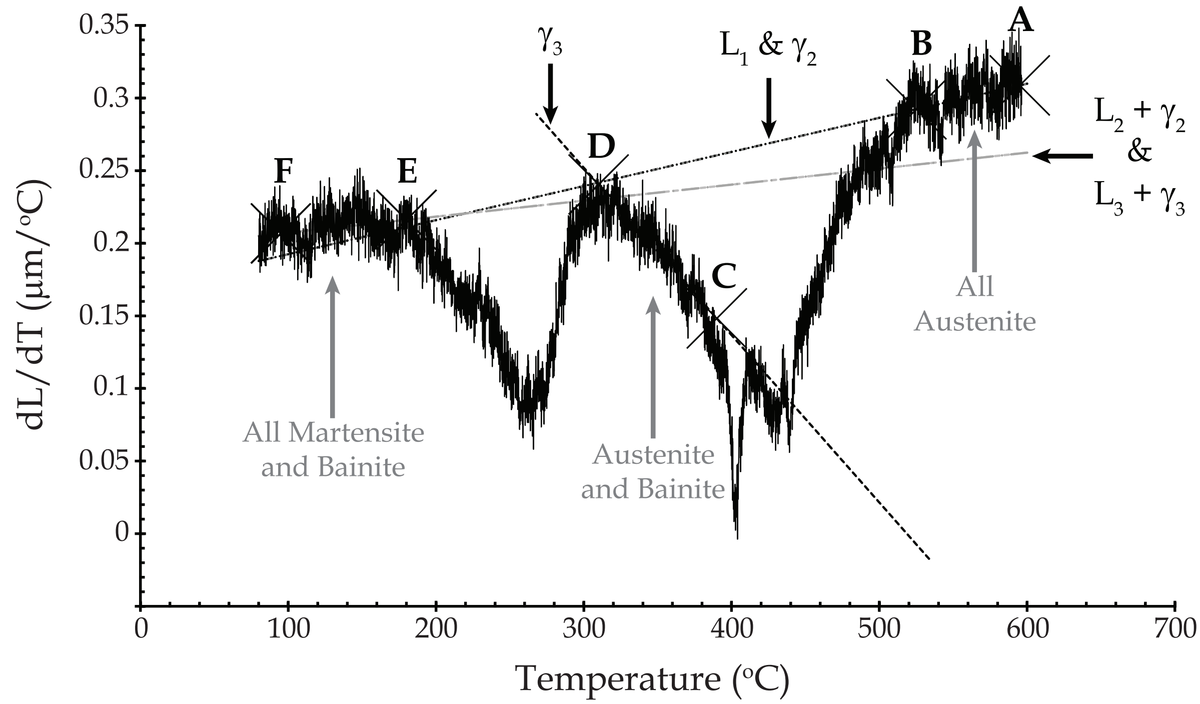

Figure 4.4: Fitting parameters in Equation 4.7 to experimental data (AISI 4140 steel cooled at 2 K/s) as linear functions of temperature.

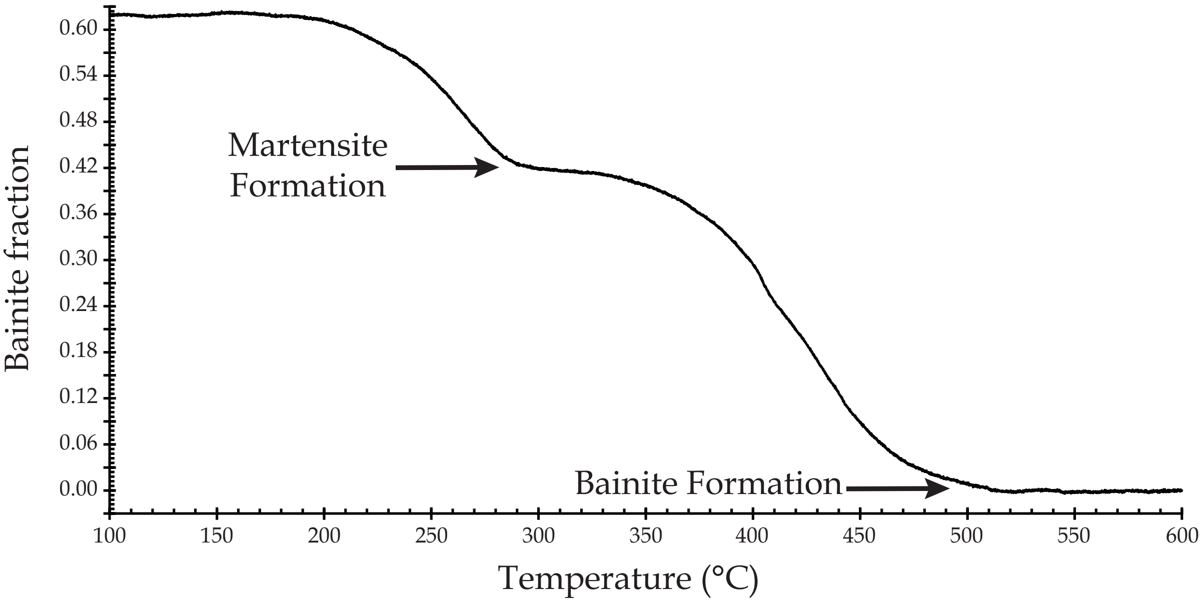

Figure 4.5: Bainite fraction versus temperature for AISI 4140 steel cooled at 2 K/s.

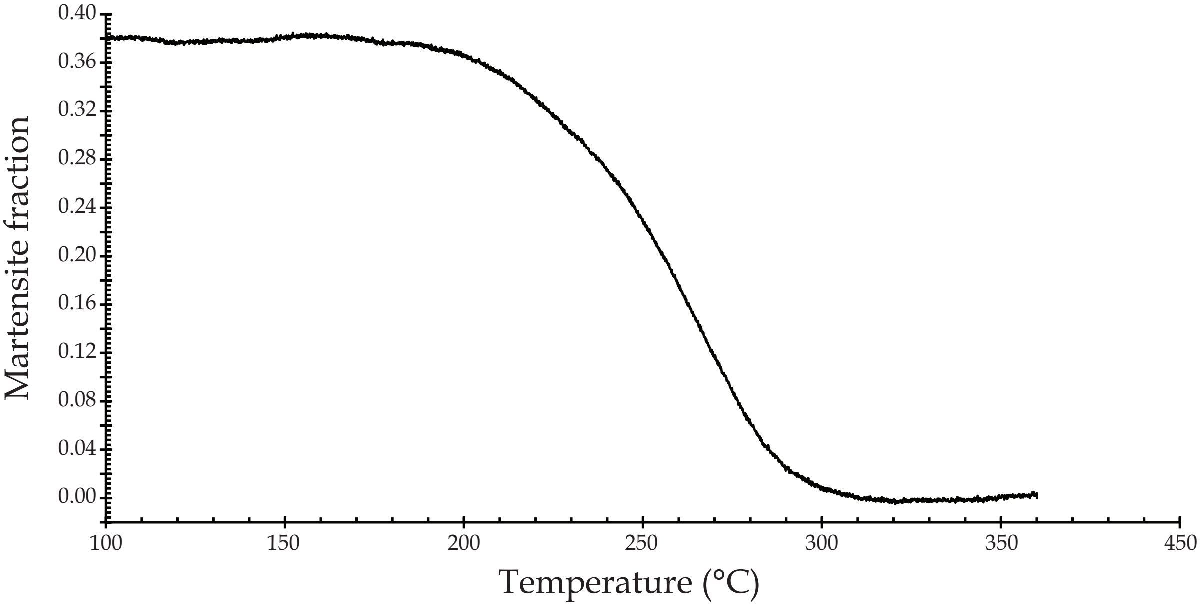

Figure 4.6: Martensite fraction versus temperature for AISI 4140 steel cooled at 2 K/s.

The bainite and martensite fractions obtained from the present methodology were verified by taking optical micrographs of the final microstructure of all seven samples. All seven samples were polished and etched with a 5% Nital solution for 8-10 seconds to reveal the microstructure. The fraction of bainite and martensite in each sample were calculated using area analysis by thresholding in ImageJ software (Schneider et al., 2012). Between four and eight optical micrographs at different magnifications (ranging from 5× to 1000× magnification) were analyzed using ImageJ to obtain the bainite and martensite fractions for each sample. It was presumed there is negligible amounts of retained austenite in the samples and hence, all the white constituent was associated to martensite and the darker constituent was assumed to be bainite. The average of phase fractions obtained from the analyzed micrographs per sample was used as the final fraction. 95% confidence interval of the analyzed micrographs is used as the error in the measurements. Table 4.5 summarizes the values of the bainite and martensite fractions obtained from both methods. The maximum difference between the fractions calculated using DCA and microscopy is 6.5%

Table 4.5: Bainite and martensite fractions calculated using the present methodology and optical microscopy.

Sample	Cooling rate (K/s)	Bainite frac. from DCA	Martensite frac. from DCA	Bainite frac. metallography	Martensite frac. metallography
1	1	0.95	0.05	0.89±0.07	0.11±0.07
2	1.5	0.87	0.13	0.83±0.09	0.17±0.09
3	2	0.62	0.38	0.61±0.04	0.39±0.04
4	2.5	0.29	0.71	0.32±0.08	0.68±0.08
5	3	0.09	0.91	0.07±0.06	0.93±0.06
6	3.5	0.05	0.95	0.04±0.03	0.96±0.03
7	4	0.002	0.998	0.009±0.003	0.991±0.003

in sample 1.

4.3.2 Hot-stage microscopy

Hot-stage microscopy was conducted on a sample of the same steel cooled at 2 K/s to confirm the simultaneous formation of bainite and martensite from austenite. The bainite and martensite start temperatures (B_s and M_s) were calculated from the hot-stage microscopy images by observing the first appearance of the new constituent. B_s and M_s values were compared to the values obtained from the current methodology for sample 3 considering the start as 1% of the total evolution of the transformation. Figure 4.7 is a cascade of screen-shots from the corresponding transformation video obtained from the CSLM (included as supplementary material). This figure shows the microstructure at B_s, M_s, and before and after bainite and martensite formation. The yellow and red arrows in these images respectively indicate the location of the forming bainite and martensite from austenite. The bainite and martensite start temperatures obtained from both methods for sample 3 are compared in Table 4.6. The difference in the martensite start temperature is much larger between the two methods than it is for the bainite start temperature. This is mainly due to the calibration of the measured temperature in the CSLM. The temperature measurements in the CSLM are not calibrated against reference

Table 4.6: comparison of the bainite and martensite start temperatures obtained from hot-stage microscopy and the current methodology for sample 3 (cooled at 2 K/s).

B_s current method (°C)	B_s hot-stage microscopy (°C)	M_s current method (°C)	M_s hot-stage microscopy (°C)
503.3	508.4	305.4	274.4

materials at low temperatures (below approximately 300 ^{o}C). Instead, an extrapolation from high temperature calibration values is used to correct the measured temperatures at lower temperature.

4.4 Discussion

When fitting a curve to the derivative of the dilation curve, the authors found that a linear function is best suitable to capture each portion of the curve for the case of the current experimental setup. Further details about the curve fitting technique used in this methodology can be found in (Gibbs et al., 2014). An exponential function can also be used to represent the different sections of the curves as suggested by Van Bohemen in (van Bohemen, 2013). This was carried out by the authors and was found that in the worst-case scenario the fitting results varied only 1.1% when an exponential function was used instead of a linear function. This shows that linear functions are much simpler and just as reliable as exponential functions to capture all the regions of the derivative of the dilatation curve for the current experimental setup.

Detecting the initiation of the transformations in hot-stage microscopy is fairly simple. In contrast, identifying the end of the transformations is not possible. In the case of austenite transformation to bainite and martensite, the simultaneous formation of bainite and martensite in the sample used could not be confirmed or denied with hot-stage

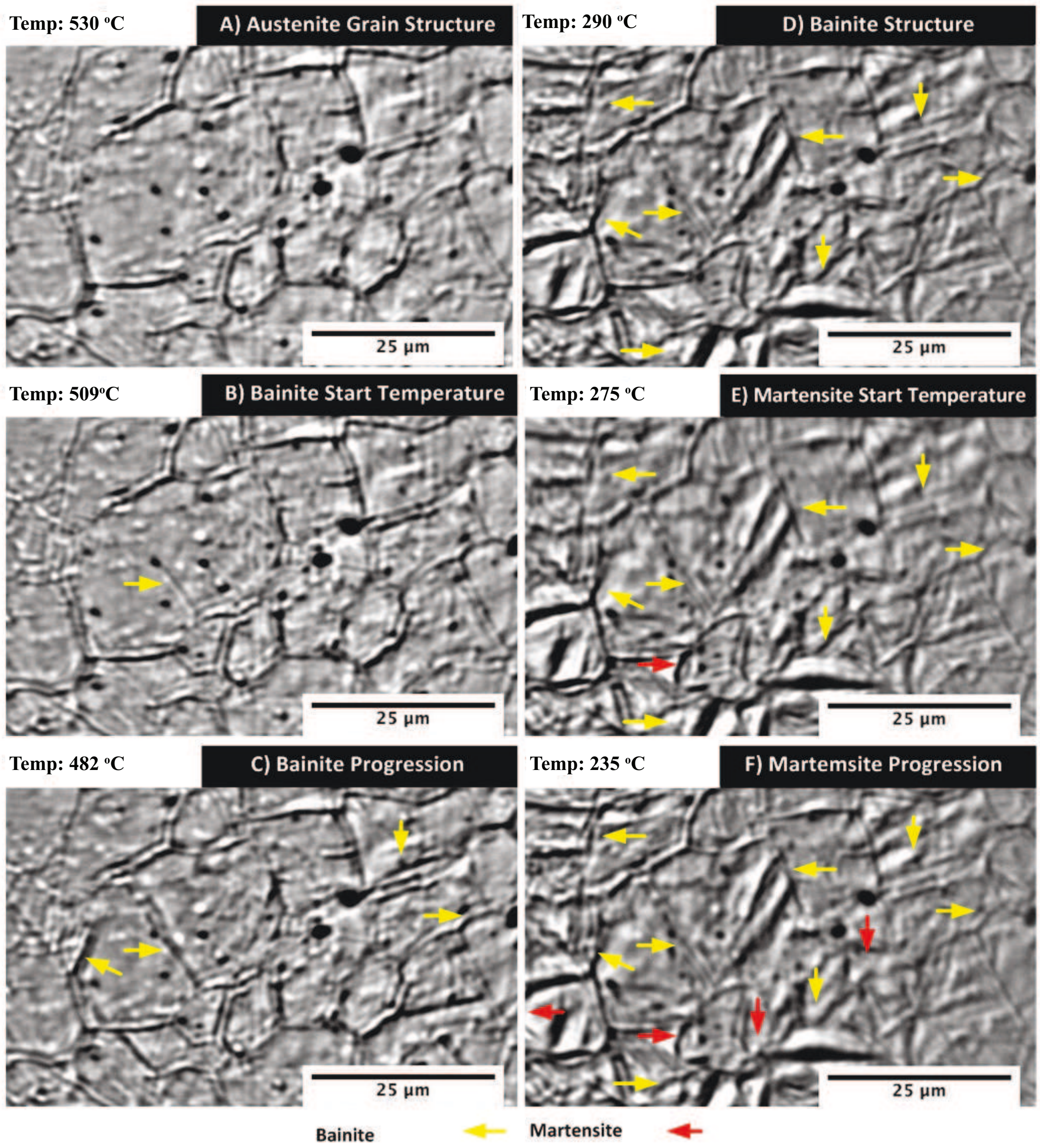

Figure 4.7: Cascade of hot-stage microscopy images before and after the bainite and martensite formation for sample 3 (cooled at 2 K/s). The yellow and red arrows in these images respectively indicate the location of the forming bainite and martensite from austenite. Full transformation video included as supplementary material.

microscopy; although, there is enough evidence in the literature that for medium carbon steels, bainite can evolve below the M_s temperature which has been confirmed with in situ simultaneous synchrotron X-ray diffraction and hot-stage microscopy (Borgenstam et al., 2009; Kolmskog et al., 2012; Yakubtsov and Purdy, 2012).

The presented methodology can be used to build advanced continuous cooling transformation (CCT) diagrams. In the current state, CCT diagrams only display the start and finish temperatures for each of the constituent regions they contain. In some cases, the 50% transformation curve is estimated in some of the regions of the CCT diagrams. The current methodology can improve these CCT diagrams by adding *"phase percent curves"* to the diagrams in addition to the start and finish temperatures. This additional information can add value to classic CCT diagrams by providing the user with the amount of each constituent at each cooling rate. This can help metallurgists in many ways such as designing more accurate heat treatments and producing better welding procedures.

The methodology described in this paper should be applicable to any material in which phase transformations are well detected in a dilatometer. The proposed approach involves a modest amount of effort (e.g. calculating/finding the density of some constituents) that is different from previous methodologies; however, this extra effort allows for the proper accounting of phase fractions that is not possible otherwise. In addition, the effort spent on analyzing a specific alloy group does not need to be repeated for similar systems. By measuring the final phase fraction in unknown systems or systems which do not have reliable thermodynamic databases available, the density of all constituents involved in the transformations can be accurately back-calculated. This is an advantage over relying solely on available thermodynamic databases and can be used to get a deeper understanding of new or custom alloy systems.

The developed methodology can be used with any dilatation data which is obtained from dilatometry runs without having to change the experimental setup or applying any limiting assumptions. This methodology could likely be extended to isothermal transformations by modifying the starting equations to base them on time instead of temperature.

4.5 Conclusions

A rigorous mathematical model for the quantification of phase fractions in simultaneous phase transformations using dilatation data is introduced. The methodology was applied to AISI 4140 steel, and can potentially be extended to many other types of material. The outcome of this methodology is an accurate accounting of phase fractions as the transformations progress in continuous cooling for multiple simultaneous phase transformations. Seven cylindrical AISI 4140 steel samples were austenitized and cooled to room temperature with constant cooling rates ranging from 1 to 4 K/s. The resulting microstructures consisted of different fractions of bainite and martensite. The martensite and bainite fractions calculated using the present method for all seven samples are in good agreement with that calculated through optical microscopy, with a maximum difference of 6.5% between the two methods. Hot-stage microscopy was performed on a high temperature confocal scanning laser microscope (CSLM). The bainite and martensite start temperatures (B_s and M_s) from the current methodology were in good agreement with the values obtained from the CSLM. The results of these examples support the presented methodology as a tool capable of tracking multiple simultaneous phase transformations and amount of each constituent present in the material.

The proposed methodology can be used to better quantify all phase transformations. Specifically in steels, this methodology can help improve the quality of CCT diagrams by adding valuable information to these diagrams that could not be included with previous methods of analysis.

4.6 Acknowledgement

The authors would like to acknowledge Codes And Standards Training Institute (CASTI), MITACS and Natural Sciences and Engineering Research Council of Canada (NSERC) for their support of this work. Special gratitude to the Canadian Welding Association (CWA) for their support of this research through the CWA Edmonton graduate annual award for excellence in welding engineering.

4.7 Appendix

4.7.1 Determination of the density of martensite

The density of martensite cannot be determined using conventional equations based on the lattice parameters of martensite such as those presented in (Durand-Charre, 2004); these theoretical equations for density of martensite only apply to iron-carbon binary alloys and do not take into account other alloying elements. The formulation for the lattice parameter of martensite given in (Yang and Bhadeshia, 2007) does not consider all the elements in the composition of the steel used in this experimental work. It assumes only iron atoms exist in the martensite unit cell, which is only an estimate for low alloy steels. In this work, the density of martensite in the AISI 4140 steel was experimentally measured using a sample of 100% martensite and the displacement method following the procedure stated in (Gupta, 2002). The measured density of martensite is reported in Table 5.2. For the experimental calculation of martensite, the density of water at 295.6 K is 0.99778 g/cm^3 (Gupta, 2002). The density of austenite (required to calculate f_3^c) was estimated from dilatometry of a sample that transformed to martensite, following the methodology presented in (Gibbs et al., 2014). The calculated values for the density of martensite and austenite used in this study are $\rho_{austenite} = 7.764 \times 10^{-12}$ g/μm^3 and $\rho_{martensite} = 7.782 \times 10^{-12}$ g/μm^3.

4.7.2 Approximations made in the proposed methodology

During the derivation of dL/dT in Equation 4.5 it was assumed that $(L/L_0)^2$ is very close to unity. This only holds for a material with $\bar{\alpha}(T - T_0) \ll 1$, where $\bar{\alpha}$ is the average linear thermal expansion coefficient between T_0 and T. This condition holds for most typical materials. For the case of austenite to bainite transformation in an 8.8 mm long sample the elongation is $\approx 30\mu$m, considering this factor as unity involves an error of $\approx 3 \times 10^{-3}$.

In calculating C_{λ_i} it was assumed that $\lambda_i - \lambda_1$ is constant. This is a reasonable assumption for typical materials. The temperature dependence of the density of an isotropic constituent at constant pressure can be expressed as $\rho_i = \frac{\rho_{0_i}}{1+3\bar{\alpha}_i(T-T_0)}$ (Gupta, 2002), where ρ_{0_i} is the density of constituent i at temperature T_0. $\lambda_i - \lambda_1$ can then be expressed as:

$$\lambda_i - \lambda_1 = \lambda_{i_0}\Big[1 + 3\bar{\alpha}_i(T - T_0)\Big] - \lambda_{1_0}\Big[1 + 3\bar{\alpha}_1(T - T_0)\Big] \tag{4.11}$$

where $\lambda_{i_0} \equiv \rho_0/\rho_{i_0}$ is the ratio between the overall density of the sample and the density of constituent i, both at room temperature. To further simplify Equation 4.11 it is convenient to define $\epsilon_{\lambda_i} \equiv \left(\frac{\lambda_{i_0}}{\lambda_{1_0}} - 1\right)$ and $\epsilon_{\bar{\alpha}_i} \equiv \left(\frac{\bar{\alpha}_i}{\bar{\alpha}_1} - 1\right)$. Equation 4.11 can then be rearranged as:

$$\lambda_i - \lambda_1 \approx \epsilon_{\lambda_i}\lambda_{1_0} + 3(\epsilon_{\lambda_i} + \epsilon_{\bar{\alpha}_i})\lambda_{1_0}\bar{\alpha}_1(T - T_0) \tag{4.12}$$

The assumption that C_{λ_i} is constant will only hold if the first term in Equation 4.12 is much greater than the second term:

$$\Big|\epsilon_{\lambda_i}\lambda_{1_0}\Big| \gg \Big|3(\epsilon_{\lambda_i} + \epsilon_{\bar{\alpha}_i})\lambda_{1_0}\bar{\alpha}_1(T - T_0)\Big| \tag{4.13}$$

After rearranging and simplifying Equation 4.13 and keeping in mind that $1 - 3\bar{\alpha}_1(T - T_0)$ is close to unity and can be approximated as 1, we will get:

$$\Big|3\bar{\alpha}_1(T - T_0)\Big| \ll \left|\frac{\epsilon_{\lambda_i}}{\epsilon_{\bar{\alpha}_i}}\right| \tag{4.14}$$

Equation 4.14 can be simplified to:

$$3\left[(\bar{\alpha}_i - \bar{\alpha}_1)(T - T_0)\right] \ll \left|\frac{\rho_{1_0}}{\rho_{i_0}} - 1\right| \tag{4.15}$$

Equation 4.15 shows that C_{λ_i} is approximately constant when the effect of difference in density between constituents is much greater than the effect of differential linear thermal expansion coefficients. For the case of austenite decomposition to bainite the right hand of Equation 4.15 is $\approx 1.4 \times 10^3$ times greater than the left hand; therefore, assuming a constant C_{λ_i} is reasonable.

In calculating $\mathcal{L}_i$, it was mentioned that a linear fitting to the derivative of the dilation curve is sufficient for capturing the variations with temperature. In other words, $\lambda_i\alpha_i$ is approximately proportional to the change in temperature. Using the temperature dependence of density introduced in the previous paragraphs, $\lambda_i\alpha_i$ can be rewritten as:

$$\lambda_i\alpha_i = \lambda_{i_0}\left[1 + 3\bar{\alpha}_i(T - T_0)\right]\alpha_i \tag{4.16}$$

If $3\bar{\alpha}_i(T - T_0) \ll 1$, then $\lambda_i\alpha_i$ will be proportional to α_i. For most materials α_i changes approximately linearly with temperature and so $\lambda_i\alpha_i$ can be tracked using a linear fitting to the derivative of the dilation curve. In the case of austenite decomposition to bainite $3\bar{\alpha}_i(T - T_0) \approx 3 \times 10^{-3}$ which is much less than unity and therefore, using a linear fitting to capture the changes with temperature is reasonable.

4.7.3 Step by step derivation of the methodology

Starting from Equation 4.2 the step by step derivation of the DCA methodology introduced in this paper is reported here.

$$V_T = m_T \sum_{i=1}^{n} \frac{f_i}{\rho_i} = V_0 m_0 \sum_{i=1}^{n} \frac{f_i}{\rho_i} \tag{4.17}$$

After rearranging Equation 4.17 we will have:

$$\frac{V_T}{V_0} = \sum_{i=1}^{n} f_i \frac{\rho_0}{\rho_i} \tag{4.18}$$

We define $\lambda_i \equiv \rho_o/\rho_i$. After differentiating Equation 4.18 with respect to temperature we will have:

$$\frac{1}{V_0}\frac{dV_T}{dT} = \sum_{i=1}^{n} f_i \frac{d\lambda_i}{dT} + \sum_{i=1}^{n} \lambda_i \frac{df_i}{dT} \tag{4.19}$$

We know the volume of the sample is proportional to the cube of the length of the sample ($V_T \propto L^3$). So we can calculate the derivative of the volume with respect to temperature as follows:

$$V_T = kL^3 \Rightarrow \frac{dV_T}{dT} = 3kL^2\frac{dL}{dT} = 3\frac{V_T}{L}\frac{dL}{dT} \Rightarrow \frac{1}{V_T}\frac{dV_T}{dT} = \frac{3}{L}\frac{dL}{dT} \tag{4.20}$$

By definition $\alpha \equiv \frac{1}{L}\frac{dL}{dT}$. Therefore, $d\lambda_i/dT$ can be rewritten as:

$$\frac{d\lambda_i}{dT} = \rho_0 \frac{d}{dT}\left(\frac{1}{\rho_i}\right) = \frac{\rho_0}{\rho_i}\rho_i \frac{d}{dT}\left(\frac{1}{\rho_i}\right) = \frac{\rho_0}{\rho_i}\frac{1}{V_i}\frac{dV_i}{dT} = \frac{\rho_0}{\rho_i}\frac{3}{L_i}\frac{dL_i}{dT} = 3\lambda_i\alpha_i \tag{4.21}$$

Substituting Equation 4.20 and Equation 4.21 into Equation 4.19 and taking $f_i \equiv f_i^c f_i^*$ will lead to:

$$\frac{V_T}{V_0}\frac{3}{L}\frac{dL}{dT} = \frac{L^3}{L_0^2}\frac{1}{L}\frac{dL}{dT} = 3\left(\frac{L}{L_0}\right)^2 \frac{1}{L_0}\frac{dL}{dT} = \sum_{i=1}^{n} 3 f_i^c f_i^* \lambda_i \alpha_i + \sum_{i=1}^{n} \lambda_i f_i^c \frac{df_i^*}{dT} \qquad (4.22)$$

From this point we can continue with the derivation following Equation 4.4.

4.8 References

Alexandrov, B.T., Lippold, J.C., 2007. Single Sensor Differential Thermal Analysis of Phase Transformations and Structural Changes During Welding and Postweld Heat Treatment. Welding in the World 51, 48–59.

Andersson, J.O., Helander, T., Hdghmd, L., Shi, P., Sundman, B., 2002. THERMO-CALC & DICTRA, Computational Tools For Materials Science. Calphad 26, 273–312.

de Andrés, C.G., Caballero, F., Capdevila, C., Bhadeshia, H.K.D.H., 1998. Modelling of kinetics and dilatometric behavior of non-isothermal pearlite-to-austenite transformation in an eutectoid steel. Scripta Materialia 39, 791–796.

ASTM A1033-10, 2013. Standard Practice for Quantitative Measurement and Reporting of Hypoeutectoid Carbon and Low-Alloy Steel Phase Transformations 1, pp. 1–14.

Bakhtiyarov, S.I., Dupac, M., Overfelt, R.a., Teodorescu, S.G., 2004. On Electrical Conductivity Measurements of Molten Metals by Inductive Technique. Journal of Fluids Engineering 126, 468–470.

Barrena, M.I., Gómez de Salazar, J.M., Pascual, L., Soria, A., 2013. Determination of the kinetic parameters in magnesium alloy using TEM and DSC techniques. Journal of Thermal Analysis and Calorimetry 113, 713–720.

Béchade, J.L., Menut, D., Doriot, S., Schlutig, S., Sitaud, B., 2013. X-ray diffraction analysis of secondary phases in zirconium alloys before and after neutron irradiation at the MARS synchrotron radiation beamline. Journal of Nuclear Materials 437, 365–372.

Birol, Y., 2009. Solid fraction analysis with DSC in semi-solid metal processing. Journal of Alloys and Compounds 486, 173–177.

van Bohemen, S., 2013. The nonlinear lattice expansion of iron alloys in the range 1001600K. Scripta Materialia 69, 315–318.

Borgenstam, A., Hillert, M., Å gren, J., 2009. Metallographic evidence of carbon diffusion in the growth of bainite. Acta Materialia 57, 3242–3252.

Brown, M., 2001. Introduction to thermal analysis: techniques and applications.

Choi, S., 2003. Model for estimation of transformation kinetics from the dilatation data during a cooling of hypoeutectoid steels. Materials Science and Engineering: A 363, 72–80.

Durand-Charre, M., 2004. Microstructure of Steels and Cast Irons.

Dykhuizen, R., Robino, C., Knorovsky, G., 1999. A Method for Extracting Phase Change Kinetics from Dilatation for Multistep Transformations : Austenitization of a Low Carbon Steel. Metallurgical and Materials Transactions B 30, 107–117.

Gibbs, J.W., Kaufman, M.J., Hackenberg, R.E., Mendez, P.F., 2010. Cooling Curve Analysis to Determine Phase Fractions in Solid-State Precipitation Reactions. Metallurgical and Materials Transactions A 41, 2216–2223.

Gibbs, J.W., Mendez, P.F., 2008. Solid fraction measurement using equation-based cooling curve analysis. Scripta Materialia 58, 699–702.

Gibbs, J.W., Schlacher, C., Kamyabi-Gol, A., Mayr, P., Mendez, P.F., 2014. Cooling Curve Analysis as an Alternative to Dilatometry in Continuous Cooling Transformations. Metallurgical and Materials Transactions A 46, 148–155.

Gómez, M., Medina, S.F., Caruana, G., 2003. Modelling of Phase Transformation Kinetics by Correction of Dilatometry Results for a Ferritic Nb-microalloyed Steel. ISIJ International 43, 1228–1237.

Gupta, S.V., 2002. Practical Density Measurement and Hydrometry. Series in Measurement Science and Technology, CRC Press.

Kamyabi-Gol, A., Mendez, P.F., 2014. The Evolution of the Fraction of Individual Phases During a Simultaneous Multiphase Transformation from TimeTemperature Data. Metallurgical and Materials Transactions A 46, 622–638.

Kiuchi, M., Sugiyama, S., 1994. A New Method to Detect Solid Fractions of Mushy/Semi-Solid Metals and Alloys. Annals of the CIRP 43, 271–274.

Knorovsky, G.a., Robino, C.V., Dykhuizen, R.C., MacCallum, D.O., 1998. Dilatometry in the Gleeble: What Did You Really Measure? ASM Proceedings of the International Conference: Trends in Welding Research 4, 101–106.

Kolmskog, P., Borgenstam, A., Hillert, M., Hedström, P., Babu, S.S., Terasaki, H., Komizo, Y.I., 2012. Direct observation that bainite can grow below MS. Metallurgical and Materials Transactions A: Physical Metallurgy and Materials Science 43, 4984–4988.

Kop, T., Sietsma, J., Zwaag, S.V.D., 2001. Dilatometric analysis of phase transformations in hypo-eutectoid steels. Journal of materials science 36, 519–526.

Kuntz, M.L., Panton, B., Wasiur-Rahman, S., Zhou, Y., Corbin, S.F., 2013. An Experimental Study of Transient Liquid Phase Bonding of the Ternary Ag-Au-Cu System Using Differential Scanning Calorimetry. Metallurgical and Materials Transactions A 44, 3708–3720.

Lee, S.J., Lusk, M., Lee, Y.K., 2007. Conversional model of transformation strain to phase fraction in low alloy steels. Acta Materialia 55, 875–882.

Lee, S.J., Tyne, C.J.V., 2011. Prediction of Martensite Volume Fraction in FeCrNi Alloys. ISIJ International 51, 169–171.

Leeuwen, Y.V., Onink, M., Sietsma, J., Zwaag, S.V.D., 2001. The .GAMMA.-.ALPHA.Transformation Kinetics of Low Carbon Steels under Ultra-fast Cooling Conditions. ISIJ International 41, 1037–1046.

MacKenzie, R.C., 1970. Differential Thermal Analysis. Academic Press.

American Society for Metals, ., 1977. Atlas of isothermal transformation and cooling transformation diagrams. American Society for Metals.

Mohanty, O.N., Bhagat, a.N., 2003. Electrical resistivity and phase transformation in steels. Materialwissenschaft und Werkstofftechnik 34, 96–101.

Onink, M., Tichelaar, F., Brakman, C., Mittemeijer, E., van der Zwaag, S., 1996. Quantitative analysis of the dilatation by decomposition of Fe-C austenites; Calculation of volume change upon transformation. Zeitschrift fur … 87, 24–32.

Schneider, C.A., Rasband, W.S., Eliceiri, K.W., 2012. NIH Image to ImageJ: 25 years of image analysis. Nature Methods 9, 671–675.

Speyer, R., 1993. Thermal analysis of materials.

Suh, D.W., Oh, C.S., Han, H.N., Kim, S.J., 2007. Dilatometric analysis of austenite decomposition considering the effect of non-isotropic volume change. Acta Materialia 55, 2659–2669.

Tszeng, T., Shi, G., 2004. A global optimization technique to identify overall transformation kinetics using dilatometry dataapplications to austenitization of steels. Materials Science and Engineering: A 380, 123–136.

United States Steel Corporation, ., 1953. Atlas of isothermal transformation diagrams. United States Steel.

Warke, V.S., Sisson, R.D., Makhlouf, M.M., 2009. A Model for Converting Dilatometric Strain Measurements to the Fraction of Phase Formed during the Transformation of Austenite to Martensite in Powder Metallurgy Steels. Metallurgical and Materials Transactions A 40, 569–572.

Xu, J.F., Liu, F., Zhang, D., Zhang, K., 2012. Comparison of baseline method and DSC measurement for determining phase fractions. Materials Science and Technology 28, 1420–1425.

Yakubtsov, I.a., Purdy, G.R., 2012. Analyses of transformation kinetics of carbide-free bainite above and below the athermal martensite-start temperature. Metallurgical and Materials Transactions A: Physical Metallurgy and Materials Science 43, 437–446.

Yang, H.S., Bhadeshia, H.K.D.H., 2007. Uncertainties in dilatometric determination of martensite start temperature. Materials Science and Technology 23, 556–560.

Zhao, J., Mesplont, C., Cooman, C., 2002. Calculation of the phase transformation kinetics from a dilatation curve. Journal of Materials Processing Technology 129, 345–348.

Zhao, J.Z., Mesplont, C., Cooman, B.C.D., 2001. Kinetics of Phase Transformations in Steels: A New Method for Analysing Dilatometric Results. ISIJ International 41, 492–497.

Chapter 5

Effect of austenite grain size on transformation kinetics and the CCT diagram of 4140 steel

5.1 Introduction

The austenite grain size has a direct effect on phase transformation during heat treatment and will indirectly influence the final mechanical and physical properties of the steel. Extensive studies have been conducted on the dependence of austenite grain growth on austenitizing temperature and time in low alloy steels (Giumelli et al., 1999; Jiao et al., 2000; Lee and Lee, 2008; Reti et al., 2001; Saito and Shiga, 1992; Militzer et al., 1996; Yoshie et al., 1992). Austenite grain growth can be very rapid when the steel contains low additions of alloying elements due to two factors: reduced solute dragging effect and limited precipitate formation (Suárez et al., 1992; Callister and Rethwisch, 2012). The size of the austenite grains will also affect the subsequent martensite start and finish temperatures. Several studies have looked into this effect (Brofman and Ansell, 1983; Huang and Xu, 2006; Lee and Lee, 2005; Yang and Bhadeshia, 2009). Multiple qualitative explanations of the effect of austenite grain size on martensite formation and start temperature exist in the literature. Some examples of these explanations can be found in (Brofman and Ansell, 1983; Bokrost and Parker, 1963; Sarma et al., 1979). More recently, Yang & Bhadeshia have developed a quantitative framework based on (Fisher et al., 1949) that is better suited to explain and predict the variations of martensite start temperature as a function of austenite grain size in low alloy steels (Yang and Bhadeshia, 2009).

The focus of the study presented here is to experimentally establish the effect of prior austenite grain size on subsequent phase transformation kinetics with specific emphasis on martensite formation. An empirical model for predicting the average austenite grain size as a function of austenitizing temperature and time is also developed. For the first time, cooling curve analysis (CCA) and dilation curve analysis (DCA) are used to compare the kinetics of martensite formation as a function of austenite grain size. Several continuous cooling transformation (CCT) diagrams are constructed for different prior austenite grain sizes. These diagrams are presented and compared to show the effect of prior austenite grain size on CCT diagrams.

5.2 Experimental procedure

Twelve cylindrical dilatometry samples of AISI 4140 were prepared using a mini-lathe. The composition of the AISI 4140 steel was determined using ICP-MS and is given in Table 5.1. The samples were all 5.0±0.1 mm in diameter and 10.0±0.1 mm in length. K-type thermocouples (0.38 mm in diameter) were spot welded to each sample using a DCC Corp. Hotspot TC welder. The twelve samples were subjected to the heat treatments shown in Table 5.2. To ensure all the samples started off with the same parent phase, each sample was heated to 1173 K, held for five minutes, and cooled at 400 K/s before being subjected to the appropriate heat treatment in Table 5.2. This way, the austenite grain size was varied depending *only* on the austenitizing temperature and time. It is

Table 5.1: Chemical composition of the AISI 4140 steel used (wt.%, Fe balance).

Element	C*	Mn	Cr	Mo	Ni	Cu	P	Al
Amount	0.41	0.73	0.82	0.17	0.06	0.13	0.011	0.022

* Nominal value of carbon in AISI 4140 steel

Table 5.2: Times and temperatures for heat treatments.

Sample	Heating rate (K/s)	Holding temperature (K)	Holding time (s)	Cooling rate (K/s)
1	10	1173	30	400
2	10	1173	60	400
3	10	1173	300	400
4	10	1173	600	400
5	10	1223	30	400
6	10	1223	60	400
7	10	1223	300	400
8	10	1223	600	400
9	10	1273	30	400
10	10	1273	60	400
11	10	1273	300	400
12	10	1273	600	400

assumed all the carbides in the steel samples have dissolved in austenite when the dilation curve reached a plateau during the austenitization holding time.

The samples were then mounted, polished, etched with 5% Nital solution and micrographs of the microstructure were obtained for each sample. All the microstructures consisted of martensite laths. Hardness testing was also performed using a Tukon 2500 Automated Vickers Hardness Tester to obtain the Vickers hardness of the samples to ensure the final microstructure was martensite in all the samples. Table 5.4 shows the average Vickers hardness values for each of the 12 samples. This was obtained by indenting each sample 12 times (in a 3 by 4 matrix) using a force of 1 kilogram and a 15 second hold time for each indent. The average of the 12 hardness measurements and the standard deviation are used to represent the hardness value and confidence interval for each of the samples, respectively. After hardness testing, the samples were re-polished and etched

Table 5.3: Etchants and etching procedures used.

Etchant	Components	Preparation procedure	Etching procedure	Function
5% Nital solution	19 mL ethanol 1 mL nitric acid	Add 1 mL of nitric acid to 19 mL of ethanol in a shallow beaker	Etch by immersion for approximately 10 seconds	Reveal martensite
Aqueous picric acid solution	100 mL distilled water 2 g picric acid 1 g sodium dodecylbenzene sulfonate 6 drops of HCl	Dissolve 2 g of picric acid in 100 mL of distilled water, add to this solution 1 g of sodium dodecylbenzene sulfonate. To enhance the etching effectiveness, add 6 drops of HCl	Heat the solution to 112 K and swab etch for 5 minutes. Lightly re-polish the sample such that only prior austenite grain boundaries are visible	Reveal prior austenite grains

using a saturated aqueous picric acid solution to reveal the prior austenite grains. Optical micrographs of the prior austenite grains were taken at different magnifications using a Nikon Eclipse MA200 Inverted Microscope, and the size of these grains was measured according to the Abrams three-circle technique described in (ASTM E112-13, 2013). All etchants used in this study, their functionality, relevant preparation and etching procedures are given in Table 5.3.

Three samples with different prior austenite grain sizes were heat treated with different cooling rates such that information to build CCT diagrams could be collected. The three samples chosen to build CCT diagrams were heat treated in the dilatometer to reproduce the initial austenite grain size of Samples 5, 9 and 12 in Table 5.2 (average austenite grain diameter of 15.64, 30.09 and 44.04 μm, respectively). The CCT curves were compared to each other to establish the effect of prior austenite grain size.

5.3 Measurement of austenite grain size

Two different etchants and techniques were used to reveal the prior austenite grains and martensite features. Figure 5.1 shows the microstructure of Sample 1 after etching with

5% Nital (Figure 5.1(a)) and picric acid (Figure 5.1(b)) to reveal the martensite and austenite grains respectively. The microstructure of Sample 12 after etching with 5% Nital and picric acid is illustrated in Figure 5.2. It is clear that Sample 12 (highest austenitization temperature and holding time) consists of larger austenite grains than Sample 1 (lowest austenitization temperature and holding time).

To obtain the average prior austenite grain diameter as shown in Table 5.4, the Abrams three-circle technique was employed following the procedure described in (ASTM E112-13, 2013). All micrographs used to calculate the austenite grain size were taken at 500X magnification to allow for convenient counting of the grain boundary intersections. The second and third columns of Table 5.4 show the number of micrographs that were necessary to obtain an acceptable level of accuracy (ASTM E112-13, 2013), and the total number of grain boundary intersections that were counted as a result, respectively. The 95% confidence interval as instructed in (ASTM E112-13, 2013) was used to show the accuracy of the austenite grain size measurements.

5.4 Empirical model of austenite grain size

An empirical model of austenite grain size was fitted on the theoretical basis of (Lee and Lee, 2008). This model involves an Arrhenius component and was fitted for 10 K/s heating rate and pure martensite initial microstructure. This model can be used to predict the austenite grain size for future austenitizing conditions using the same heating rate and initial microstructure. The expression of the proposed model is:

$$d = A \exp\left(-\frac{Q}{RT}\right) t^{n} \tag{5.1}$$

(a) Martensite revealed after etching with 5% Nital.

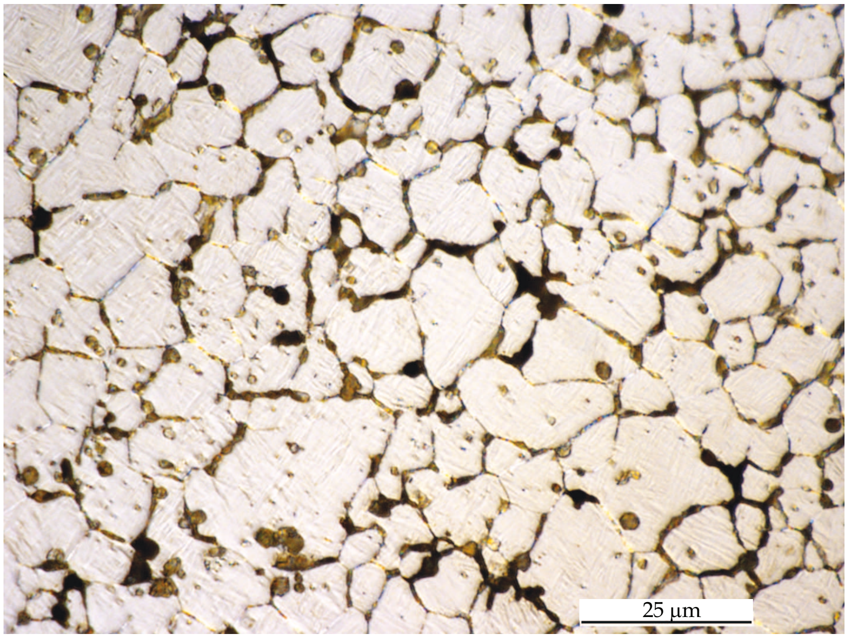

(b) Prior austenite grains revealed after etching with picric acid.

Figure 5.1: Optical micrographs of Sample 1 after etching with 5% Nital and picric acid.

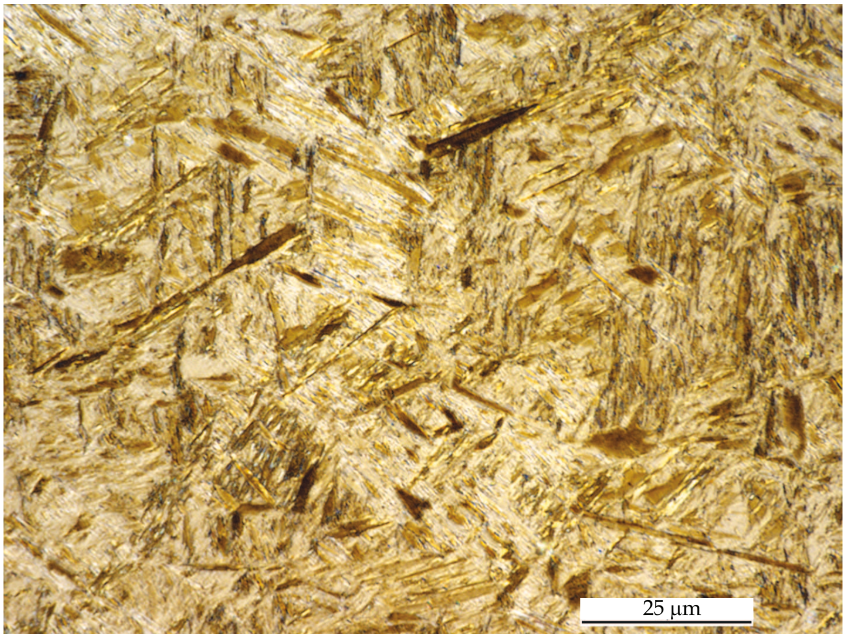

(a) Martensite revealed after etching with 5% Nital.

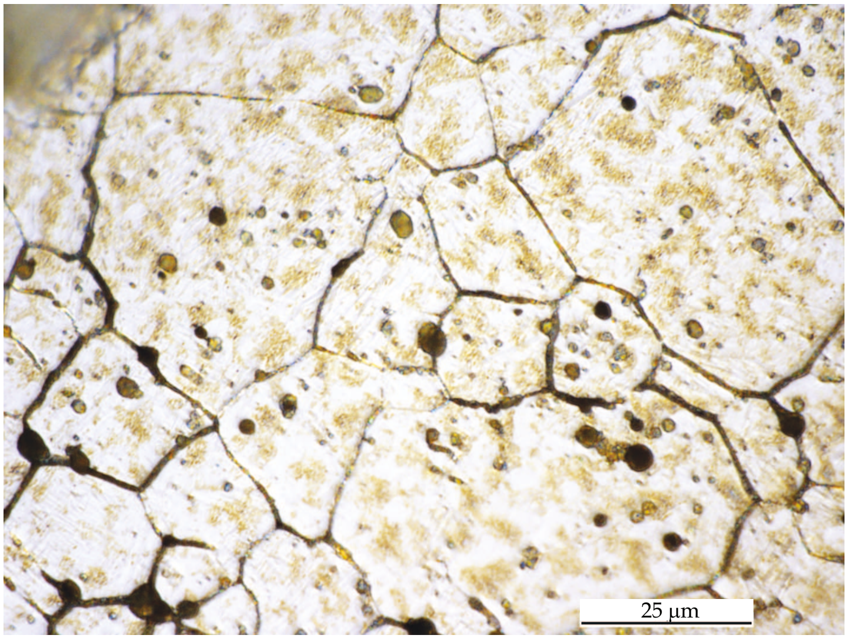

(b) Prior austenite grains revealed after etching with picric acid.

Figure 5.2: Optical micrographs of Sample 12 after etching with 5% Nital and picric acid.

Table 5.4: Average austenite grain size using Abrams three-circle technique as per (ASTM E112-13, 2013).

Sample	Total fields observed, n	Total counts (grain boundary intersections)	Average of the mean lineal intercept, $\bar{l}$ (mm^{-1})	ASTM grain size, G	Average grain diameter, d (μm) ± 95% CI	†Average HV $\pm\sigma$
1	7	497.5	0.01467	8.893	16.42 ± 1.68	692 ± 37.0
2	8	508.0	0.01653	8.549	18.51 ± 2.18	748 ± 56.8
3	10	523.5	0.02005	7.991	22.46 ± 1.78	719 ± 106.5
4	11	509.5	0.02303	7.593	25.79 ± 3.03	652 ± 27.6
5	7	522.0	0.01397	9.034	15.64 ± 0.90	701 ± 50.8
6	9	505.5	0.01907	8.136	21.36 ± 3.08	642 ± 41.7
7	12	528.5	0.02402	7.471	26.91 ± 2.35	694 ± 31.4
8	13	495.5	0.02776	7.053	31.11 ± 2.73	697 ± 16.3
9	13	508.5	0.02686	7.148	30.09 ± 2.19	705 ± 36.7
10	14	525.0	0.02820	7.008	31.59 ± 2.79	753 ± 49.7
11	15	511.0	0.03123	6.714	34.99 ± 3.05	704 ± 29.9
12	19	512.5	0.03930	6.051	44.04 ± 3.02	707 ± 23.7

† 1 kg force and 15 s hold time

where d is the austenite grain diameter (μm), A a constant, Q the activation energy for grain growth (J/mol), R the universal gas constant (8.314 $J/molK$), T the austenitizing temperature (K), t the austenitizing time (s), and n a time exponent constant. The activation energy is only a function of the composition of the steel which is constant throughout the experiments conducted here. With d, R, T, and t known, the experimental data points were fitted to Equation 5.1 resulting in values of $A = 11998$, $Q = 69874$ J/mol and $n = 0.1478$.

Substituting values of T and t, the grain size diameters were predicted using Equation 5.1. These predictions were used along with the experimental values to perform a standardized residual test to identify any outliers in the experimental data set. The predicted grain sizes and the results of the residual test are shown in Table 5.5. There are no outliers in the measured data as all the standardized residuals are within the interval of (-2, 2) (Berthold et al., 2010).

Table 5.5: Predicted and measured grain diameters and their standardized residuals for all samples.

Sample	Experimental grain diameter (μm)	Predicted grain diameter (μm)	Standardized residuals	Error* (%)
1	16.42	15.35	0.13	6.5
2	18.51	17.01	0.19	8.1
3	22.46	21.58	0.11	3.9
4	25.79	23.90	-0.24	7.3
5	15.64	20.58	-0.61	-31.5
6	21.36	22.79	-0.18	-6.7
7	26.91	28.92	-0.25	-7.5
8	31.11	32.04	0.12	-3.0
9	30.09	26.95	0.39	10.5
10	31.59	29.86	0.22	5.5
11	34.99	37.87	-0.36	-8.2
12	44.04	41.96	0.26	4.7

Error=$\frac{experimental-predicted}{experimental} \times 100$

Comparing the experimental grain diameters to those calculated using the empirical model, it was found that the model predicted values with an error less than 8.6%. Two parameters can be used to describe the accuracy of the model as discussed in (Lee and Lee, 2008). Parameter D, the average *absolute* distance between the ideal predictions and the experimental measurements, and parameter E, the average *signed* distance between the ideal predictions and the experimental measurements. Equation 5.2 and Equation 5.3 show how these two parameters (units of ASTM grain size number) are calculated.

$$D = \frac{\sum_{i=1}^{N} \left| \frac{1}{\sqrt{2}}(d_{pred} - d_{exper}) \right|}{N} \tag{5.2}$$

$$E = \frac{\sum_{i=1}^{N} \left[\frac{1}{\sqrt{2}}(d_{pred} - d_{exper}) \right]}{N} \tag{5.3}$$

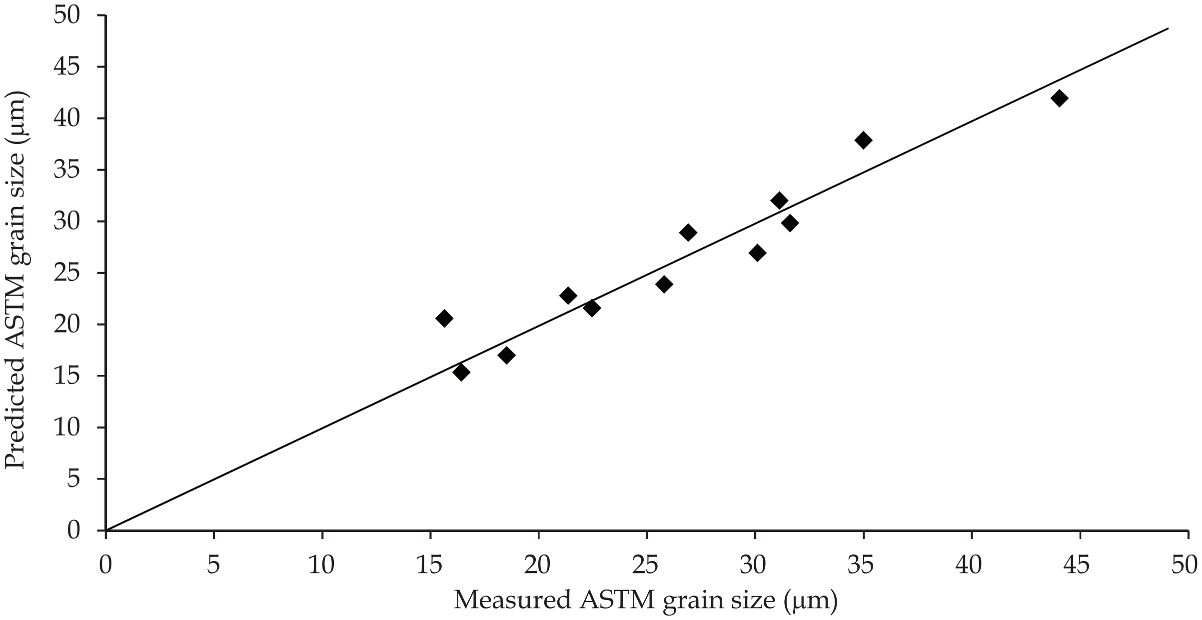

Figure 5.3: Graphical comparison of the measured and predicted austenite grain diameters for the 12 samples. The curve is fit with R^2=0.9097. D=1.44 and E=-0.0068 (see Equation 5.2 and Equation 5.3 for definitions).

The term N in these equations denotes the number of experimental data points. Smaller values of D indicate a better match between predicted and experimental values, while E indicates whether the empirical equation (Equation 5.1) is, on average, predicting values that are too high (positive values) or too low (negative values). The calculated D value of 1.44 indicates that a good match between the experimental and predicted values exist. The calculated E value of -0.0068 indicates that on average, Equation 5.1 predicts values that are very close to the experimental values (slight underestimation since it is a negative number). Figure 5.3 shows a graphical comparison of the predicted austenite grain diameter versus the experimentally measured values.

5.5 Determination of M_s and M_f

The determination of the temperature at which martensite starts to form (M_s) during cooling has important practical implications, for example in the design of heat treatments, welding consumables (Alghamdi and Liu, 2014; Zenitani et al., 2007), or to use inside predicting formulas such as the well-known Koistinen-Margurger (KM) equation and its many successors (Koistinen and Marburger, 1959; Sourmail and Smanio, 2013a; Yang et al., 2012).

A very important (and seldom acknowledged) challenge in the determination of M_s is that there is no universal agreement on a definition of M_s. More importantly, some definitions result in such different M_s values that they cause confusion in practice.

Most definitions of M_s can be grouped in two categories: those based on thermodynamics (used in (Kaufman and Cohen, 1958; Ghosh and Olson, 1994a,b; Bhadeshia, 1981a,b)) and those based on empirical measurements (e.g. ASTM and KM). The most important difference between these two groups is that M_s definitions based on thermodynamics aim to identify the first appearance of martensite, while the empirical definitions aim to identify an arbitrary measurable amount of martensite. As a consequence, thermodynamic-based definitions typically result in higher values than empirical definitions.

The experimental determination of the first appearance of martensite during cooling is challenging, and limited by the resolution of the instrument and the behavior of the alloy. Occasionally, the slope variations in the dilation curves is so shallow that identifying an M_s with any method can lead to appreciable errors. Experiments show that the evolution of martensite fraction during cooling has a relatively smooth start, yielding a sigmoidal curve. In contrast, the KM equation assumes a sharp start of martensite evolution, with a clearly determined M_s. Typically, the determination of M_s by matching the KM equation to empirical data results in M_s temperatures corresponding to measurable martensite fractions. This M_s temperature obtained by fitting the KM equation is clearly below the M_s temperature corresponding to the thermodynamic equilibrium of martensite.

Six M_s definitions are considered in this paper: 1) ASTM A1033 (ASTM A1033-10, 2013), 2) the tangent method, 3) the offset method (Yang and Bhadeshia, 2007), 4) cooling curve analysis (Gibbs, 2009; Gibbs and Mendez, 2008; Gibbs et al., 2014), 5) dilation curve analysis (Gibbs et al., 2014), 6) SteCal V3.0 software (P et al., 2004).

ASTM A1033 is an empirical measurement that defines the critical temperatures as ”*...strain will begin to decrease with increasing temperature...*” or ”*...strain will again begin to increase with increasing temperature...*” which is typically interpreted as defining M_s as the temperature at which the dilation curve experiences a minimum in the region of interest, as illustrated in Figure 5.5. This definition does not account for noise in the dilation curve, which is typically small, but is observable in the data collected using modern, highly sensitive dilatometers. During cooling and before the dilation curve reaches a minimum, some small amount of martensite is produced; therefore this method does not measure the first appearance of martensite, which occurs at higher temperatures.

The tangent method is another empirical measurement often embedded in dilatometer software packages, and is illustrated in Figure 5.4 and Figure 5.5. This method defines M_s as the temperature at which two tangents to the dilation curve intersect. There are no formal rules for the choice of the tangents, and they are chosen based on ”good judgment”, which involves a small degree of subjectivity and variation based on the operator. Typically, the tangent method yields M_s values similar to ASTM A1033, and lower than thermodynamic methods.

The offset method was developed to systematically identify from dilation curves a value of M_s close to the thermodynamic data. A small value of martensite fraction is arbitrarily chosen to determine M_s, typically 1%. This method requires the choice of a tangent to the dilation curve that represents the contraction of austenite, as shown in Figure 5.5.

Similarly to the tangent method, good judgment is used to choose the tangent. For alloy and dilatometer combinations where martensite presents a smooth start during cooling, small variations in the choice of the tangent can result in appreciable differences in M_s (Sourmail and Smanio, 2013b).

Cooling curve analysis (CCA) and dilation curve analysis (DCA) were developed to quantify as accurately as possible micro-constituent fraction evolution from common experiments such as free cooling or dilatometer experiments. These techniques allow for the detection of small amounts of martensite, with the lower limit given mainly by signal noise. It is possible to relate the definition of M_s of other techniques to the actual amount of martensite present in the microstructure measured using CCA or DCA. DCA typically yields lower M_s values than CCA because DCA dilation corresponds to the whole sample, but temperature measurements are local to the surface of the sample; thus, transformations that occur at the center of the sample are assigned the lower temperatures corresponding to the surface (the difference is relatively small, as analyzed in (Gibbs et al., 2014)). CCA is likely a better measurement since it measures local transformations in the vicinity of the thermocouple; an in-depth comparison of these techniques is in (Kamyabi-Gol et al., 2015). Both CCA and DCA require good judgment in the choice of tangents, but in contrast with other techniques, these tangents are part of a deeper analysis that can account for smooth variations in thermal expansion coefficient or cooling conditions. The choice of tangents in these methods is more robust than the tangent method or the offset method.

CCA and DCA analysis show that for all samples the evolution of martensite started smoothly without a sharp starting point. Comparison with the tangent method showed an average martensite fraction of 13.4% with a 95% confidence interval of ±6.4% at the M_s temperature determined with the tangent method. Within the error determined, CCA or DCA would yield essentially the same M_s values of ASTM A1033 or the tan-

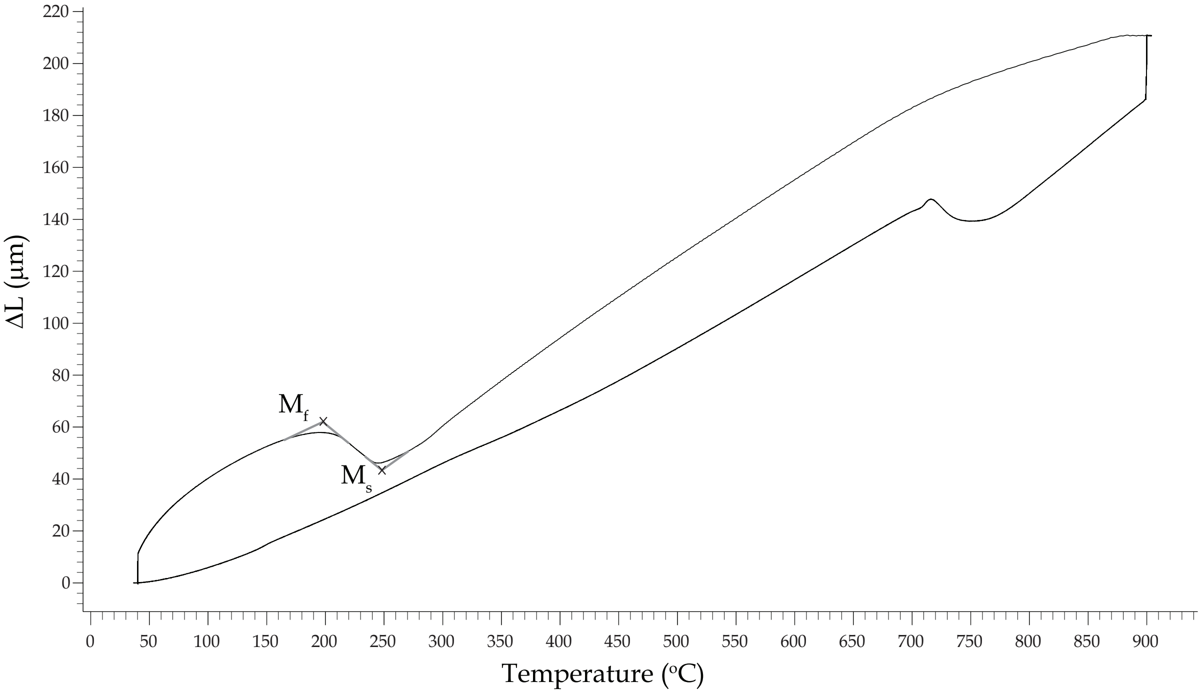

Figure 5.4: Tangent method used to determine martensite start and finish temperatures (dilation curve for Sample 3).

gent method when considering the practical rounded value of 10% of martensite fraction. Martensite fractions calculated with DCA could match the target martensite fraction of 1% at the M_s temperature determined with the offset method, but could also depart significantly from the intended 1% with slightly different choices of tangent for the contraction of austenite.

SteCal software uses empirical formulas for M_s that relate the steel composition to empirical values of M_s (ASTM A1033 or tangent method). Initial austenite grain size cannot be included in the software. On average, Stecal V3.0 predictions are approximately 75 K higher than measured with other techniques.

Similar considerations apply to the determination of M_f, except that the offset method does not apply to M_f.

M_s and M_f values for all the 12 samples obtained from all the methods are given in

Table 5.6: Comparison of martensite start and finish temperatures obtained from the tangent method, cooling curve analysis, dilation curve analysis and the offset method.

Sample	Measured austenite grain diameter (μm)	M_s from the tangent method (K)	M_s from the offset method* (K)	M_s from CCA$^\bullet$ (K)	M_s from DCA$^\bullet$ (K)	M_f from the tangent method (K)	M_f from CCA† (K)	M_f from DCA† (K)	$f_{M_{Tan-DCA}}$ $^\diamond$ (mass%)	$f_{M_{Tan-CCA}}$ ‡ (mass%)
1	16.42	509	515.3	505.5	504.6	461	441.8	442.3	4%	8%
2	18.51	520	536.7	546.9	526.4	474	457.9	456.6	22%	24%
3	22.46	530	536.3	555.0	528.2	476	460.3	441.1	8%	22%
4	25.79	532	541.6	560.5	527.6	475	460.5	448.0	4%	21%
5	15.64	523	544.0	552.5	538.0	477	457.5	462.2	39%	23%
6	21.36	524	529.8	553.4	525.0	478	456.6	459.3	11%	24%
7	26.91	531	530.3	566.3	537.9	477	461.5	458.5	27%	24%
8	31.11	536	544.1	571.8	538.8	478	466.4	454.7	13%	26%
9	30.09	535	535.6	509.2	537.2	466	447.5	483.4	12%	2%
10	31.59	541⋆	552.4	518.9	548.1	467	450.1	478.8	21%	5%
11	34.99	549⋆	523.8	544.7	519.4	471	452.9	458.1	0%	9%
12	44.04	575⋆	527.6	558.1	531.0	475	461.9	471.3	0%	4%

The value for M_s obtained from SteCal V3.0 is 601 K for all twelve samples.

∗ refer to (Yang and Bhadeshia, 2007) for further details about the method.

• based on 10 mass% martensite formation.

† based on 90 mass% martensite formation.

◊ equivalent mass% of martensite from the DCA method at the measured M_s temperature from the tangent method.

‡ equivalent mass% of martensite from the CCA method at the measured M_s temperature from the tangent method.

⋆ dilatometry curves were very shallow and M_s could not be measured accurately using the tangent method.

Table 5.6. The effect of prior austenite grain size on martensite transformation kinetics was then determined using the values obtained from all six methods.

5.6 Effect of austenite grain size on M_s and M_f

To establish the effect of austenite grain size on martensite transformation kinetics, CCA and DCA were used according to (Gibbs, 2009; Gibbs et al., 2014; Gibbs and Mendez, 2008), to plot and calculate the martensite fraction curves as a function of temperature

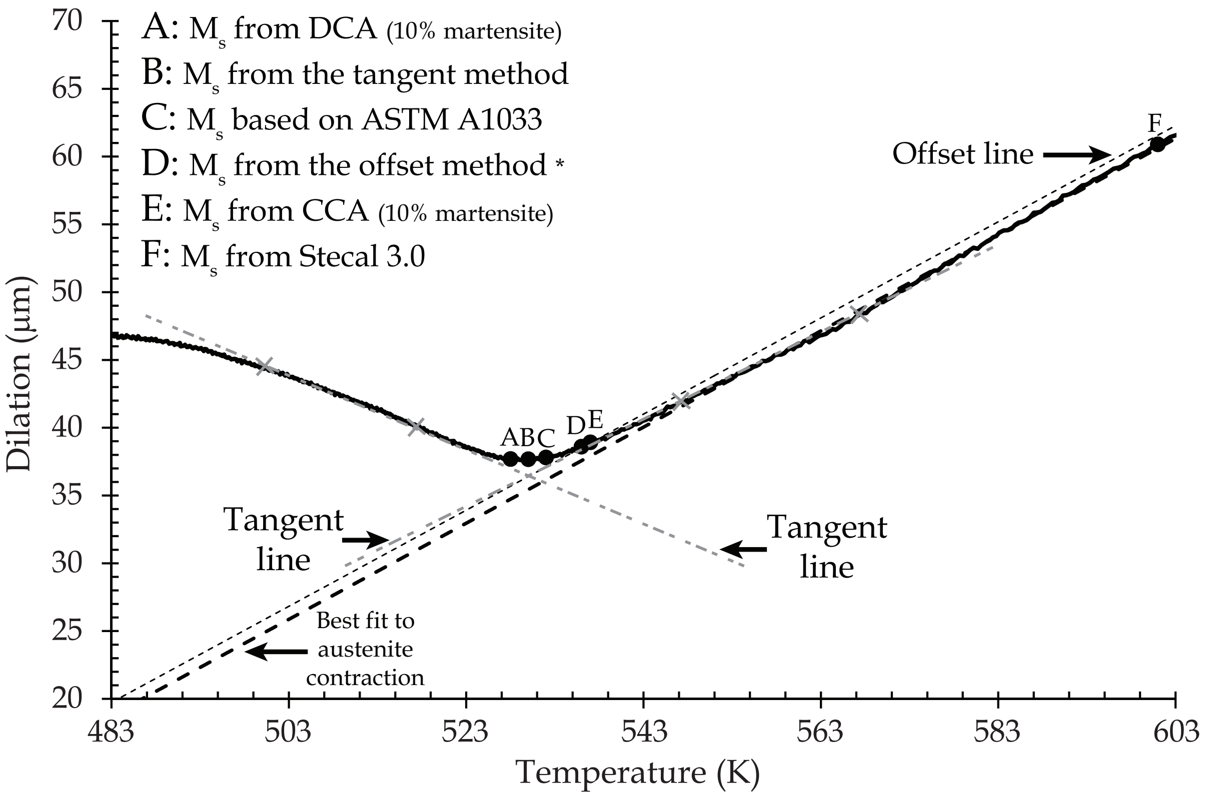

* H.-S. Yang and H. K. D. H. Bhadeshia, "Uncertainties in dilatometric determination of martensite start temperature," Mater. Sci. Technol., vol. 23, no. 5, pp. 556–560, May 2007.

Figure 5.5: Martensite start temperature (M_s) measured using six different methods for Sample 3.

for all of the samples. The martensite start temperature (and in some cases the martensite finish temperature) for the twelve samples were measured and compared using the 6 previously described methods. The value for M_s obtained for all twelve samples from SteCal V3.0 is 601 K. M_s values for Sample 3 obtained from all six methods are illustrated and compared together in Figure 5.5 and Figure 5.6.

The martensite fraction curves for all the samples austenitized at 1173 K obtained through CCA are illustrated in Figure 5.7. Similar curves for the samples austenitized at 1223 K and 1273 K are shown in Figure 5.8 and Figure 5.9, respectively. Tt was deduced that smaller prior austenite grains yield faster martensite formation and at lower temperatures.

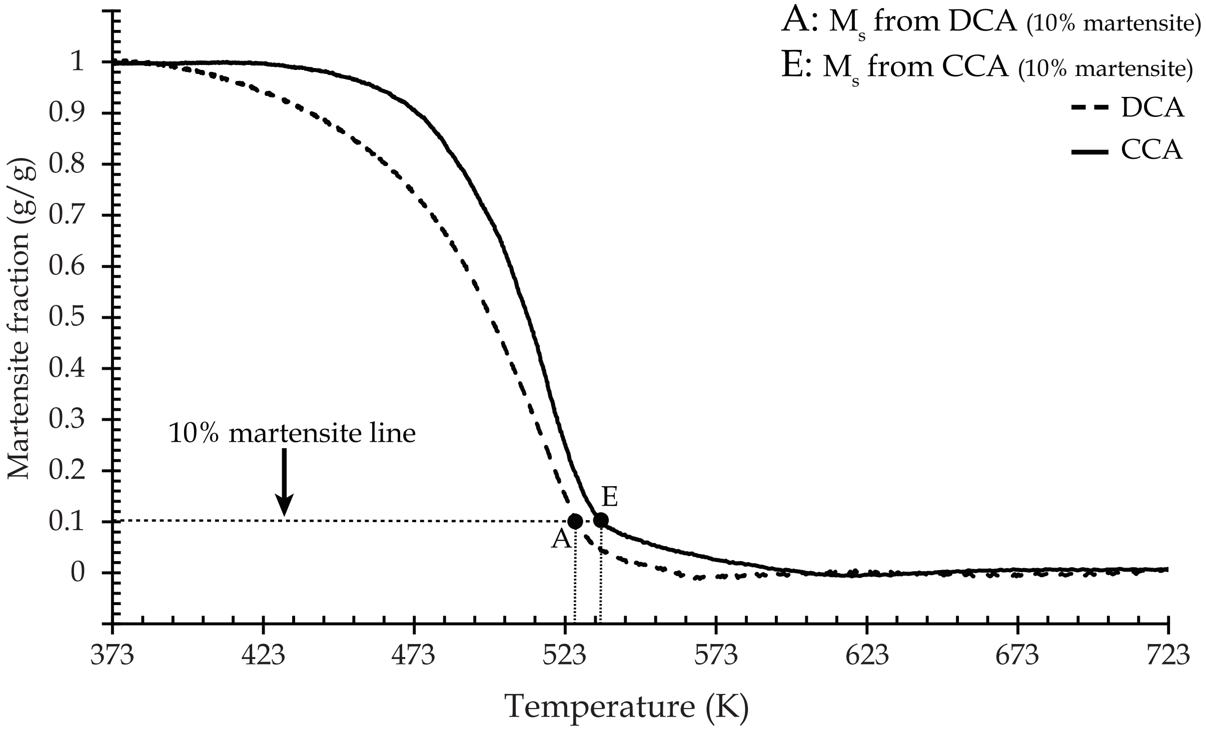

Figure 5.6: Martensite start temperature measured for Sample 3 using CCA and DCA methods. The martensite start temperature is defined as the temperature where the mass fraction of martensite is equal to 10%. Points A and E are illustrated in Figure 5.5.

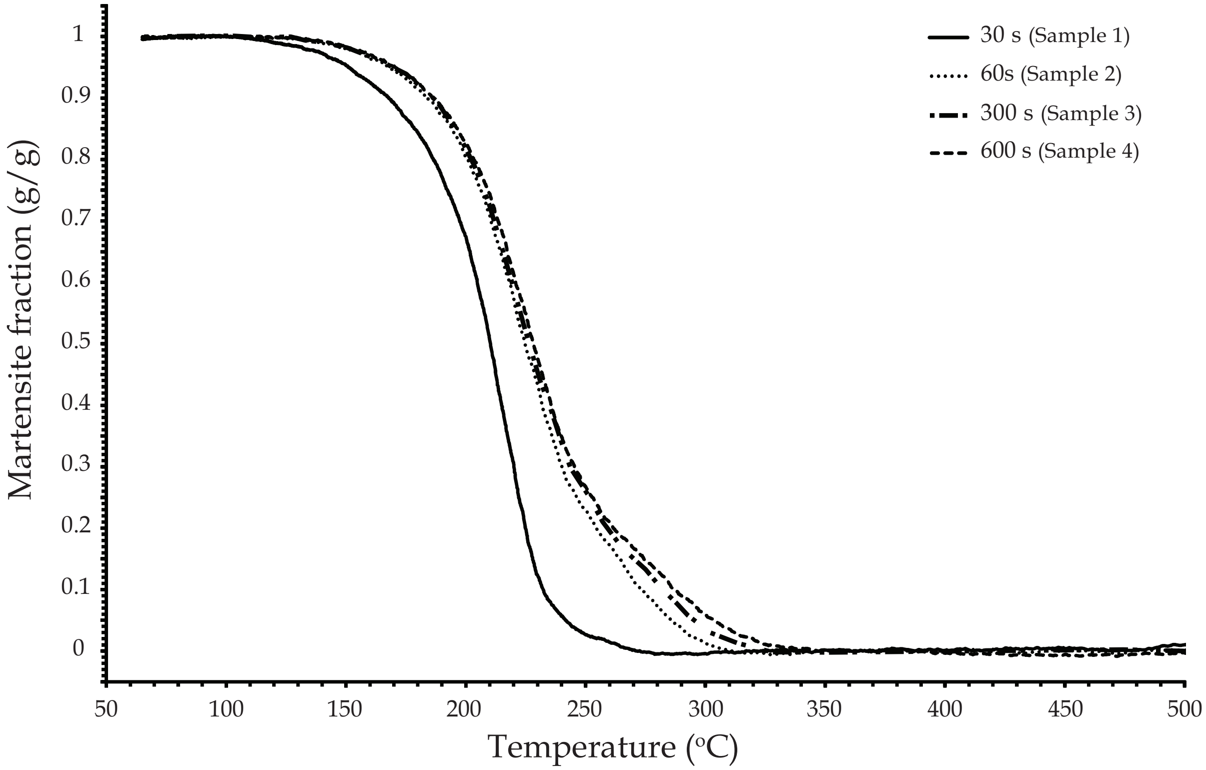

Figure 5.7: Martensite fraction curves as a function of temperature for Samples 1-4 (all austenitized at 1173 K) obtained using CCA.

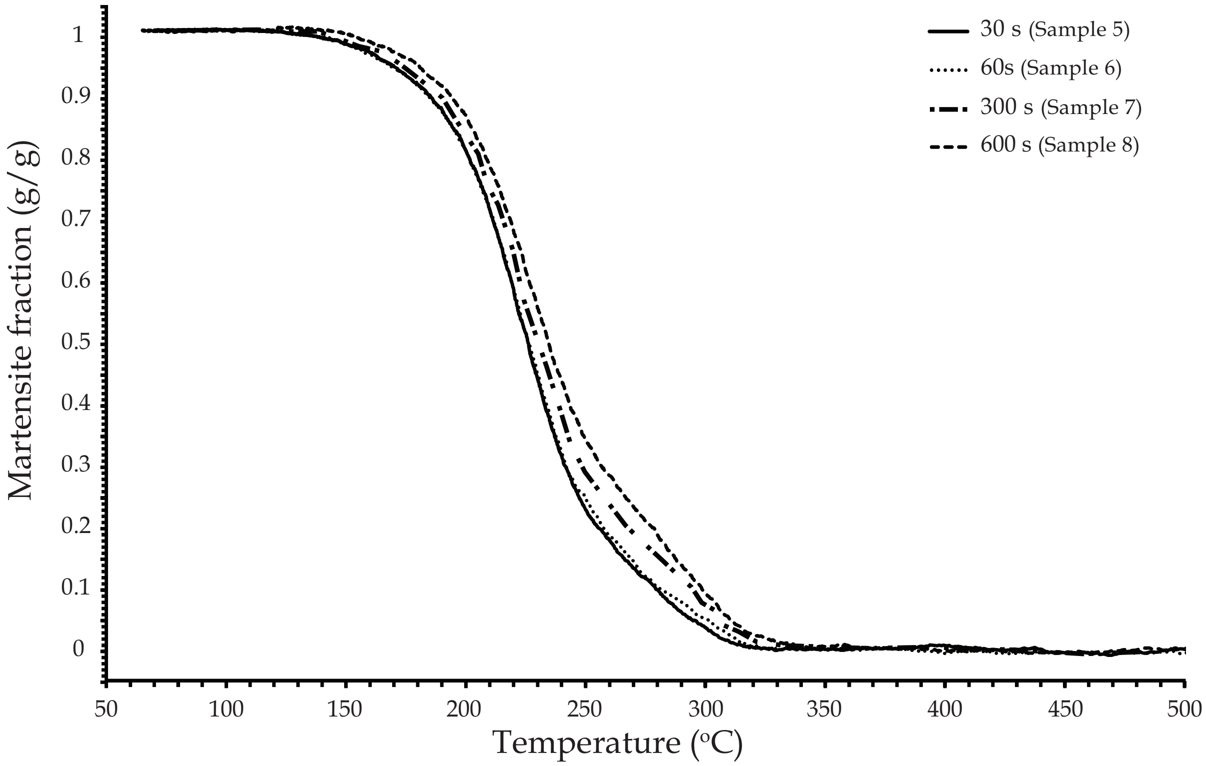

Figure 5.8: Martensite fraction curves as a function of temperature for Samples 5-8 (all austenitized at 1223 K) obtained using CCA.

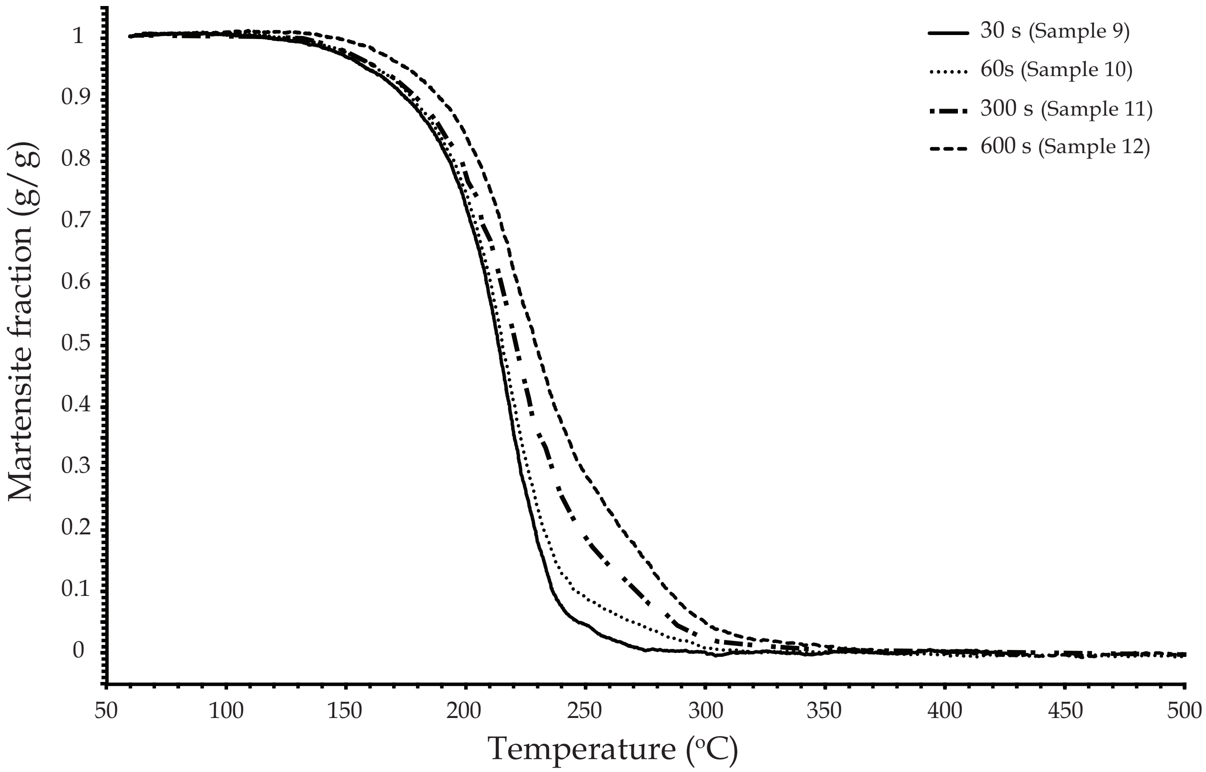

Figure 5.9: Martensite fraction curves as a function of temperature for Samples 9-12 (all austenitized at 1273 K) obtained using CCA.

5.7 Effect of austenite grain size on the CCT diagram

To investigate the effect of prior austenite grain size on the continuous cooling transformation (CCT) diagram, 3 samples with various austenite grain sizes were chosen. A CCT diagram was constructed for each of these samples. Table 5.2 lists the chosen samples (Sample 5, 9, and 12) and the heating conditions applied to them. These samples were chosen as they had widely different prior austenite grain sizes (refer to Table 5.4 for the grain diameters). Figure 5.10, Figure 5.11, and Figure 5.12 show the three CCT diagrams corresponding to Samples 5, 9, and 12 respectively. The transformation start and finish temperatures for each of the phases were determined using the tangent method as shown in Figure 5.4, where slope changes of the dilation curves signified the beginnings or ends of phase transformations. This technique was also used to determine Ac_1 and Ac_3 (the beginning and end of the formation of austenite upon heating). It was found that by decreasing the austenite grain size, the transformation curves in the CCT diagrams shifted upwards and to the left.

5.8 Discussion

The offset method introduced in (Yang and Bhadeshia, 2007) is one of the most recent and promising systematic approaches to measuring the martensite start temperature from dilation data. However, several simplifying assumptions made in construction of this method will affect the reliability of the results obtained in this study. These assumptions are: assuming martensite has a cubic crystal structure when it is tetragonal in reality, assuming martensite has two *iron* atoms in the unit cell while the AISI 4140 steel used in this research has many other substitutional atoms, and the equation used

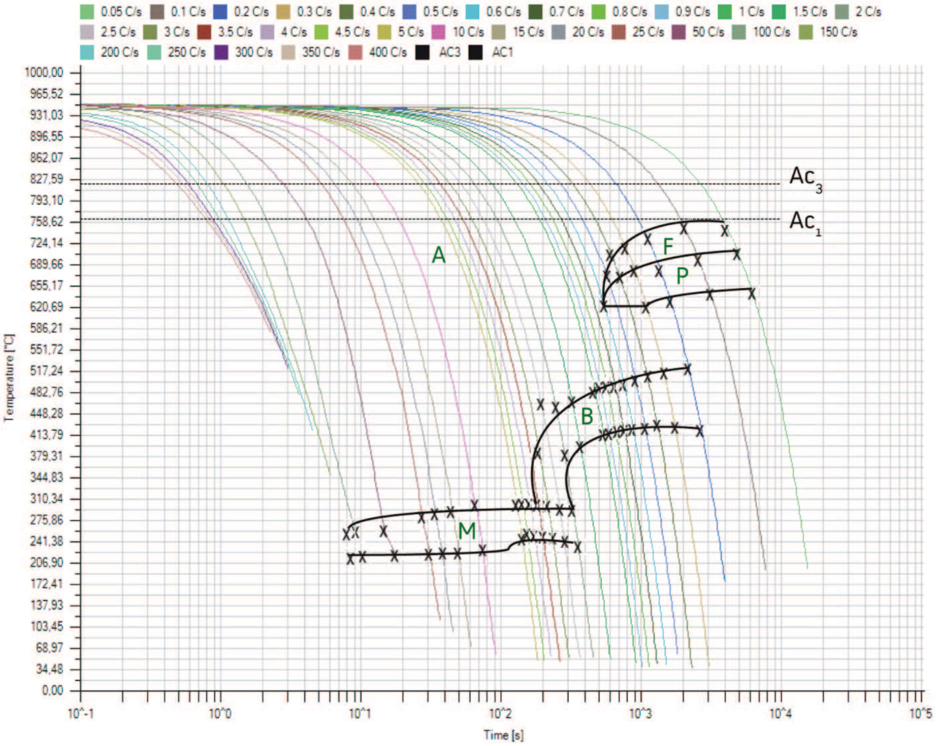

Figure 5.10: CCT diagram for Sample 5 (austenitized at 1223 K for 30 seconds). Average austenite grain size of 15.64 ± 0.90 μm.

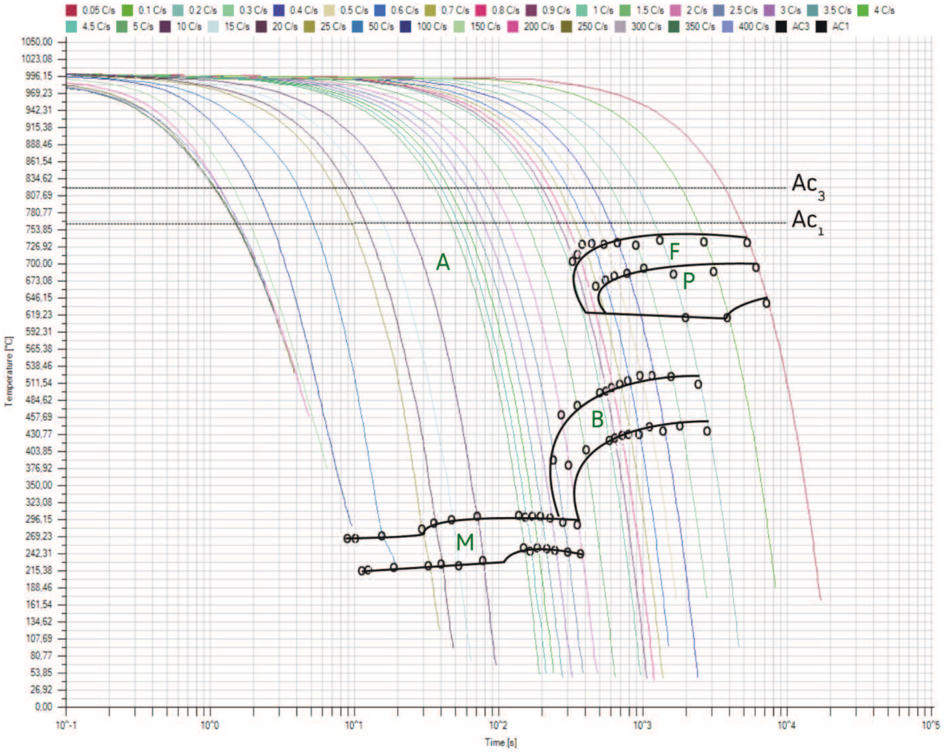

Figure 5.11: CCT diagram for Sample 9 (austenitized at 1273 K for 30 seconds). Average austenite grain size of 30.09 ± 2.19 μm.

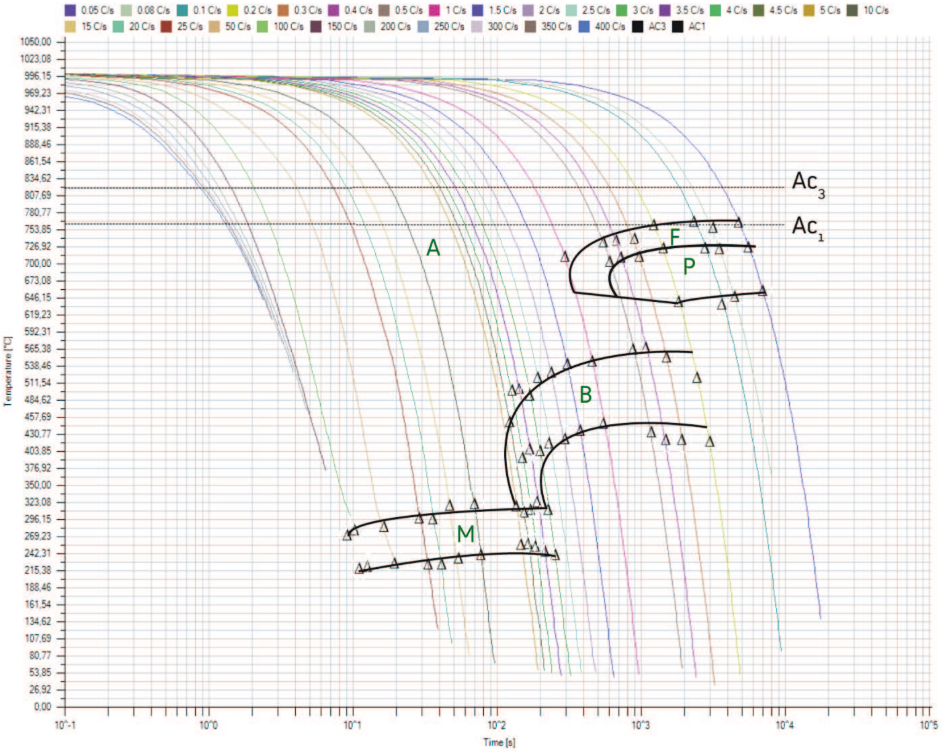

Figure 5.12: CCT diagram for Sample 12 (austenitized at 1273 K for 600 seconds). Average austenite grain size of 44.04 ± 3.02 μm.

to calculate the martensite lattice parameter does not include all the elements in the composition of the steel, mainly copper is not included. All these assumptions could have affected the M_s values calculated in this study.

Comparing the CCT diagrams for different austenite grain sizes reveals that the transformation start and finish temperatures increased, and the transformation start and finish times decreased as the austenitization temperature and time decreased i.e. the CCT curves shifted upwards and to the left with decreasing austenite grain size. This indicates that transformations begin and end faster and at higher temperatures, meaning less energy is required to initiate phase transformations. This could be due to heterogeneous nucleation, i.e nucleation at austenite grain boundaries, of all the phases in the CCT diagrams. Smaller austenite grains increase the grain boundary surface area promoting nucleation by increasing the area and density of nucleation sites. This reduces the overall energy barrier of phase transformations which consequently means that less undercooling and less time is required to trigger a phase transformation.

5.9 Conclusions

Twelve samples of AISI 4140 steel were austenitized and held at different temperatures for different periods of time to vary the austenite grain sizes. It was found that the austenite grain size increased as the austenitization temperature and time increased as indicated in Table 5.2 and Table 5.5. Using these measured austenite grain diameters, an empirical model as shown in Equation 5.4 was developed to predict the austenite grain size as a function of austenitizing temperature and time with an error smaller than 8.6% as indicated in Table 5.5.

$$d = 11998 \exp\left(-\frac{8404.38}{T}\right) t^{0.1478} \tag{5.4}$$

where d is the austenite grain diameter (μm), T the austenitizing temperature (K), t the austenitizing time (s).

Table 5.6 summarizes the M_s values measured using six different methods: the tangent method, the offset method, according to ASTM A1033, cooling curve analysis (CCA), dilation curve analysis (DCA) and SteCal V3.0. It was found that on average the M_s values from the tangent method roughly correspond to an M_s equivalent to 13.4±6.4% martensite from the DCA method. Similarly, it was found that the value of M_f measured using the tangent method roughly corresponds to an M_f equivalent to 90% martensite from the CCA and DCA methods. CCA and DCA were also used to plot the martensite fraction evolution with temperature for all of the samples. From these fraction curves, it was deduced that smaller prior austenite grains yield faster martensite formation and at lower temperatures. Finally, 3 CCTs were constructed for 3 samples of different austenite grain diameters (15.64 μm, 30.09 μm, 44.04 μm). Comparing these 3 CCT diagrams, it was found that by decreasing the austenite grain size, the transformation curves in the CCT diagrams shifted upwards and to the left as illustrated in Figure 5.10, Figure 5.11 and Figure 5.12.

5.10 Acknowledgement

The authors would like to acknowledge Codes And Standards Training Institute (CASTI), MITACS and Natural Sciences and Engineering Research Council of Canada (NSERC) for their support of this work.

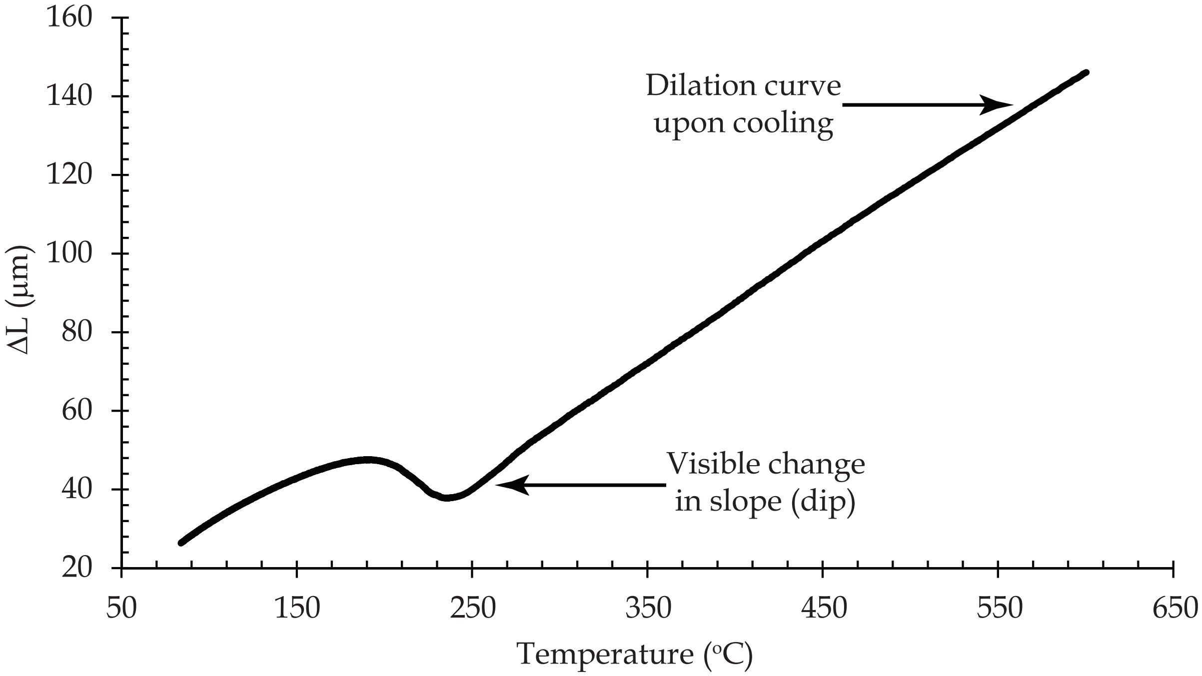

Figure 5.13: Dilation curve for Sample 1 showing a minor dip in the curve just before the start of the martensite transformation.

5.11 Appendix

5.11.1 Observed anomaly in the dilation curves

The dilation curves for some of the samples studied in this research showed an anomaly. In these samples, the dilation curve (contraction of austenite) shows a minor dip just before the start of the martensite transformation. This dip is clearly shown in Figure 5.13 for Sample 1. The change in the slope of the dilation curve is even more visible in the derivative of the dilation curve as shown in Figure 5.14 for Sample 1.

The reason behind this change in the slope of austenite contraction is not known and requires deeper analysis.

5.12 References

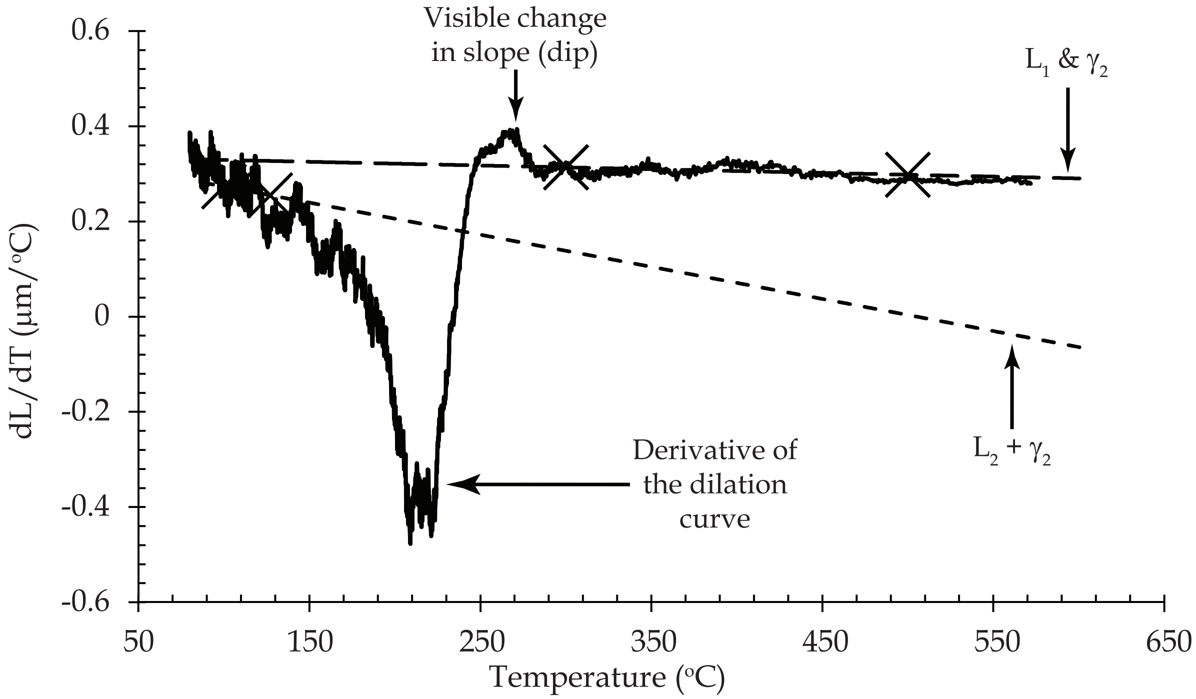

Figure 5.14: Derivative of the dilation curve for Sample 1 showing a minor dip in the curve just before the start of the martensite transformation.

Alghamdi, T., Liu, S., 2014. Low-Transformation-Temperature (LTT) Welding Consumables for Residual Stress Management: Consumables Development and Testing Qualification. Welding Journal 93, 243–s–252–s.

ASTM A1033-10, 2013. Standard Practice for Quantitative Measurement and Reporting of Hypoeutectoid Carbon and Low-Alloy Steel Phase Transformations 1, pp. 1–14.

ASTM E112-13, 2013. Standard Test Methods for Determining Average Grain Size, in: ASTM International, pp. 1–28.

Berthold, M.R., Borgelt, C., Höppner, F., Klawonn, F., 2010. Guide to Intelligent Data Analysis: How to Intelligently Make Sense of Real Data. Texts in Computer Science, Springer.

Bhadeshia, H.K.D.H., 1981a. Driving force for martensitic transformation in steels. Metal Science 15, 175–177.

Bhadeshia, H.K.D.H., 1981b. Thermodynamic extrapolation and martensite-start temperature of substitutionally alloyed steels. Metal Science 15, 178–180.

Bokrost, J.C., Parker, E., 1963. THE MECHANISM OF THE MARTENSITE BURST IN Fe-Ni SINGLE CRYSTALS. Acta Metallurgica 11, 1291–1301.

Brofman, P., Ansell, G., 1983. On the effect of fine grain size on the M s temperature in Fe-27Ni-0.025 C alloys. Metallurgical and Materials Transactions A 14, 1929–1931.

Callister, W.D., Rethwisch, D.G., 2012. Fundamentals of Materials Science and Engineering: An Integrated Approach. Wiley.

Fisher, J., Hollomon, J., Turnbull, D., 1949. KINETICS OF THE AUSTENITE-] MARTENSITE TRANSFORMATION. Metals Transactions 185, 691–700.

Ghosh, G., Olson, G., 1994a. Kinetics of F.C.C. B.C.C. heterogeneous martensitic nucleationI. The critical driving force for athermal nucleation. Acta Metallurgica et Materialia 42, 3361–3370.

Ghosh, G., Olson, G., 1994b. Kinetics of F.c.c. b.c.c. heterogeneous martensitic nucleationII. Thermal activation. Acta Metallurgica et Materialia 42, 3371–3379.

Gibbs, J.W., 2009. Thermal Analysis Techniques for Phase Fraction Measurements of First-order Phase Transformations. Msc. Colorodo School of Mines.

Gibbs, J.W., Mendez, P.F., 2008. Solid fraction measurement using equation-based cooling curve analysis. Scripta Materialia 58, 699–702.

Gibbs, J.W., Schlacher, C., Kamyabi-Gol, A., Mayr, P., Mendez, P.F., 2014. Cooling Curve Analysis as an Alternative to Dilatometry in Continuous Cooling Transformations. Metallurgical and Materials Transactions A 46, 148–155.

Giumelli, A., Militzer, M., Hawbolt, E., 1999. Analysis of the austenite grain size distribution in plain carbon steels. ISIJ international 39, 271–280.

Huang, J., Xu, Z., 2006. Effect of dynamically recrystallized austenite on the martensite start temperature of martensitic transformation. Materials Science and Engineering: A 438-440, 254–257.

Jiao, S., Penning, J., Leysen, F., Houbaert, Y., Aernoudt, E., 2000. The Modeling of the Grain Growth in a Continuous Reheating Process of a Low Carbon Si-Mn Bearing TRIP Steel. ISIJ International 40, 1035–1040.

Kamyabi-Gol, A., Gibbs, J.W., Mendez, P.F., 2015. Advanced mathematical treatment of dilatometry and calorimetry to discriminate and quantify multiple phase transformations, in: Proceedings of the International Conference on Solid-Solid Phase Transformations in Inorganic Materials 2015, Whistler, BC, Canada. pp. 1199–1206.

Kaufman, L., Cohen, M., 1958. Thermodynamics and kinetics of martensitic transformations. Progress in Metal Physics 7, 165–246.

Koistinen, D., Marburger, R., 1959. A general equation prescribing the extent of the austenite-martensite transformation in pure iron-carbon alloys and plain carbon steels. Acta Metallurgica 7, 59–60.

Lee, S.J., Lee, Y.K., 2005. Effect of Austenite Grain Size on Martensitic Transformation of a Low Alloy Steel. Materials Science Forum 475-479, 3169–3172.

Lee, S.J., Lee, Y.K., 2008. Prediction of austenite grain growth during austenitization of low alloy steels. Materials & Design 29, 1840–1844.

Militzer, M., Giumelli, A., Hawbolt, E., Meadowcroft, T., 1996. Austenite grain growth kinetics in Al-killed plain carbon steels. Metallurgical and Materials Transactions A 27, 3399–3409.

P, T., Martín, J.P., Perez, J., 2004. SteCal 3.0: User Manual. Asm International.

Reti, T., Fried, Z., Felde, I., 2001. Computer simulation of steel quenching process using a multi-phase transformation model. Computational Materials Science 22, 261–278.

Saito, Y., Shiga, C., 1992. Computer Simulation of Microstructural Evolution in Thermomechanical Processing of Steel Plates. ISIJ international 32, 414–422.

Sarma, D., Whiteman, J., Keown, S., 1979. The structure of burst and isothermal martensites in an Fe-24 wt% Ni-0.5 wt% C alloy. Journal of Materials Science 14, 693–698.

Sourmail, T., Smanio, V., 2013a. Determination of M s temperature: methods, meaning and influence of slow start phenomenon. Materials Science and Technology 29, 883–888.

Sourmail, T., Smanio, V., 2013b. Response to comments on Determination of M s temperature: methods, meaning and influence of slow start phenomenon by T. Sourmail and V. Smanio. Materials Science and Technology 29, 890–892.

Suárez, J., Molleda, F., de Salazar, J.G., 1992. Modeling of grain growth during arc welding of high strength low alloy steels. Materials characterization 28, 3–13.

Yang, H., Bhadeshia, H., 2009. Austenite grain size and the martensite-start temperature. Scripta Materialia 60, 493–495.

Yang, H.S., Bhadeshia, H.K.D.H., 2007. Uncertainties in dilatometric determination of martensite start temperature. Materials Science and Technology 23, 556–560.

Yang, H.S., Jang, J.H., Bhadeshia, H.K.D.H., Suh, D.W., 2012. Critical assessment: Martensite-start temperature for the γ ϵ transformation. Calphad: Computer Coupling of Phase Diagrams and Thermochemistry 36, 16–22.

Yoshie, A., Fujioka, M., Watanabe, Y., 1992. Modelling of microstructural evolution and mechanical properties of steel plates produced by thermo-mechanical control process. ISIJ international 32, 395–404.

Zenitani, S., Hayakawa, N., Yamamoto, J., Hiraoka, K., Morikage, Y., Kubo, T., Yasuda, K., Amano, K., 2007. Development of new low transformation temperature welding consumable to prevent cold cracking in high strength steel welds. Science and Technology of Welding and Joining 12, 516–522.

Chapter 6

Conclusions and Future work

6.1 Conclusions and Summary of Findings

The integration methodology developed for the analysis of cooling curves and dilatometric data has been tested successfully in a broad range of materials: 10 variations of cast aluminum A356 alloy (Kamyabi-Gol and Mendez, 2014), 9Cr3W3CoVNb steel (Gibbs et al., 2014), and AISI 4140. It is reasonable to expect this methodology to be applicable in many other materials of practical significance, limited only by the sensitivity of the measurement technique for complete single transformations. For example, small amounts of precipitation might be difficult to quantify.

For partial transformations or multiple transformations, additional data is necessary: thermodynamic data and (in some cases) quantitative metallography for CCA, and density data for dilatometry. In some cases, the needed data can be obtained from analysis of samples of the same material at different cooling rates such that the transformations become complete, or a multiple transformation problem turns into a single transformation one.

In the case of calorimetry, cooling rate and size of the sample are related, and attention must be paid to experiment design. For both calorimetry and dilatometry, sample temperature homogeneity must be considered carefully. In the experiments discussed in the previous chapters, the Biot number was always small, ensuring temperature homogeneity. In addition, there were no longitudinal gradients such as those often present in Gleeble testing.

One of the advantages of the integration procedure proposed, is that it can be extended to problems beyond those tested. In both calorimetry and dilatometry, analysis during heating is possible; for dilatometry this is trivial, but for calorimetry this involves the use of furnaces (either convective or radiative) and might have limitations in practice. The analysis of steels during heating is especially relevant currently because of the fast growth of laser heat treatments, in which there is ample (circumstantial) evidence that full austenitization (Ac_3) is reached at temperatures significantly above the thermodynamic value (A_3).

For the case of CCA, different well known boundary conditions can be treated rigorously. For sand casting, the heat transfer model would be based on Chvorinov's analysis instead of constant effective heat transfer coefficient. Cooling by radiation and combined radiation and convention can also be tackled. The application of CCA to sand casting, although possible in theory, has not been implemented successfully. It is thought that shrinkage can greatly affect the part/mold heat transfer parameters. Also, possible phase transformations in the sand might play a role. Future work on this area would be of significant practical value to casting operations. Substituting convection for conduction in CCA has the potential of creating a whole CCT diagram in a single Jominy test. Other possible extensions of CCA would bring an additional quantification of phase fractions to systems in which it is currently not practical to measure phase fraction; hot stage microscopy and welding are among such systems.

For the case of dilatometry, the multiple transformation methodology should be able to yield light into simultaneous transformations in steels. Typically simultaneous transformations are treated as if they were sequential and with similar density change, not simultaneous and with products of varying densities.

Proper quantification of phase fraction also provides control over the criterion to determine the start and finish of transformations. Instead of the traditional intersection of tangents (which any practitioner will recognize it can carry subjectivity at times), a clearly designated criterion for start and stop based on percentages such as 1%, 5%, 99%, etc. is possible.

For transformations such as martensite in steels, in which completion is occasionally reached well below room temperature, the determination of the end of the integration is occasionally not well defined. In these cases quantitative metallography is needed. What is remarkable, however, is that nearing the completion of the transformation, conditions resembling full transformation are typically present, allowing proper quantification (provided metallography of the sample is performed after testing). This convenient phenomenon is present in the traditional analysis of dilatometry too, and often used.

It is worth to highlight that the wealth of data brought by the integration proposed comes at very little incremental cost over the traditional tests. The system used for the solidification alloys is described in detail in (Gibbs, 2009), and no hardware modifications are needed for the enhanced analysis of dilatometry.

6.2 Future Work

- Apply and compare the developed CCA and DCA methods to more materials (e.g. X80 pipeline steel, stainless steels, etc.).
- Extend the DCA and CCA methods to isothermal transformations.
- Extend the CCA technique to the Jominy experimental setup to be able to obtain a continuous cooling transformation diagram from a single Jominy experiment.

- Extend the CCA method to casting applications by considering the potentially different modes of heat transfer.
- Develop a methodology to be able to predict phase fractions similar to CCA and DCA by using electrical resistivity-temperature data.
- Fit Johnson-Mehl-Avrami constants to the phase fraction curves to be able to understand the nucleation and growth mechanisms.
- Fit a two-portion equation partially based on the Koistinen-Margurger equation to the martensite fraction curves obtained from DCA for multiple steels to construct an empirical equation to be able to accurately reproduce the martensite fraction curve from the composition of any steels studied in the future.

6.3 References

Gibbs, J.W., 2009. Thermal Analysis Techniques for Phase Fraction Measurements of First-order Phase Transformations. Msc. Colorado School of Mines.

Gibbs, J.W., Schlacher, C., Kamyabi-Gol, A., Mayr, P., Mendez, P.F., 2014. Cooling Curve Analysis as an Alternative to Dilatometry in Continuous Cooling Transformations. Metallurgical and Materials Transactions A 46, 148–155.

Kamyabi-Gol, A., Mendez, P.F., 2014. The Evolution of the Fraction of Individual Phases During a Simultaneous Multiphase Transformation from TimeTemperature Data. Metallurgical and Materials Transactions A 46, 622–638.

Bibliography

Alexandrov, B.T., Lippold, J.C., 2007. Single Sensor Differential Thermal Analysis of Phase Transformations and Structural Changes During Welding and Postweld Heat Treatment. Welding in the World 51, 48–59.

Alghamdi, T., Liu, S., 2014. Low-Transformation-Temperature (LTT) Welding Consumables for Residual Stress Management: Consumables Development and Testing Qualification. Welding Journal 93, 243–s–252–s.

Andersson, J.O., Helander, T., Hdghmd, L., Shi, P., Sundman, B., 2002. THERMO-CALC & DICTRA, Computational Tools For Materials Science. Calphad 26, 273–312.

de Andrés, C.G., Caballero, F., Capdevila, C., Bhadeshia, H.K.D.H., 1998. Modelling of kinetics and dilatometric behavior of non-isothermal pearlite-to-austenite transformation in an eutectoid steel. Scripta Materialia 39, 791–796.

ASTM A1033-10, 2013. Standard Practice for Quantitative Measurement and Reporting of Hypoeutectoid Carbon and Low-Alloy Steel Phase Transformations 1, pp. 1–14.

ASTM E112-13, 2013. Standard Test Methods for Determining Average Grain Size, in: ASTM International, pp. 1–28.

Bäckerud, L., Chai, G., Tamminen, J., 1990. Solidification Characteristics of Aluminium Alloys: Foundry Alloys. Solidification Characteristics of Aluminum Alloys, AFS/Skanaluminium.

Bakhtiyarov, S.I., Dupac, M., Overfelt, R.a., Teodorescu, S.G., 2004. On Electrical Conductivity Measurements of Molten Metals by Inductive Technique. Journal of Fluids Engineering 126, 468–470.

Barrena, M.I., Gómez de Salazar, J.M., Pascual, L., Soria, A., 2013. Determination of the kinetic parameters in magnesium alloy using TEM and DSC techniques. Journal of Thermal Analysis and Calorimetry 113, 713–720.

Béchade, J.L., Menut, D., Doriot, S., Schlutig, S., Sitaud, B., 2013. X-ray diffraction analysis of secondary phases in zirconium alloys before and after neutron irradiation at the MARS synchrotron radiation beamline. Journal of Nuclear Materials 437, 365–372.

Bergman, T.L., Incropera, F.P., Lavine, A.S., DeWitt, D.P., 2011. Fundamentals of Heat and Mass Transfer. Wiley.

Berthold, M.R., Borgelt, C., Höppner, F., Klawonn, F., 2010. Guide to Intelligent Data Analysis: How to Intelligently Make Sense of Real Data. Texts in Computer Science, Springer.

Bhadeshia, H.K.D.H., 1981a. Driving force for martensitic transformation in steels. Metal Science 15, 175–177.

Bhadeshia, H.K.D.H., 1981b. Thermodynamic extrapolation and martensite-start temperature of substitutionally alloyed steels. Metal Science 15, 178–180.

Birol, Y., 2009. Solid fraction analysis with DSC in semi-solid metal processing. Journal of Alloys and Compounds 486, 173–177.

van Bohemen, S., 2013. The nonlinear lattice expansion of iron alloys in the range 1001600K. Scripta Materialia 69, 315–318.

Bojack, A., Zhao, L., Morris, P., Sietsma, J., 2012. In-situ determination of austenite and martensite formation in 13Cr6Ni2Mo supermartensitic stainless steel. Materials Characterization 71, 77–86.

Bokrost, J.C., Parker, E., 1963. THE MECHANISM OF THE MARTENSITE BURST IN Fe-Ni SINGLE CRYSTALS. Acta Metallurgica 11, 1291–1301.

Borgenstam, A., Hillert, M., Å gren, J., 2009. Metallographic evidence of carbon diffusion in the growth of bainite. Acta Materialia 57, 3242–3252.

Brofman, P., Ansell, G., 1983. On the effect of fine grain size on the M s temperature in Fe-27Ni-0.025 C alloys. Metallurgical and Materials Transactions A 14, 1929–1931.

Brown, M., 2001. Introduction to thermal analysis: techniques and applications.

Callister, W.D., Rethwisch, D.G., 2012. Fundamentals of Materials Science and Engineering: An Integrated Approach. Wiley.

Choi, S., 2003. Model for estimation of transformation kinetics from the dilatation data during a cooling of hypoeutectoid steels. Materials Science and Engineering: A 363, 72–80.

Davis, J.R., 1990. Properties and selection: nonferrous alloys and special-purpose materials. ASM handbook / prepared under the direction of the ASM International Handbook Committee, ASM International.

Durand-Charre, M., 2004. Microstructure of Steels and Cast Irons.

Dykhuizen, R., Robino, C., Knorovsky, G., 1999. A Method for Extracting Phase Change Kinetics from Dilatation for Multistep Transformations : Austenitization of a Low Carbon Steel. Metallurgical and Materials Transactions B 30, 107–117.

Farahat, A.I.Z., 2008. Dilatometry determination of phase transformation temperatures during heating of Nb bearing low carbon steels. Journal of Materials Processing Technology 204, 365–369.

Fisher, J., Hollomon, J., Turnbull, D., 1949. KINETICS OF THE AUSTENITE-] MARTENSITE TRANSFORMATION. Metals Transactions 185, 691–700.

Fornaro, O., Palacio, H.a., 2009. Study of dilute AlCu solidification by cooling curve analysis. Journal of Materials Science 44, 4342–4347.

Frankel, J.I., Porter, W.D., Sabau, A., 2005. Analysis of Volumetric Changes Through Melting Using a Dilatometer. Journal of Thermal Analysis and Calorimetry 82, 171–177.

Ghosh, G., Olson, G., 1994a. Kinetics of F.C.C. B.C.C. heterogeneous martensitic nucleationI. The critical driving force for athermal nucleation. Acta Metallurgica et Materialia 42, 3361–3370.

Ghosh, G., Olson, G., 1994b. Kinetics of F.c.c. b.c.c. heterogeneous martensitic nucleationII. Thermal activation. Acta Metallurgica et Materialia 42, 3371–3379.

Gibbs, J.W., 2009. Thermal Analysis Techniques for Phase Fraction Measurements of First-order Phase Transformations. Msc. Colorodo School of Mines.

Gibbs, J.W., Kaufman, M.J., Hackenberg, R.E., Mendez, P.F., 2010. Cooling Curve Analysis to Determine Phase Fractions in Solid-State Precipitation Reactions. Metallurgical and Materials Transactions A 41, 2216–2223.

Gibbs, J.W., Mendez, P.F., 2008. Solid fraction measurement using equation-based cooling curve analysis. Scripta Materialia 58, 699–702.

Gibbs, J.W., Schlacher, C., Kamyabi-Gol, A., Mayr, P., Mendez, P.F., 2014. Cooling Curve Analysis as an Alternative to Dilatometry in Continuous Cooling Transformations. Metallurgical and Materials Transactions A 46, 148–155.

Giumelli, A., Militzer, M., Hawbolt, E., 1999. Analysis of the austenite grain size distribution in plain carbon steels. ISIJ international 39, 271–280.

Gladman, T., 1997. The physical metallurgy of microalloyed steels.

Gojić, M., Sućeska, M., Rajić, M., 2004. Thermal analysis of low alloy Cr-Mo steel. Journal of Thermal Analysis and Calorimetry 75, 947–956.

Gómez, M., Medina, S.F., Caruana, G., 2003. Modelling of Phase Transformation Kinetics by Correction of Dilatometry Results for a Ferritic Nb-microalloyed Steel. ISIJ International 43, 1228–1237.

Gupta, S.V., 2002. Practical Density Measurement and Hydrometry. Series in Measurement Science and Technology, CRC Press.

Holt, J.M., Gibson, C., Ho, C.Y., for Information, P.U.C., Analysis, N.D., Synthesis, 1999. Structural Alloys Handbook. Number v. 2 in Structural Alloys Handbook, CINDAS/Purdue University.

Http://www.thermocalc.com, 2013. Thermo-Calc Software TCFE6 Steels/Fe-alloys database Version 6.2.

Huang, J., Xu, Z., 2006. Effect of dynamically recrystallized austenite on the martensite start temperature of martensitic transformation. Materials Science and Engineering: A 438-440, 254–257.

JAHM, 1999. Material Property Database (MPDB v6.61).

Jiao, S., Penning, J., Leysen, F., Houbaert, Y., Aernoudt, E., 2000. The Modeling of the Grain Growth in a Continuous Reheating Process of a Low Carbon Si-Mn Bearing TRIP Steel. ISIJ International 40, 1035–1040.

Kamyabi-Gol, A., Gibbs, J.W., Mendez, P.F., 2015. Advanced mathematical treatment of dilatometry and calorimetry to discriminate and quantify multiple phase transformations, in: Proceedings of the International Conference on Solid-Solid Phase Transformations in Inorganic Materials 2015, Whistler, BC, Canada. pp. 1199–1206.

Kamyabi-Gol, A., Mendez, P.F., 2014. The Evolution of the Fraction of Individual Phases During a Simultaneous Multiphase Transformation from TimeTemperature Data. Metallurgical and Materials Transactions A 46, 622–638.

Kaufman, L., Cohen, M., 1958. Thermodynamics and kinetics of martensitic transformations. Progress in Metal Physics 7, 165–246.

Kiani-Rashid, A., Edmonds, D., 2008. Phase transformation study of aluminium-containing ductile cast irons by dilatometry. Materials Science and Engineering: A 481-482, 752–756.

Kiuchi, M., Sugiyama, S., 1994. A New Method to Detect Solid Fractions of Mushy/Semi-Solid Metals and Alloys. Annals of the CIRP 43, 271–274.

Knorovsky, G.a., Robino, C.V., Dykhuizen, R.C., MacCallum, D.O., 1998. Dilatometry in the Gleeble: What Did You Really Measure? ASM Proceedings of the International Conference: Trends in Welding Research 4, 101–106.

Koistinen, D., Marburger, R., 1959. A general equation prescribing the extent of the austenite-martensite transformation in pure iron-carbon alloys and plain carbon steels. Acta Metallurgica 7, 59–60.

Kolmskog, P., Borgenstam, A., Hillert, M., Hedström, P., Babu, S.S., Terasaki, H., Komizo, Y.I., 2012. Direct observation that bainite can grow below MS. Metallurgical and Materials Transactions A: Physical Metallurgy and Materials Science 43, 4984–4988.

Kop, T., Sietsma, J., Zwaag, S.V.D., 2001. Dilatometric analysis of phase transformations in hypo-eutectoid steels. Journal of materials science 36, 519–526.

Kuntz, M.L., Panton, B., Wasiur-Rahman, S., Zhou, Y., Corbin, S.F., 2013. An Experimental Study of Transient Liquid Phase Bonding of the Ternary Ag-Au-Cu System Using Differential Scanning Calorimetry. Metallurgical and Materials Transactions A 44, 3708–3720.

Lee, S.J., Lee, Y.K., 2005. Effect of Austenite Grain Size on Martensitic Transformation of a Low Alloy Steel. Materials Science Forum 475-479, 3169–3172.

Lee, S.J., Lee, Y.K., 2008. Prediction of austenite grain growth during austenitization of low alloy steels. Materials & Design 29, 1840–1844.

Lee, S.J., Lusk, M., Lee, Y.K., 2007. Conversional model of transformation strain to phase fraction in low alloy steels. Acta Materialia 55, 875–882.

Lee, S.J., Tyne, C.J.V., 2011. Prediction of Martensite Volume Fraction in FeCrNi Alloys. ISIJ International 51, 169–171.

Leeuwen, Y.V., Onink, M., Sietsma, J., Zwaag, S.V.D., 2001. The .GAMMA.-.ALPHA.Transformation Kinetics of Low Carbon Steels under Ultra-fast Cooling Conditions. ISIJ International 41, 1037–1046.

Lu, L., Dahle, A.K., 2005. Iron-Rich Intermetallic Phases and Their Role in Casting Defect Formation in Hypoeutectic Al-Si Alloys. Metallurgical and Materials Transactions A 36, 819–835.

MacKenzie, R.C., 1970. Differential Thermal Analysis. Academic Press.

Mayr, P., 2013. Henry Granjon Prize Competition 2008 Joint Winner Category B: Materials Behaviour and Weldability Evolution of Microstructure and Mechanical Properties of the Heat-Affected Zone in 9Cr Steels. Welding in the World 54, R1–R11.

Mayr, P., Palmer, T., Elmer, J., Specht, E., Allen, S., 2010. Formation of Delta Ferrite in 9 Wt Pct Cr Steel Investigated by In-Situ X-Ray Diffraction Using Synchrotron Radiation. Metallurgical and Materials Transactions A 41, 2462–2465.

Mayr, P., Palmer, T.A., Elmer, J.W., Specht, E.D., 2008. Direct observation of phase transformations in the simulated heat-affected zone of a 9Cr martensitic steel. International Journal of Materials Research 99, 381–386.

Mendez, P.F., 2010. Characteristic Values in the Scaling of Differential Equations in Engineering. Journal of Applied Mechanics 77, 610171–12.

American Society for Metals, ., 1977. Atlas of isothermal transformation and cooling transformation diagrams. American Society for Metals.

Militzer, M., Giumelli, A., Hawbolt, E., Meadowcroft, T., 1996. Austenite grain growth kinetics in Al-killed plain carbon steels. Metallurgical and Materials Transactions A 27, 3399–3409.

Mohanty, O.N., Bhagat, a.N., 2003. Electrical resistivity and phase transformation in steels. Materialwissenschaft und Werkstofftechnik 34, 96–101.

Onink, M., Tichelaar, F., 1996. Quantitative analysis of the dilatation by decomposition of Fe-C austenites; Calculation of volume change upon transformation. Zeitschrift fur . . . 87, 24–32.

Onink, M., Tichelaar, F., Brakman, C., Mittemeijer, E., van der Zwaag, S., 1996. Quantitative analysis of the dilatation by decomposition of Fe-C austenites; Calculation of volume change upon transformation. Zeitschrift fur . . . 87, 24–32.

P, T., Martín, J.P., Perez, J., 2004. SteCal 3.0: User Manual. Asm International.

Peet, M., Hasan, H., Bhadeshia, H., 2011. Prediction of thermal conductivity of steel. International Journal of Heat and Mass Transfer 54, 2602–2608.

Poirier, D.R., Geiger, G.H., 2013. Transport Phenomena in Materials Processing. Wiley.

Ravi, C., Wolverton, C., 2005. Comparison of thermodynamic databases for 3xx and 6xxx aluminum alloys. Metallurgical and Materials Transactions A 36, 2013–2023.

Reti, T., Fried, Z., Felde, I., 2001. Computer simulation of steel quenching process using a multi-phase transformation model. Computational Materials Science 22, 261–278.

Saito, Y., Shiga, C., 1992. Computer Simulation of Microstructural Evolution in Thermomechanical Processing of Steel Plates. ISIJ international 32, 414–422.

Sarma, D., Whiteman, J., Keown, S., 1979. The structure of burst and isothermal martensites in an Fe-24 wt% Ni-0.5 wt% C alloy. Journal of Materials Science 14, 693–698.

Schneider, C.A., Rasband, W.S., Eliceiri, K.W., 2012. NIH Image to ImageJ: 25 years of image analysis. Nature Methods 9, 671–675.

Sourmail, T., Smanio, V., 2013a. Determination of M s temperature: methods, meaning and influence of slow start phenomenon. Materials Science and Technology 29, 883–888.

Sourmail, T., Smanio, V., 2013b. Response to comments on Determination of M s temperature: methods, meaning and influence of slow start phenomenon by T. Sourmail and V. Smanio. Materials Science and Technology 29, 890–892.

Speyer, R., 1993. Thermal analysis of materials.

Stefanescu, D.M., Upadhya, G., Bandyopadhyay, D., 1990. Heat Transfer-Solidification Kinetics Modeling of Solidification of Castings. Metallurgical Transactions A 21, 997–1005.

Suárez, J., Molleda, F., de Salazar, J.G., 1992. Modeling of grain growth during arc welding of high strength low alloy steels. Materials characterization 28, 3–13.

Suh, D.W., Oh, C.S., Han, H.N., Kim, S.J., 2007. Dilatometric analysis of austenite decomposition considering the effect of non-isotropic volume change. Acta Materialia 55, 2659–2669.

Suwanpinij, P., Kitkamthorn, U., Diewwanit, I., Umeda, T., 2003. Influence of Copper and Iron on Solidification Characteristics of 356 and 380-Type Aluminum Alloys. Materials Transactions 44, 845–852.

Tamminen, J., 1988. Thermal analysis for investigation of solidification mechanisms in metals and alloys. Phd. University of Stockholm.

Tszeng, T., Shi, G., 2004. A global optimization technique to identify overall transformation kinetics using dilatometry dataapplications to austenitization of steels. Materials Science and Engineering: A 380, 123–136.

United States Steel Corporation, ., 1953. Atlas of isothermal transformation diagrams. United States Steel.

Warke, V.S., Sisson, R.D., Makhlouf, M.M., 2009. A Model for Converting Dilatometric Strain Measurements to the Fraction of Phase Formed during the Transformation of Austenite to Martensite in Powder Metallurgy Steels. Metallurgical and Materials Transactions A 40, 569–572.

Xu, J., Liu, F., Xu, X., Chen, Y., 2011. Determination of Solid Fraction from Cooling Curve. Metallurgical and Materials Transactions A 43, 1268–1276.

Xu, J., Liu, F., Zhang, D., 2013. In situ observation of solidification of undercooled hypoeutectic NiNi3B alloy melt. Journal of Materials Research 28, 1891–1902.

Xu, J.F., Liu, F., Zhang, D., Zhang, K., 2012. Comparison of baseline method and DSC measurement for determining phase fractions. Materials Science and Technology 28, 1420–1425.

Yakubtsov, I.a., Purdy, G.R., 2012. Analyses of transformation kinetics of carbide-free bainite above and below the athermal martensite-start temperature. Metallurgical and Materials Transactions A: Physical Metallurgy and Materials Science 43, 437–446.

Yang, H., Bhadeshia, H., 2009. Austenite grain size and the martensite-start temperature. Scripta Materialia 60, 493–495.

Yang, H.S., Bhadeshia, H.K.D.H., 2007. Uncertainties in dilatometric determination of martensite start temperature. Materials Science and Technology 23, 556–560.

Yang, H.S., Jang, J.H., Bhadeshia, H.K.D.H., Suh, D.W., 2012. Critical assessment: Martensite-start temperature for the $\gamma \quad \epsilon$ transformation. Calphad: Computer Coupling of Phase Diagrams and Thermochemistry 36, 16–22.

Yoshie, A., Fujioka, M., Watanabe, Y., 1992. Modelling of microstructural evolution and mechanical properties of steel plates produced by thermo-mechanical control process. ISIJ international 32, 395–404.

Zenitani, S., Hayakawa, N., Yamamoto, J., Hiraoka, K., Morikage, Y., Kubo, T., Yasuda, K., Amano, K., 2007. Development of new low transformation temperature welding consumable to prevent cold cracking in high strength steel welds. Science and Technology of Welding and Joining 12, 516–522.

Zhao, J., Mesplont, C., Cooman, C., 2002. Calculation of the phase transformation kinetics from a dilatation curve. Journal of Materials Processing Technology 129, 345–348.

Zhao, J.Z., Mesplont, C., Cooman, B.C.D., 2001. Kinetics of Phase Transformations in Steels: A New Method for Analysing Dilatometric Results. ISIJ International 41, 492–497.